

$D^{*\pm}$ Meson Production at low Q^2
with the H1 Detector and
Determination of Unintegrated
Gluon Densities

Dissertation
zur Erlangung des Doktorgrades
des Department Physik
der Universität Hamburg

vorgelegt von

Axel Cholewa

aus Stadthagen

Hamburg

2010

$D^{*\pm}$ Meson Production at low Q^2
with the H1 Detector and
Determination Of Unintegrated
Gluon Densities

Dissertation
zur Erlangung des Doktorgrades
des Department Physik
der Universität Hamburg

vorgelegt von

Axel Cholewa

aus Stadthagen

Hamburg

2010

Gutachter der Dissertation:	Dr. Hannes Jung Prof. Dr. Joachim Meyer
Gutachter der Disputation:	Dr. Hannes Jung Prof. Dr. Peter Schleper
Datum der Disputation:	28.1.2011
Vorsitzender des Promotionsausschusses:	Prof. Dr. Joachim Bartels
Dekan der Fakultät Mathematik, Informatik und Naturwissenschaften:	Prof. Dr. Heinrich Graener

Zusammenfassung

Die inelastische Produktion von $D^{*\pm}$ -Mesonen in Elektron-Proton-Streuung bei kleinen Photonvirtualitäten wurde mithilfe von Daten des H1-Experiments untersucht. Die Ergebnisse dieser Messung wurden daraufhin verwendet, um mit dem Ereignisgenerator CASCADE unintegrierte Gluondichten zu ermitteln.

Der Phasenraum der Messung ist gegeben durch Photonvirtualitäten im Bereich von $2 \text{ GeV}^2 < Q^2 < 5 \text{ GeV}^2$ und Inelastizitäten innerhalb $0.02 < y < 0.7$. Der sichtbare Bereich der $D^{*\pm}$ -Mesonen ist auf Pseudorapiditäten von $|\eta^{D^*}| < 1.5$ und Transversalimpulse $p_t^{D^*} > 1.5 \text{ GeV}$ beschränkt und ergänzt Messungen von $D^{*\pm}$ -Mesonproduktion bei höheren Virtualitäten. Die Daten wurden in den Jahren 2004 bis 2007 in der HERA-II-Phase vom H1-Detektor aufgenommen und ergeben eine integrierte Luminosität von 348 pb^{-1} . Diese gegenüber H1-Messungen in der HERA-I-Phase deutlich erhöhte Statistik ermöglichte eine differenziertere Messung von einfach- und doppeltdifferentiellen Wirkungsquerschnitten der $D^{*\pm}$ -Mesonproduktion.

Die einfach differentiellen Wirkungsquerschnitte dieser Messungen wurden anschließend verwendet, um mittels Parameteranpassung unintegrierte, d.h. vom Transversalimpuls abhängige, Gluondichten zu ermitteln. Dafür wurden Streueignisse in Elektron-Protonkollisionen mit dem Monte Carlo-Programm CASCADE simuliert und die Abweichung der Simulationsvorhersagen im χ^2 -Verfahren minimiert. Drei verschiedene Parametrisierungen der unintegrierten Gluondichte wurden verwendet und die Ergebnisse verglichen.

Abstract

A study of inclusive $D^{*\pm}$ meson production in deep inelastic electron-proton scattering at the H1 detector is presented for low photon virtualities. The results of these measurements have been used to determine untegrated gluon densities with the Monte Carlo generator CASCADE.

The phase space of the measurement is defined by photon virtualities inside $2 \text{ GeV}^2 < Q^2 < 5 \text{ GeV}^2$, and inelasticities inside $0.02 < y < 0.7$. The visible region of the production of $D^{*\pm}$ mesons is restricted to pseudo rapidities of $|\eta^{D^*}| < 1.5$ and transverse momenta of $p_t^{D^*} > 1.5 \text{ GeV}$ and complements $D^{*\pm}$ meson production measurements at higher photon virtualities. Data taken in the years 2004-2007 during the HERA II running period have been analyzed yielding an integrated luminosity of 348 pb^{-1} . This significant increase in statistics compared to HERA I was exploited in the single

and double differential cross sections which have been measured more differentiated than in previous measurements at H1.

The single differential cross sections have been used in parameter fits of unintegrated gluon densities. For this purpose scattering events in electron-proton collisions were simulated with the Monte Carlo generator CASCADE and the deviation of the prediction of the simulation from the measured data was then minimized with the χ^2 method. Three different parametrizations of unintegrated gluon distributions have been used and compared.

Contents

Nomenclature	VII
Introduction	1
1 Deep Inelastic Scattering	5
1.1 Kinematics of the Parton Model	5
1.2 Quarks and Gluons in the Proton	7
1.2.1 The Proton Structure Function	8
1.2.2 The Strong Interaction	8
1.3 $D^{*\pm}$ Meson Production in Electron-Proton Collisions	11
1.3.1 Charm Quark Production at HERA	12
1.3.2 $D^{*\pm}$ Mesons as Charm Quark Tags	12
1.4 Unintegrated Gluon Densities	13
1.5 Monte Carlo Event Generators	13
1.5.1 The Three Stages Of Simulation	14
1.5.2 Event Generators In Use	14
2 The H1 Experiment	17
2.1 The Particle Accelerator HERA	17
2.2 The Detector	20
2.3 Calorimetry at H1	20
2.3.1 The Liquid Argon Calorimeter	21
2.3.2 The Backward Calorimeter SpaCal	22
2.4 The Central Tracking Devices	23
2.4.1 The Jet Chambers	25
2.4.2 The Central Silicon Tracker	27
2.4.3 The Central Proportional Chambers	27
2.4.4 The Z-Chambers	27
2.5 Triggering Physics Events at H1	28

2.6	Detector Simulation and Reconstruction	29
3	D* Meson Cross Sections	31
3.1	Heavy Quark Physics at H1	31
3.1.1	Charm Production Measurements	32
3.1.2	Beauty Production Measurements	33
3.2	The Electron Energy Measurement	34
3.2.1	Reconstruction of Kinematic Variables	34
3.2.2	The Electron Selection	36
3.2.3	Testing the Calibration of the Electron Energy Measurement	39
3.2.4	Control Distributions	42
3.3	Triggering D* mesons in DIS	43
3.3.1	Trigger Elements	44
3.3.2	Trigger Efficiencies	44
3.4	Event and D^* Meson Selection Criteria	47
3.5	The D* 's Golden Decay Channel	48
3.5.1	Reconstructing D* Mesons from Tracks	49
3.5.2	Signal Extraction	50
3.5.3	Choice of Fit Function	52
3.5.4	Control Distributions for Track Quantities	53
3.6	Detection Efficiencies and Migration Effects	63
3.7	Contributions from Reflections and Photoproduction	66
3.7.1	Reflections	66
3.7.2	Photoproduction Background	68
3.8	Radiative Corrections	69
3.9	Systematic Uncertainties	71
3.9.1	Uncertainty of Energy Measurements	71
3.9.2	Losses From The D⁰ Mass Window	75
3.9.3	Reweighting Uncertainty	76
3.10	The Total D* Meson Cross Section at low Q^2	80
3.11	Differential Cross Sections	81
4	Parton Distribution Functions	87
4.1	Factorization and the Hard Interaction	87
4.2	Parton Evolution	89
4.2.1	Collinear Factorisation	89

4.2.2	\mathbf{k}_t -factorisation	94
4.3	Next-To-Leading Order Corrections	98
5	Event Generators and Parton Distributions	101
5.1	Simulation of scattering events	101
5.1.1	Matrix Element Calculation	101
5.1.2	Process Selection	102
5.1.3	Parton Showers	103
5.1.4	Fragmentation and Hadronisation	104
5.1.5	Decays Of Unstable Particle	105
5.2	Parton Evolution in Event Generators	106
5.2.1	The Collinear Approach in Event Generators	106
5.2.2	PDF4MC	107
5.2.3	UPDFs in MC Generators	108
6	Determination of Parton Densities	109
6.1	The Analytic Method	109
6.2	The Monte Carlo Method	110
6.3	Outline of the Fitting Formalism	110
6.4	Unintegrated Gluon Densities from D^* Mesons at low Q^2	111
	Summary and Conclusion	119
	A Cross Section Tables	121
	Bibliography	125
	Acknowledgments – Danksagung	129

Contents

Nomenclature

- ⊗ Mathematical convolution: $A \otimes B(t) = \int f(\tau)g(t - \tau)d\tau$, page 88
- ⊕ Addition in quadrature: $x \oplus y = \sqrt{x^2 + y^2}$, page 22
- QPM Quark Parton Model, page 6
- BGF Boson Gluon Fusion process, page 89
- NLO next-to-leading order, page 98
- MC short for Monte Carlo event generator, page 101
- LO leading order, page 89
- QCDC QCD Compton process, page 89
- QCD Quantum Chromodynamics, the theory of the strong interaction between quarks, page 10
- $g(x, Q^2)$ Gluon distribution function, gluon density, page 91
- detector level* Hits, tracks, energy deposits. For simulated events these are obtained by detector simulation , page 14
- generator/hadron level* Simulated event information and four momenta of particles as produced by MC simulations, page 14
- reconstruction level* Event information – measured as well as simulated – and four momenta of particles after and reconstruction, page 14
- $D^{*\pm}$ a meson consisting of a charm quark and an anti-down quark (or vice versa); used in this analysis to tag scattering events involving charm quarks, page 31
- run periods* HERA was operated with electrons in positrons in four run periods: 2004 e^+ , 2004/05 e^- . 2006 e^- , 2006/07 e^+ , page 20

Contents

γ_h	Effective scattering angle of the hadronic final state, page 39
p_e	Four-momentum of the incoming electron, page 6
p_p	Four-momentum of the incoming proton, page 6
Q^2	Virtuality of the exchanged photon, also referred to as four-momentum transfer, page 7
$E_{e'}$	Energy of the scattered electron, page 34
θ_e	Polar angle of the scattered electron, page 34
Σ	Sum of $E - p_z$ of all final state particles, incl. scattered electron, page 35
x, x_q	Fraction of proton momentum carried by a quark, page 6
x_{Bj}	The Bjorken variable x . In the quark parton model it is identical to the quark momentum fraction x_q , page 7

Introduction

Scattering Experiments

Since the days of Ernest Rutherford scattering experiments have been effective tools for probing the structure of matter at smallest distances. Rutherford shot α -particles at a gold target foil and found that the gold foil consisted of very small scattering centers of $\sim 10^{-14}$ m, which today are called atomic nuclei. But Rutherford's experiment was more than just proof of the existence of atomic cores: it lay the foundation for modern experiments probing the structure of matter.

The Composite Proton

Today, much more is known about the structure of matter. Atoms are not fundamental building blocks, they consist of an outer shell made up of electrons, and neutrons and protons which form atomic nuclei. While electrons are still considered fundamental, neutrons and protons are composed of quarks or, more generally, *partons*. Partons are not found separately in experiments, they are always part of a larger compound like a neutron or proton.

At the accelerator HERA (Hadron Ring-Anlage) at the DESY facility at Hamburg, the partonic structure of protons was studied. Electrons were collided with protons at very high energies, and in such a collision an electron interacts with a quark in the proton via the electromagnetic force. At the energy of the HERA collisions hadrons are formed in the collisions. These hadrons as well as the scattered electron were detected by the H1 detector.

D^* Mesons in Electron-Proton Collisions

The production of one such particle, the D^* meson, was studied in this thesis. It consists of a charm quark, a heavy quark which only manifests itself in highly energetic

protons. Charm quarks, and therefore D^* mesons, are dynamically created in the strong interaction which binds the quarks together. D^* mesons are thus directly sensitive to the strong interaction in the proton.

D^* meson production has been studied before both in the HERA I and in the HERA II running periods, but either not with the same statistics (HERA I) or in a different region of phase space (HERA II, see [1] and [2, 3]). Here, D^* meson production was studied in the low Q^2 region, which is more sensitive to low parton momentum fractions.

Unintegrated Gluon Densities

The interaction between quarks in the proton is described by the theory of Quantum Chromodynamics (QCD). As a quantum field theory it states that the interaction of quarks is mediated by a boson. This boson is called *gluon*, because it “glues” the quarks together. It is also considered a parton, because it too is found only inside hadron.

In theoretical predictions partons appear in the form of *parton distribution functions*, or *parton densities*. These are momentum distribution functions which contribute to proton scattering cross sections. In this thesis *unintegrated parton densities* are determined. They introduce a dependence of the parton densities on the parton’s transverse momentum component, which is missing in the more common framework of collinear parton densities. This makes unintegrated parton densities more suited for the use in computer programs simulating high energy scattering events, because the kinematics in particle collisions can be treated more consistently.

Exploiting the direct sensitivity of D^* meson production to the gluon content of the proton, unintegrated gluon densities are determined by fits to the cross sections measured in this analysis.

The Structure Of This Thesis

The experimental data used here was collected in the collider experiment H1 at the particle accelerator HERA. There electrons and protons were collided from 1992 until 2007 to study the partonic structure of the proton. The measurement of the D^* meson production cross section at low photon virtualities is the topic of this thesis. From these cross sections unintegrated gluon densities are determined.

The first chapter explains the ideas behind modern experiments probing the structure of protons and the basic models describing the outcomes. After an overview of the H1 detector in chapter 2, the measurement of D^* meson production cross sections is presented in detail in chapter 3.

Chapters 4 and 5 deal with theoretical aspects of the parton model and how these are incorporated in computer programs simulating the interaction of electrons and protons. These chapters also introduce the formalism of unintegrated parton densities. In chapter 6 I describe how unintegrated gluon densities can be obtained by fits to exclusive final state measurements. I present first results and discuss the difference to former methods.

Introduction

1 Deep Inelastic Scattering

In this chapter I briefly introduce the ideas behind deep inelastic scattering and the parton model and its application to current particle collider experiments. Only the most basic concepts are discussed here. A more detailed presentation on the subject will be given in chapters 4 and 5.

The first section 1.1 deals with the kinematics of lepton-nucleon scattering. Section 1.2 introduces the notion of gluons as the carriers of the strong nuclear force and explains shortly how they influence the proton structure. Also *the* idea of *parton distribution functions* (PDFs) or *parton densities* is presented.

The role of charm quarks in electron-proton scattering is discussed in section 1.3, before the last section of this chapter gives a short overview of the Monte Carlo simulations used in this analysis.

1.1 Kinematics of the Parton Model

In order to study the properties of the strong interaction many experiments exist where a proton target is probed by a lepton, be it electron or positron, muon or neutrino. One possibility is to use a fixed proton target, e. g. in the form of liquid

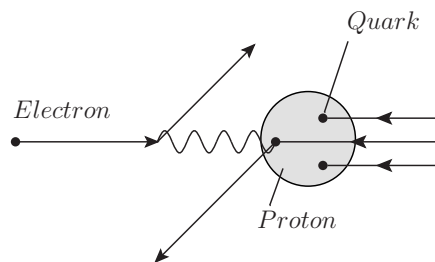


Figure 1.1: *The basic idea behind deep inelastic scattering: An electron collides with a proton head on and interacts with a quark inside the proton via the electroweak interaction, which is mediated by a virtual photon, Z or W boson (sketched by the wavy line).*

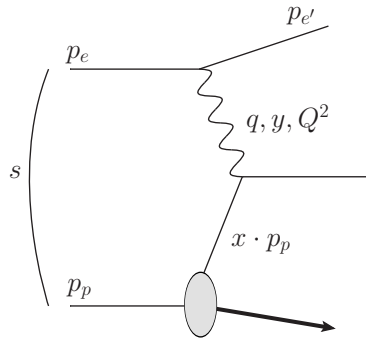


Figure 1.2: Diagram showing the basic kinematic variables in ep -scattering.

hydrogen. This was done by various experiments at the Stanford Linear Accelerator Center (SLAC), DESY and others.

To reach higher center-of-mass energies it is beneficial not to collide a probe on a fixed target but to use two accelerated particle beams and collide them head-on. This is because at high energies the energy in the center-of-mass frame is higher for head-on collider experiments as for fixed target experiments.

At the HERA accelerator an electron¹ beam is colliding with a highly energetic proton beam². The physical picture of such an electron-proton collision can be viewed in figure 1.1: the electron interacts via the electroweak interaction, i. e. by exchange of either a photon, a Z^0 boson or a W^\pm boson, with a constituent of the proton, called quark or parton. This assumption, that the proton consists of partons moving in the same direction, is called the *quark parton model* (QPM).

The case of W^\pm exchange is called *charged current*, because the W bosons carry electric charge, whereas the exchange of neutrally charged Z^0 and γ is referred to as *neutral current*. In this analysis only neutral current events are examined.

The kinematic variables needed for the description of the system are illustrated in figure 1.2: an electron with four-momentum p_e interacts with a quark of momentum $x_q \cdot p_p$ in a proton of four momentum p_p , where x_q is the *momentum fraction* carried by the quark. The scattered electron's four-momentum is denoted $p_{e'}$, while q is the four-momentum of the virtual photon.

From these variables a set of four Lorentz invariants can be defined that, neglecting mass terms, over-determine the state of the system [4]:

¹Throughout this thesis the term *electron* refers to electrons as well as positrons, as HERA collided both lepton types with protons. Whenever the difference is important it is emphasized.

²HERA and the H1 experiment are introduced in more detail in chapters 2.1 and 2, respectively.

$$s = (p_e + p_p)^2 \quad (1.1)$$

$$Q^2 = -q^2 = -(p_e - p_{e'})^2 \quad (1.2)$$

$$x_{Bj} = \frac{Q^2}{2p_p \cdot q} \quad (1.3)$$

$$y_{Bj} = \frac{p_p \cdot q}{p_p \cdot p_e} \quad (1.4)$$

These variables are related via

$$Q^2 = x_{Bj} \cdot y_{Bj} \cdot s \quad (1.5)$$

The Bjorken variable x_{Bj} can be identified with the quark's momentum fraction, $x_q \equiv x_{Bj}$, while in the proton rest frame (*prf*) the inelasticity y_{Bj} can be interpreted as the virtual photon's fraction of the electron energy, $y_{Bj} = E_\gamma^{prf} / E_e^{prf}$. The squared center-of-mass energy (see eq. (1.5)) of the electron-proton system is given by s . The virtuality of the photon, Q^2 , is defined as the squared four-momentum transfer between the electron and the proton. In deep inelastic scattering it gains a special status as it can set the energy scale for the hard interaction of the virtual photon and the scattered parton.

The exchange of Z^0 bosons dominates at virtualities approaching the Z^0 mass peak, $m_Z^2 \simeq 8100 \text{ GeV}^2$, while photon exchange governs the low Q^2 region. Later on the measurement of D^* meson cross section will be presented for low virtualities $2 < Q^2 < 5 \text{ GeV}^2$, so that Z^0 exchange does not contribute. Therefore only photon exchange is considered in the following considerations.

1.2 Quarks and Gluons in the Proton

The quark parton model as shown in figure 1.2 was invented to explain the first measurements [5, 6] of the proton structure function. What these first measurements were hiding, however, was a dependency on the energy scale at which the interaction with the quarks takes place. This *scaling violation* were the first evidence that the QPM alone could not explain the structure of the proton.

1.2.1 The Proton Structure Function

The structure function of the proton enters the scattering cross section in a similar way as form factors known, for example, from Rutherford scattering. The scattering cross section of electron-proton reads:

$$\frac{d^2\sigma}{dx dQ^2} = \frac{2\pi\alpha_{em}^2}{xQ^4} (1 + (1-y)^2) F_2(x). \quad (1.6)$$

In addition to the kinematic variables Q^2 and x as defined in the previous section the electromagnetic coupling constant α_{em} (also known as the fine structure constant) also enters the calculation.

The proton structure function can now loosely be interpreted as the probability that the probe scatters off an arbitrary quark carrying the fraction x of the proton momentum. It is given by

$$F_2(x) = \sum_i e_i x f_i(x),$$

where the index i runs over all quark flavors in the proton and e_i is the charge of quark i in units of the elementary charge. f_i is the *parton distribution function*, meaning the distribution of the momentum fraction x of a quark of flavor i . Note the subtle difference to the interpretation of F_2 : parton distribution function state how probable it is to find a certain quark *flavor*, structure functions are a measure for how likely it is that a scattering off a quark in general occurs.

In the experimental data from the HERA accelerator shown in figure 1.3 where the structure function F_2 is shown as a function of Q^2 for various fixed momentum fractions x a Q^2 dependence is visible especially for $x \lesssim 0.13$. This scaling violation cannot be explained by the naive quark parton model, which approximates the proton to consist of three independent quarks. One needs to introduce the strong interaction into this model in order to obtain Q^2 dependent parton densities $f_i(x, Q^2)$ leading to a Q^2 dependent structure function $F_2(x, Q^2)$. How this is done is outlined in more detail in chapter 4.

1.2.2 The Strong Interaction

The origin of scaling violations lies in the interaction of the quarks. These are not independent particles, but rather constantly interacting via the strong force. Like the electromagnetic interaction, the strong interaction or Quantum Chromodynamics

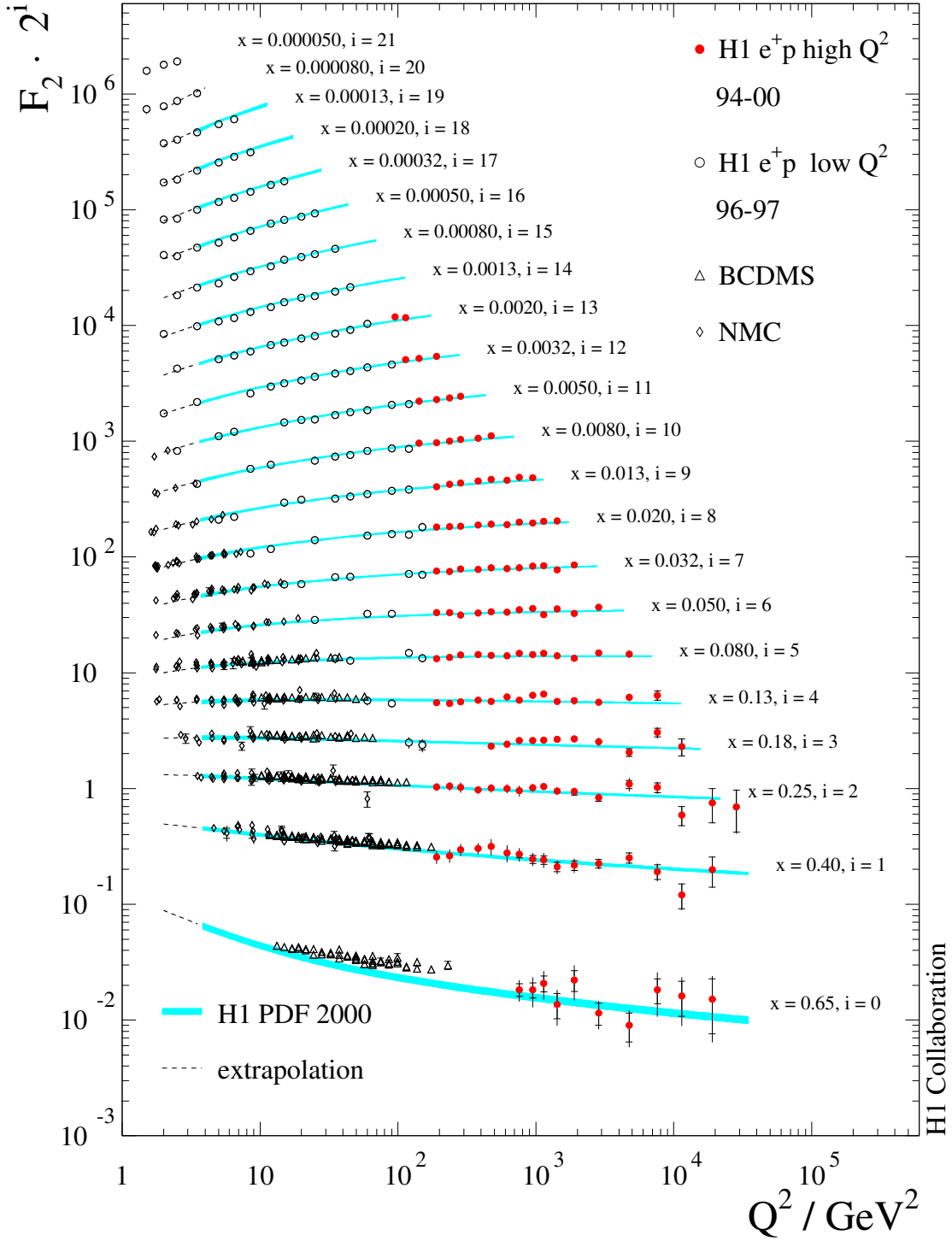


Figure 1.3: The structure function F_2 as a function of the four-momentum transfer Q^2 as measured by various experiments. The scaling violation, meaning the dependence on Q^2 at fixed x arising from the contribution of gluons to the scattering cross section, can be observed.

1 Deep Inelastic Scattering

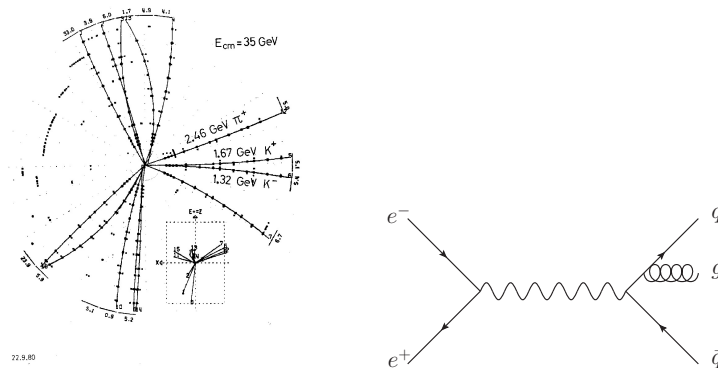


Figure 1.4: *On the left: Three jet event at the TASSO experiment at DESY.[7] On the right: the feynman diagram explaining three jet production production in electron-positron scattering with gluon radiation.*

(QCD) is mediated via an exchange boson called gluon.

The first direct experimental proof of the existence of gluons was obtained by the four collaborations TASSO, PLUTO, JADE and MARK J in 1979 at the PETRA facility, an e^+e^- storage ring at DESY in Hamburg. Colliding electrons and positrons annihilated each other, forming two quarks, one of which radiated a gluon (see fig. 1.4). All four collaborations presented their evidence on the same conference in August 1979. [7]

In contrast to the electromagnetic interaction, the strong interaction gets stronger the farther apart two interacting particles are and weaker if they are closer together. This leads to *asymptotic freedom*, meaning that two quarks that are very close behave approximately like free particles.

Like the quark, the gluon is a constituent of the proton: a parton. It is therefore possible that an electron scattering off a proton interacts indirectly with a gluon in the proton. Such a process is called *boson gluon fusion* (BGF) and is illustrated in figure 1.5: an electron interacts via photon exchange with the proton; a gluon g in the proton splits up into a quark anti-quark pair, one of which couples to the virtual photon (find a more detailed discussion of the influence of gluons on parton densities in chapter 4). A boson - the virtual photon - "fuses" with the gluon to form a quark anti-quark pair.

Quarks created in such a process are called *sea quarks*. The so called *valence quarks* are the quarks that determine if a baryon behaves like, for example, a proton or a neutron: protons consist of two up quarks and a down quark, neutrons of two down and one up quark.

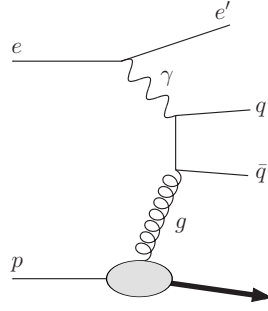


Figure 1.5: Boson Gluon Fusion in electron-proton scattering.

1.3 $D^{*\pm}$ Meson Production in Electron-Proton Collisions

The standard model of particle physics classifies particles into two general categories: bosons and fermions. Bosons are particles with integer spin, fermions with half integer spin. Exchange particles mediating a certain interaction like the electroweak or the strong interaction are always bosons, particles composing matter are fermions.³

Fermions can be further categorized into quarks and leptons. The following table lists all the know fermions, the associated symbol and their electric charge in units of the elementary charge e (anti-fermions have the same charge with opposite sign).

Fermions	1st family		2nd family		3rd family		Charge [e]
Leptons	e neutrino	ν_e	μ neutrino	ν_μ	τ neutrino	ν_τ	0
	electron	e	muon	μ	tau	τ	-1
Quarks	up	u	charm	c	top	t	+2/3
	down	d	strange	s	beauty ⁴	b	-1/3

The different types of quarks are called *flavors*. The strong interaction does not differentiate between the flavors. While the coupling of a photon to a quark depends on the quarks charge all the quark flavors couple equally strong to gluons. The weak interaction is flavor sensitive as well, in that processes including a W boson allow for a change of flavor. That means, for example, that while the process $u \rightarrow Z^0 c$ is forbidden the process $u \rightarrow W^+ s$ is allowed.

Another difference between the quark flavors is their mass. Quark masses span a range of nearly 5 orders of magnitude, from as few as 2.55 MeV for the up quark up

³This is only a loose concept, since gluons, for example, are also partons and therefore part of the composite proton.

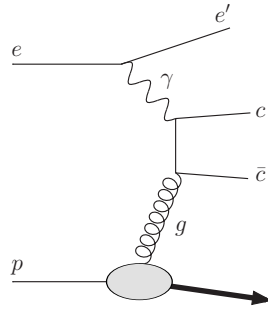


Figure 1.6: *Dominant charm quark production mechanism in electron-proton scattering.*

to 171 GeV for the top quark.[8]

The up, down and strange quarks are usually termed *light quarks*, while *heavy quarks* are the charm, beauty and top quark. This is because the masses of the light quarks are below the typical energy scale of QCD, $m_q < \Lambda_{QCD} \approx 200 \text{ MeV}$. Processes below this scale are not calculable in perturbation theory. The production of light sea quarks, for example, can be calculated only if the resulting jets or particles have a high enough energy.

1.3.1 Charm Quark Production at HERA

Because of the high center-of-mass energy of the HERA accelerator of $\sqrt{s} = 318 \text{ GeV}$, sea quark pairs with masses of up to $\sqrt{s}/2 = 159 \text{ GeV}$ can be produced in BGF at the H1 experiment. The charm quark has a mass of $m_c \approx 1.3 \text{ GeV}$ [8] so that charm quarks can be found among the sea quarks created in BGF processes.

Figure 1.6 shows a diagram for the production of charm quarks in electron-proton scattering. Since the gluon is a parton, one can determine its corresponding parton distribution function, the gluon density g . It is obvious from the figure that charm production processes are directly sensitive to the gluon density, because BGF is the dominant production mechanism for charm quarks in electron-proton collisions. The charm's high mass ensures the applicability of perturbation theory in such a process.

1.3.2 $D^{*\pm}$ Mesons as Charm Quark Tags

Together with light quarks charm quarks form mesons called D mesons. The $D^{*\pm}$ meson studied here is an excited D^\pm state consisting of a charm (or anti-charm quark) and an anti-down (or down quark) with a very short lifetime. Its decay

products, though, are long lived enough to leave tracks in the H1 detector. Such tracks were analyzed for measuring $D^{*\pm}$ meson production cross section in electron-proton collisions, quantities directly sensitive to momentum distributions of gluons in the proton. In chapter 3 I describe in detail how cross sections were determined using data recorded by the H1 detector.

1.4 Unintegrated Gluon Densities

The quark and gluon content of the proton is not deducible from first principles. Rather, as described above (sec. 1.2.1), the momentum distributions of quarks and gluons are parametrized in *parton distribution functions* or *parton densities*. These contain information on how probable it is to find a parton, quark and gluon alike, in the proton at a certain energy scale with a certain *longitudinal* momentum fraction x of the proton momentum.

These PDFs only depend on the longitudinal momentum fraction, but there are theoretical models where the PDFs also incorporate the transverse momentum of the partons. These PDFs are called *unintegrated* PDFs (uPDFs). In this thesis the experimental data of D^* meson production with the H1 detector is compared to predictions from the CCFM[9] formalism incorporating the concept of unintegrated gluon densities. Section 4.2.2 gives a more detailed presentation on the theoretical background of unintegrated gluon densities.

1.5 Monte Carlo Event Generators

For the estimation of systematic uncertainties, detector effects and physics phenomena that cannot be measured by the H1 detector (see sec. 3.7), it is vital to use simulations of the physics happening in ep -collisions. These are based on the theory of strong interactions, or Quantum Chromodynamics (QCD). Perturbative QCD (pQCD) calculations can be evaluated in such simulations to obtain statistical predictions for the outcome of a desired measurement, for example D^* meson production. Because these simulations *generate* collision *events*, and because this is implemented with Monte Carlo methods, they are often referred to as *Monte Carlo event generators*.⁵

⁵For a detailed presentation on how pQCD is implemented in event generators see chapter 5.

1.5.1 The Three Stages Of Simulation

For comparison to experimental data one classifies simulated events into three different stages of simulation:

- *generator* or *hadron level* events: at this stage simulated events are not directly comparable to experimental data because the simulations generate event topologies, i.e. four-momenta of particles produced in a collision, before the produced particles interact with the detector.
- *detector level* events: after generator level information has been subjected to a detector simulation the resulting event information is similar to real measurements: hits in drift chambers, energy deposits in calorimeters etc.
- *reconstruction level* events: measurements can be reproduced from detector level events by applying the complete reconstruction cycle of the experimental data: forming tracks out of hits in tracking chambers, energy clusters out of energy deposits in calorimeter cells, particle candidates out of tracks and energy clusters, jets out of particles.

The information of these different stages of simulation can be used, for example, to estimate detector effects by comparison of the reconstruction level events with the generator level events (section 3.6), or to find the contribution of physics which the detector alone cannot distinguish (section 3.7).

1.5.2 Event Generators In Use

In this analysis the event generators PYTHIA[10], RAPGAP[11] and CASCADE [12] have been used.

PYTHIA is a Monte Carlo Generator simulating electron-proton and proton-proton collisions. It used the Lund string model to implement hadronisation effects (see sec. 5.1.4).

RAPGAP is an event generator based on the DGLAP formalism (see section 4.2.1). It is widely used for estimations of detector effects in DIS and has been used here for detector efficiency determination.

CASCADE is a Monte Carlo generator based on the CCFM formalism (see section 4.2.2) which is specialized for sea quark production in BGF events and a correct treatment of the gluon kinematics.

For an easy comparison of experimental data to predictions from event generators the software package HZTOOL[13] was very helpful. It has been used here to compare unintegrated gluon densities to the data as well as to extract new unintegrated gluon densities (see chapter 6).

HZTOOL provides the user with a set of function to access certain information generated by a Monte Carlo program on run time, e.g. four momenta of particles or event kinematics. With these functions the user can write a subroutine which analyses generated events according to certain selection criteria and writes out histograms. For this analysis a subroutine has been written which writes out histograms according to the event and D^* meson selection used in the measurement (see table 3.3).

Both RAPGAP and CASCADE access the hadronisation functions of PYTHIA.

2 The H1 Experiment

For measuring the outcome of electron proton collisions at the HERA collider, the H1 Collaboration build a multi-purpose detector consisting of calorimetry and tracking systems designed for precise measurements of the inclusive proton structure function as well as detailed final state measurements, for example jet cross sections, charged particle multiplicities or cross section measurements of charm meson production.

The chapter starts with an introduction of the HERA accelerator and the basic concepts and ideas behind the experiment in sections 2.1 and 2.2. An overview of the calorimetry in both the central and backward region of the detector is given in section 2.3. The tracking system as explained in section 2.4 forms the foundation of this analysis as it allows for a precise measurement of the decay particles of D^* mesons. Section 3.2.1 addresses the reconstruction of kinematic variables, followed by the calibration check of the electron energy measurement with the backward calorimeter in section 3.2.3. This is especially important here because the measurement takes place at the lowest possible Q^2 region at H1 during the HERA II phase. The H1 trigger system is outlined in section 2.5. The chapter closes with a description of the detector simulation and the reconstruction software in section 2.6.

2.1 The Particle Accelerator HERA

The particle accelerator HERA was the only electron-proton collider of its time. Before HERA, the proton structure was studied only in fixed target collisions. With its larger center-of-mass energy of $\sqrt{s} = 318$ GeV high precision measurements of the proton structure function F_2 as well as various other analyses were possible. Therefore the experimental data of the HERA experiments H1 and ZEUS are essential in the determination of parton densities.

In figure 2.1 the storage ring is shown, along with all four experiments and the pre-accelerators DESY and PETRA. These accelerated either electrons or positrons up to an injection energy of 12 GeV, while the protons where injected into HERA at

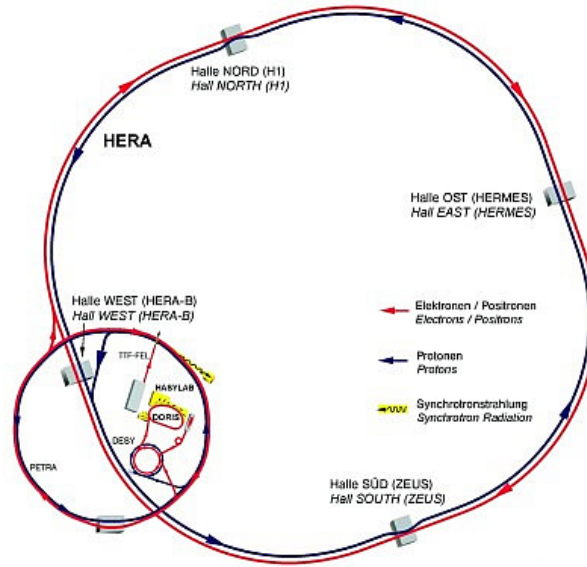


Figure 2.1: *The HERA storage ring and its experiments. The pre-accelerators PETRA and DESY can also be seen.*

40 GeV.

HERA was a storage ring located in Hamburg with a circumference of 6.3 km. After the luminosity upgrade in the years 2000 - 2003 the HERA II phase began. In this time, from 2004 - 2007, protons were accelerated to energies of 920 GeV and electrons to energies of 27.5 GeV, designed to reach luminosities of $\mathcal{L} = 7.4 \cdot 10^{31} \text{ cm}^{-2}\text{s}^{-1}$. Four experiments were using the electron and proton beams for their studies: the HERMES collaboration collided polarized electrons accelerated by HERA with fixed gas targets, thereby studying the spin structure of the proton; the HERA-B collaboration studied CP-violations in the production of heavy mesons by colliding the proton beam with wire targets of different densities; at the experiments H1 and ZEUS the electron and proton beams collided head-on to study the structure of the proton.

The colliding particles were accelerated in bunches. The electrons bunches consisted of $\sim 10^{11}$ particles and moved clockwise around HERA, the proton bunches of $\sim 10^{12}$ particles moved counterclockwise. The bunches collided at a frequency of ~ 10 MHz leaving a time span of 96 ns in between collisions.

During the whole operation time of HERA from 1992 to 2007, the H1 experiment was able to gather an integrated luminosity of 500 pb^{-1} .

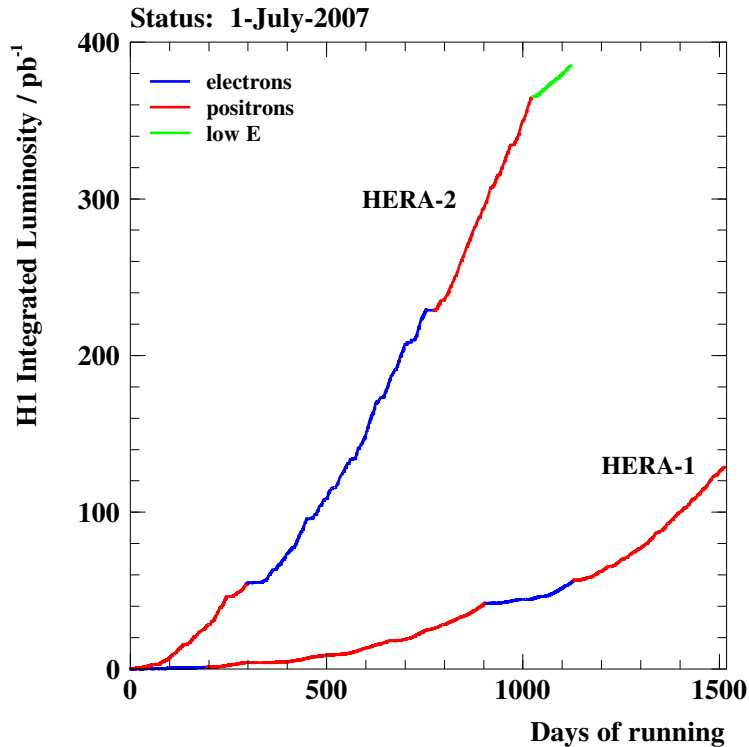


Figure 2.2: *Integrated Luminosity taken by the H1 detector over time. The luminosities gathered before the upgrade (HERA-1) and after the upgrade (HERA-2) are shown separately. The periods when HERA was operated with electrons are highlighted in blue, the red curves show the periods with positrons. The green curve at the end of HERA operation shows the luminosity gathered during the low proton energy runs.*

Luminosity Upgrade

In 2000 HERA was upgraded with new focusing magnets to reach higher luminosities. The focussing magnets were installed inside the H1 detector, so that part of the calorimeter measuring the energy of the scattered electron or positron had to be removed (see sec. 2.3.2 for more details).

Figure 2.2 shows the integrated luminosity gathered by the H1 detector during the entire time of operations. A comparison of the curves labeled HERA-1 and HERA-2 shows that the HERA upgrade successfully increased the luminosity.

Run Periods

HERA was operating with both electrons and positrons. For purposes of trigger efficiencies and calibration testing the HERA II phase is divided in this analysis into

four running periods depending on the accelerated particles:

- 2004 e^+ : during most of the year 2004 positrons were accelerated
- 2004/05 e^- : in the end of 2004 HERA switched to electrons
- 2006 e^- : until the middle of 2006 HERA was operated with positron
- 2006/07 e^+ : from mid 2006 to 2007 positrons were used

From march 2007 to its shutdown in July 2007 HERA was operated with lower proton energies of 460 GeV and 575 GeV.

2.2 The Detector

The detector is introduced in much detail in [14]. For the purpose of measuring momenta a right-handed coordinate system is defined. The origin is defined by the nominal interaction point, with the z -axis pointing in the proton direction and the y -axis pointing upwards. Cylindrical coordinates are used with the azimuthal and polar angles ϕ and θ , respectively.

Figure 2.3 shows a schematic side view of the H1 detector showing its most basic ingredients. The inner part consists of the tracking system, which is enclosed by the backward calorimeter SpaCal at the back and the liquid Argon calorimeter in the central region and in the front.

A superconducting coil surrounds the calorimeters and creates a homogeneous magnetic field of 1.15 T so that momenta can be measured. The central muon detector CMD surrounds the whole detector and also serves as a return yoke for the magnetic field. Outside this the forward muon detector FMD detects muon with small polar angles, θ_μ .

2.3 Calorimetry at H1

The H1 detector had two dedicated systems for energy measurements: the Liquid Argon calorimeter (LAr) [15] for the forward and central region and the Spaghetti Calorimeter (SpaCal) [16] for the backward region. Because of the asymmetric energies of the colliding particles jets were found in the central and forward region with energy deposits in the liquid argon calorimeter, while for $Q^2 < 100 \text{ GeV}^2$ the electron scattered under a large polar angle $\theta_{e'}$ and could be detected in the SpaCal.

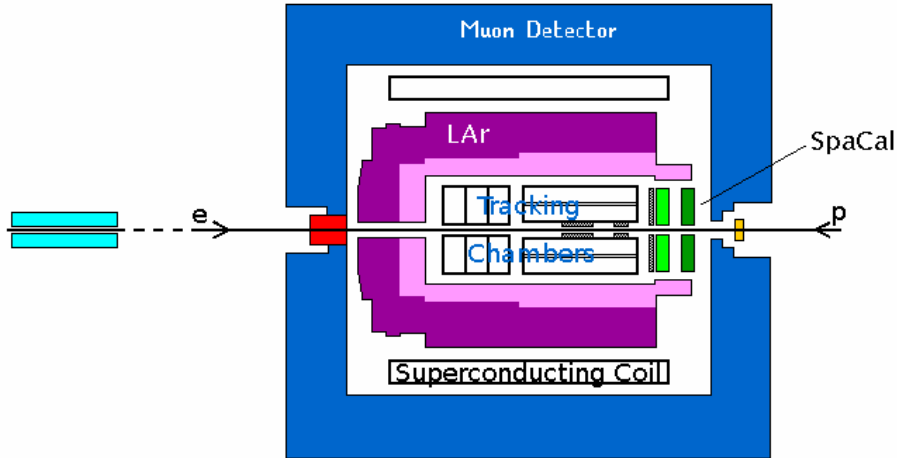


Figure 2.3: *Side view of the H1 detector and its main components: the Central Muon Detector (CMD), the superconducting coil creating the uniform magnetic field, the Liquid Argon calorimeter (LAr), the tracking chambers around the interaction point and the Spaghetti Calorimeter (SpaCal) used for measuring the scattered electron properties at low Q^2 . Protons move in the positive (coming in from the right in the picture), electrons in the negative z -direction.*

2.3.1 The Liquid Argon Calorimeter

The LAr consists of an inner part for measuring energies of electromagnetically interacting particle and an outer part for measuring energies of hadrons. It is a sampling calorimeter which utilizes two different materials for creating the particle shower (absorber material) and measuring the energy (active material). In both parts liquid argon is used as active material. Absorber materials are lead in the electromagnetic and steel in the hadronic section. The liquid argon is cooled by a helium driven cryostat in which the calorimeter is embedded. The circulating helium gas is cooled by an external liquid nitrogen heat exchanger.

Plates of the absorber materials are oriented in a way that the inclination angle of particles originating at the interaction point is always larger than 45° . The space between the plates is filled with liquid argon, giving the calorimeter the alternating structure of active and absorber material common to all sampling calorimeters. The material in the calorimeter amounts to 20 - 30 radiation lengths in the electromagnetic section and 5 - 8 interaction lengths in the hadronic section.

Test beam measurements have shown that the energy resolution of the LAr is

2 The H1 Experiment

$\sigma_{em}(E)/E \approx 12\%/\sqrt{E/GeV} \oplus 1\%$ in the electromagnetic part and $\sigma_{had}(E)/E \approx 50\%/\sqrt{E/GeV} \oplus 2\%$.

In this analysis the LAr calorimeter was used for the measurement of the inelasticity $y_{e\Sigma}$, which was reconstructed with the $e\Sigma$ -method as described in section 3.2.1.

2.3.2 The Backward Calorimeter SpaCal

The Spaghetti Calorimeter was mainly used for measuring the energy of the scattered electron. At scattering angles where there is no information from the tracking chambers on the scattered electron, the SpaCal also allowed for a reconstruction of $\theta_{e'}$.

The energy of the scattered electron was measured in the electromagnetic section of the backward spaghetti calorimeter SpaCal. Using lead as absorber material and scintillating fibers as active material it provided an energy resolution of $\sigma_E/E \approx 7\%\sqrt{E/GeV} \oplus 1\%$ and an angular resolution of ~ 2 mrad for the scattered electron.

The SpaCal was located in the backward region of the detector at $z = -160$ cm, originally covering the angular region $153^\circ < \theta < 177.5^\circ$. After the luminosity upgrade of HERA parts of the inner cells of the calorimeter had to be removed to make space for a new focusing magnet. This rebuilding led to a reduced angular coverage of $153^\circ < \theta < 174.5^\circ$.

To measure energies of both leptons and photons on one side and hadrons on the other the SpaCal also featured a hadronic section which was located behind the electromagnetic one. Both sections consisted of cells of scintillating fibers embedded in lead sheets. The scintillation light was transported along the fibers and read-out by photo multipliers positioned at the end of each section.

Since electromagnetic and hadronic showers behave very differently the design of the cells of each section differs. The following table lists some of the design parameters for the hadronic and the electromagnetic sections which take into account the differences in the shower behavior:

	Electromagnetic section	Hadronic section
Fiber diameter	0.5 mm	1 mm
Lead-to-fiber ratio	2.3 : 1	3.4 : 1
Cell size	$40.5 \times 40.5 \text{ mm}^2$	$119.3 \times 119.0 \text{ mm}^2$
Depth	$27.5 \chi_0$	$1.02 \lambda_{int}$

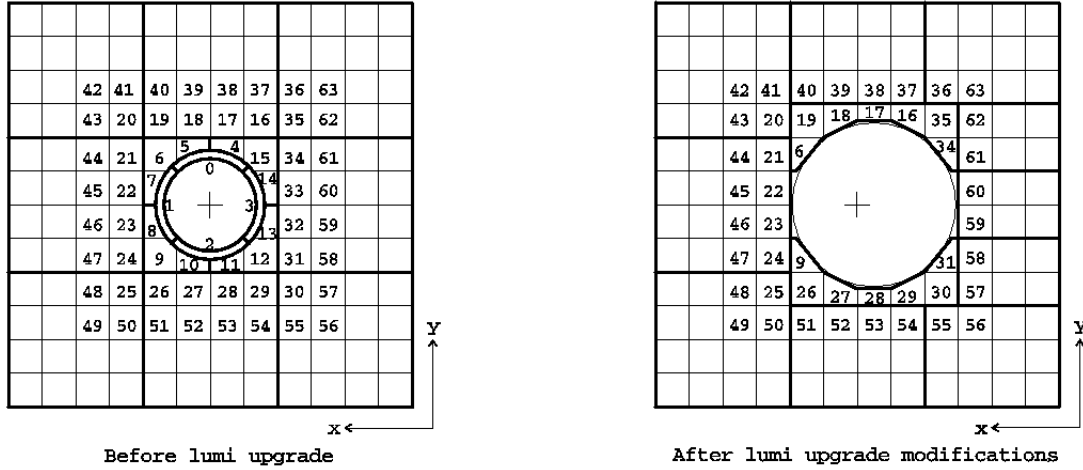


Figure 2.4: Changes to the inner part of the SpaCal after the luminosity upgrade.

The SpaCal replaced the Backward Electron Magnetic Calorimeter (BEMC) which was operated as the backward calorimeter of H1 until 1995.[17] Its size was therefore constrained by the already existing detector. For the electromagnetic section this is not a severe constraint, since a depth of ~ 28 radiation lengths (χ_0) is mostly enough to fully contain the electromagnetic shower. On the other hand the hadronic section is only ~ 1 interaction length (λ_{int}) deep, so that hadronic showers can partly escape detection. In this thesis the hadronic part was only used for identification of the electron by demanding that the energy deposited there was less than 15% of the energy of the scattered electron.

The Inner Part of SpaCal

Figure 2.4 shows the changes applied to the inner part of the SpaCal after HERA's luminosity upgrade. The most inner cells, numbers 0 through 4, have been removed and the surrounding cells cut. Note that with respect to the beam axis (the cross in fig. 2.4) the cut was asymmetric.

2.4 The Central Tracking Devices

Figure 2.5 shows a cross section of the Central Tracking Devices (CTD) of the H1 detector in the $r\phi$ -plane. The CTD covered an angular range of approximately $15^\circ < \theta_{track} < 165^\circ$. Starting with the devices closest to the beam pipe moving, the CTD

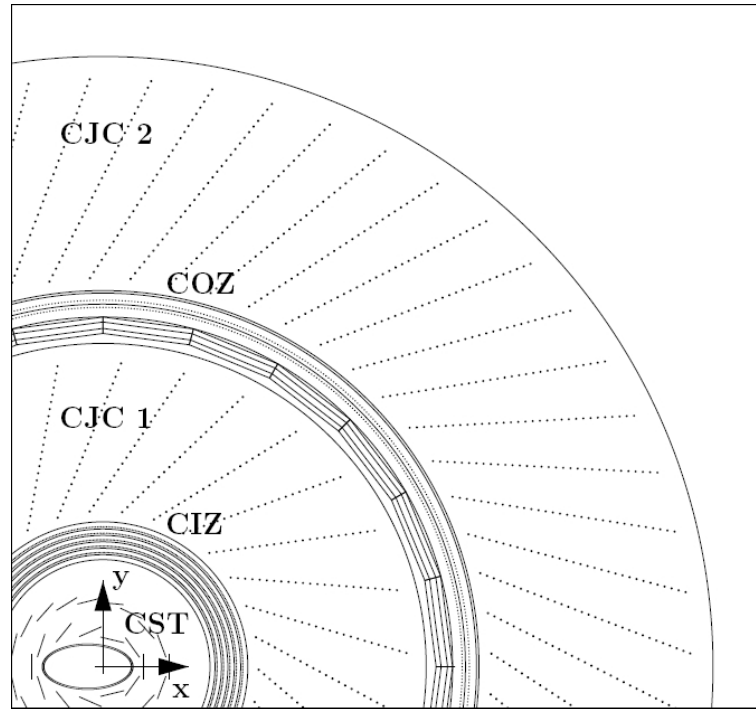


Figure 2.5: Cross Section of the central tracking chambers in the x - y -plane.

consisted of

- the central, forward and backward silicon trackers (CST, FST and BST) surrounded the interaction point at $z = 0$ and were installed close to the beam pipe to improve tracking and determination of the interaction vertex,
- the Central Inner Proportional Chamber (CIP) surrounded the silicon trackers and was used mainly for triggering purposes,
- the first of two chambers to measure the z -component of track momenta, the Central Inner Z-Chamber (CIZ) sat at the outside of the CIP,
- the Central Jet Chamber 1 (CJC1) was the inner of two drift chambers measuring the transverse momentum of tracks,
- the Central Outer Proportional Chamber (COP),
- the Central Outer Z-Chamber (COZ)
- and the CJC2.

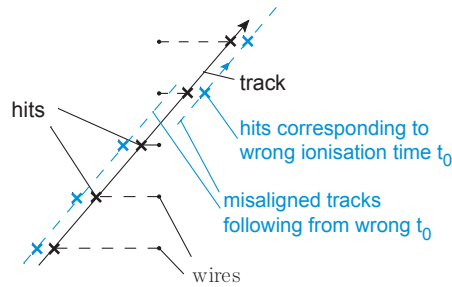


Figure 2.6: Tracks are aligned by varying the ionization time t_0 . The hits on opposite sides of the wires do not align when a wrong t_0 is used.

2.4.1 The Jet Chambers

The Central Jet Chambers were drift chambers composed of 30 radial cells for the CJC1 and 60 radial cells for the CJC2, which had a larger radius. The cells were tilted against the chamber radius by 30° so that tracks from the interaction vertex have a high probability of crossing at least one cell boundary. In each cell in the CJC1 24 signal wires were installed parallel to the z -axis, whereas the cells in the CJC2 consist of 36 wires each.

The cells were filled with a gas. The gas was ionized when charged particles moved through the chambers. A mainly uniform electric field between the anode signal wires and the cathode wires caused the ionization electrons to move towards the signal wires perpendicular to the wire plane. The collisions of the ionization electrons with the gas molecules caused secondary ionization, so that a whole ionization avalanche was created. Upon reaching the signal wires this caused a charge excess in a wire, which could be measured at both of its ends.

The charge excess at the ends of a wire differ depending on where the wire was struck. In principle it was possible to measure the z -component of the track momentum with the jet chambers by exploiting this charge difference, but the resolution of $\sigma_z = 22$ mm was not good enough for the precision needed for most measurements carried out with the H1 detector. The z -chambers offered a much higher precision for the task.

Drift time Measurement

Measuring the exact position of a hit (the position where the ionization occurred and, thus, where the particle passed through the detector) is done by measuring the drift time of the electrons. The drift time is the difference between the ionization time

2 The H1 Experiment

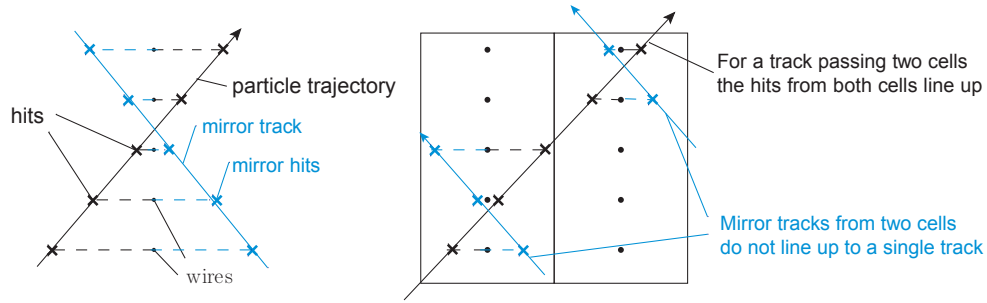


Figure 2.7: *Schematic illustration of mirror hits causing mirror tracks (left). Mirror tracks in two cells do not line up (right).*

when the charged particle ionized the gas and the arrival time when the ionization avalanche reached the wire.

The ionization time t_0 is in general given by the bunch crossing time. But this is not exactly known because the scattering can occur anywhere in the bunches, which are a few meters long. Thus the ionization time is determined by varying the time of the bunch crossing so that hits on opposite sides of the wires in a cell are aligned (see fig. 2.6).

The arrival time is given by the signal in the wire. For a given gas or gas mixture the velocity of the ionization electrons is known, so that the precise distance of the hit from the wire can be determined.

Mirror Tracks in the Jet Chambers

This does not yet give the exact position of the hit, because it is still not known on which side of a wire the gas was ionized. The hit on the wrong side of the wire is called mirror hit, a series of mirror hits producing mirror tracks. This is illustrated on the left of figure 2.7. In order to find the correct position of the hit, the cells of the jet chambers were tilted by 30° against the chamber radius. Thus most tracks cross two cells, and mirror hits from two cells are easily identified because they don't connect to a single line, as can be seen from the right illustration of figure 2.7.

Track Momentum Measurement

In the H1 detectors particles were moving in a uniform magnetic field parallel to the z -axis of field strength $B_z = 1.15$ T. Inside that field tracks of particles are curved in the $r\phi$ plane with a curvature κ , which can be easily measured. The transverse momentum of the tracks p_t^{track} is proportional to the inverse of κ :

$$p_t^{track}[GeV] = -Q \frac{0.3 \cdot B_z[T]}{\kappa[m^{-1}]} . \quad (2.1)$$

The spatial resolution of the hit position measurement in the $r\phi$ -plane was $\sigma_{r\phi} = 170\mu m$ and resulted in a resolution of the transverse momentum of $\sigma_{p_t}/p_t^2 = 0.005 \text{ GeV}^{-1} \oplus 0.015$ [18].

2.4.2 The Central Silicon Tracker

Of the silicon trackers only the central one was used in this analysis. The CST directly surrounded the elliptical beam pipe at the nominal interaction point and was used as a vertex detector. Its two layers consisted of silicon strips arranged in ladders. It covered polar angles of $30^\circ < \theta < 150^\circ$, achieving a resolution of $\sigma_{r\phi} = 12 \mu m$ in the $r\phi$ -plane and $\sigma_z = 25 \mu m$ in z . With the CST the distance of closest approach (dca) of a track was measured with an accuracy of $\sigma_{dca} \approx (33 \mu m \oplus 90 \mu m)/p_t[GeV]$, with uncertainties arising from the intrinsic resolution (first term) and from multiple scatterings in both beam pipe and CST (second term).

2.4.3 The Central Proportional Chambers

The CIP and COP were multi-wire proportional chambers (MWPCs) with wires strung parallel to the beam axis. The inner chamber was located between the silicon trackers and the CJC1, the outer between the two jet chambers.

Replaced by a new five layer MWPC during the detector upgrade the CIP had a fast response time and was therefore used for online event selection. It covered a polar angular range of $11^\circ < \theta < 169^\circ$.

2.4.4 The Z-Chambers

The exact z -components of particle momenta was determined in the inner and outer z -chambers CIZ and COZ. These were drift chambers with wires not parallel to the z -axis, but tilted by 45° in case of the inner and 90° in case of the outer chamber. With these a resolution in z of $\sigma_z \approx 350 \mu m$ was achieved.

2 The H1 Experiment

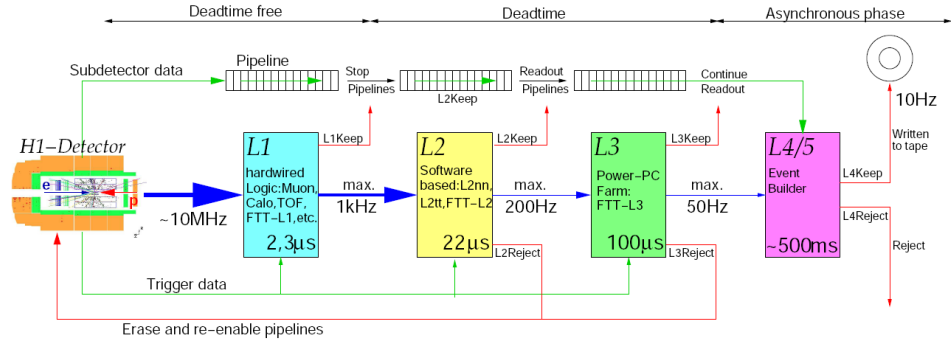


Figure 2.8: *The H1 trigger scheme and its multiple levels.*

2.5 Triggering Physics Events at H1

In collider experiments such as HERA not all occurring particle collisions contain information about interesting physical processes. For this reason the collision rate at HERA was much higher than the storage capabilities and the readout rates of the detectors in order to guarantee statistically significant yields of interesting physics events. These are then preselected by sophisticated trigger schemes.

The H1 multi-level trigger scheme - outlined in figure 2.8 - reduced HERA's bunch crossing frequency of 10.4 MHz by roughly six orders of magnitude to a final readout frequency of the order of 5 to 10 Hz.

Level 1

The first trigger level L1 analyzed bunch crossing information stored in a pipeline. Since the L1 decision took $2.3\mu\text{s}$ the pipelines stored the information of 22 bunch crossings so that the L1 decision was dead time free. The decision was made by about 200 trigger elements combined into 128 sub-triggers named S0 to S127. If at least one of the subtriggers fired the readout into the pipelines was stopped and the dead time began. The signal then send to the central trigger logic (CTL) was called L1Keep.

Level 2

Once an event had passed the first trigger level the information in the current pipeline was analyzed by either a topological trigger system (L2TT) or by a neural network (L2NN). The topological triggers selected interesting events based on a grid in θ and ϕ , while the neural network was trained to select events based on sub-detector

information. The L2 decision took about $22\mu\text{s}$. If L2 rejected an event the pipeline was erased and the dead time ended. An event that passed L2 was fully being read out for a more detailed analysis by the higher trigger levels.

Level 3

The third trigger level L3 was running while the information from the pipeline was being read out and stopped the readout if the event was rejected. The readout continued if the event was kept to be further analyzed by the fourth and fifth trigger levels. L3 was part of the Fast Track Trigger (FTT) installed in 2006. In addition to track information it relied on the calorimeters and the muon system to decide if an event was kept. This decision took place in about $100\mu\text{s}$ and reduced the readout frequency to about 50 Hz.

Level 4

The last trigger level for the online data selection, L4, has access to the full event information from the event builder. It rejects background events from interaction of the beams with gas remnants in the beam pipe or with the wall of the beam pipe. At this stage the physics finders sort the selected events into the different physics categories. Events passing the L4 conditions are written to tape with a rate of approximately 10 Hz.

L4 is further used to fill certain histograms online for quality monitoring by the shift crews.

2.6 Detector Simulation and Reconstruction

For the simulation of effects of the H1 detector on particles passing through the collaboration has developed the software package `h1sim` based on the detector simulation tool GEANT [19]. It simulates the behavior of the H1 detector by creating tracks and energy deposits from four-momenta of particles generated by MC event generators. The GEANT package takes account of electromagnetic and nuclear interactions during the particles' passage through matter.

The event information created by `h1sim` is then run through the whole reconstruction cycle. In this step specific run dependent information is taken into account to match the reconstruction of the data. The output can then be used for a compari-

2 The H1 Experiment

son of hadron and detector level information to correct for detector inefficiencies and migration effects (see section 3.6).

3 D^* Meson Cross Sections

The charmed meson $D^{*\pm}$ has been used in previous HERA studies to measure charm quark production in electron-proton scattering. It consists of a charm or anti-charm and a anti-down or down quark. The decay channel $D^{*\pm} \rightarrow D^0 \pi_s^\pm \rightarrow K^\pm \pi^\mp \pi_s^{\pm 1}$ is reviewed in this chapter after a short introduction to charm production.

3.1 Heavy Quark Physics at H1

Heavy quark production at HERA offers a direct sensitivity to the gluon density because its dominant production mechanism in electron-proton scattering is boson gluon fusion, as depicted in figure 3.1. The large masses of charm and bottom quarks serve as hard scales in the hard scattering and ensure the applicability of perturbative QCD.

Since in neutral current processes heavy quarks and anti-quarks are always produced in pairs, in the HERA phase space the top quark cannot be produced because the mass of a top quark pair, $2 \cdot m_t \approx 350$ GeV, is larger than the center-of-mass energy of the electron-proton system, $\sqrt{s} = 318$ GeV.

At HERA heavy quark production is studied by searching for decay products of charm or beauty mesons, or by studying jets associated with the heavy quarks. The latter can be done by selecting leptons or mesons with certain properties implying the heavy quark origin of the jets. In the following charm production measurements are presented which used D^* mesons as tags of charm quarks. An overview of D^* production measurements at both H1 and ZEUS is given, followed by a short discussion of beauty production measurements.

¹ π_s indicates the “slow pion”, i. e. the low momentum pion from the D^* decay.

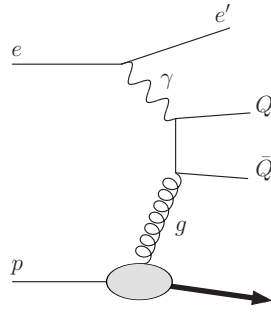


Figure 3.1: *Dominant charm quark production mechanism in electron-proton scattering.*

3.1.1 Charm Production Measurements

Charmed mesons like D^\pm or $D^{*\pm}$ predominantly decay into kaons and pions, which leave tracks in the detector. But even with particle identification methods like determination of the energy loss dE/dx it is impossible to know with certainty which kind of particle causes which track. That is why the basic method is to look for all possible combinations of tracks and for each combination make an arbitrary assumption which track belongs to which particle. Under this assumption masses are assigned to tracks, so that energies and momenta can be calculated. With the resulting kinematics it is then possible to calculate the invariant mass of the originator meson, e.g. a D^* . In the end, fits to mass resonances determine the number of produced mesons. This method is applied here and explained in more detail in section 3.5.

D^* Production at H1 with HERA II Data

There have been various D^* production measurements in DIS at H1 and ZEUS using the data from the HERA I period [20, 21, 22, 23, 24, 25, 26]. The HERA II data collected by the H1 detector offers much larger statistics due to both higher luminosity as well as the more efficient Fast Track Trigger (FTT) system introduced in 2005 [27] (see section 3.3).

In DIS this fact has been exploited to study the production of D^* mesons in electron-proton collisions in three different Q^2 ranges:

- low Q^2 : $2 \text{ GeV}^2 < Q^2 < 5 \text{ GeV}^2$ (this analysis)
- medium Q^2 : $5 \text{ GeV}^2 < Q^2 < 100 \text{ GeV}^2$ (Andreas Jung [1])
- high Q^2 : $100 \text{ GeV}^2 < Q^2 < 1000 \text{ GeV}^2$ (Martin Brinkmann [3],[2])

These three measurements cover the Q^2 range $2 \text{ GeV}^2 < Q^2 < 1000 \text{ GeV}^2$ of nearly three orders of magnitude. The integrated luminosity in these analyses is much higher than in a comparable study of the ZEUS collaboration using HERA I data [26]. There an integrated luminosity of roughly 82 pb^{-1} was analyzed, compared to about 340 pb^{-1} (see section 3.10) in the HERA II studies at H1.

Although in [25] the phase space extended to a minimum $Q_{min}^2 = 1 \text{ GeV}^2$ compared to $Q_{min}^2 = 2 \text{ GeV}^2$ used here, this analysis offers a finer binning in Q^2 and a dedicated measurement of the transverse momentum spectrum at low Q^2 .

D^* Production with Jets

It is also possible to study jet events with D^* mesons. Especially interesting are dijet events, because if a D^* meson is found in a dijet event and associated with one of the jets, it is possible that the second jet also stems from a charm quark. This makes it possible to directly study the two charm quarks produced in boson gluon fusion. Even if the second jet originates from a gluon or another quark, which happens especially at large pseudorapidities η^{jet} , such events offer interesting possibilities to study underlying phenomena like different models of gluon density evolution. Examples of such a study are found in [28] for DIS and in [29] for photoproduction.

In order to study both charm quarks produced in boson gluon fusion, the double tagging method can be applied. In addition to the selection of a D^* meson to tag at least one charm quark, the second charm quark can also be associated with a fragmentation or decay product of heavy quarks or mesons, for example a muon. For photoproduction this has been done in [30].

3.1.2 Beauty Production Measurements

Beauty mesons are harder to tag. One example is the search for events with two jets and a lepton that can be associated with a jet. Because the background from light and charm quark production cannot be neglected, in reference [31] the beauty fraction samples is enhanced by requiring that the transverse momentum component of the lepton relative to the jet momentum, p_t^{rel} , has to exceed a certain minimum, making use of the fact that in beauty production events p_t^{rel} features a harder spectrum.

3.2 The Electron Energy Measurement

In deep inelastic scattering experiments event kinematics are mostly determined by a precise measurement of the energy of the scattered electron. This section first introduces the methods for the reconstruction of these event kinematics in section 3.2.1. A test of the calibration of the electron energy measurement and a determination of the related uncertainty is presented in section 3.2.3. This test results in a systematic uncertainty on the measurement of the scattered electron $E_{e'}$.

3.2.1 Reconstruction of Kinematic Variables

A precise measurement of DIS processes requires high precision measurements of the event kinematics: the four-momentum transfer Q^2 , the inelasticity y and the quark momentum fraction x . Because these variables are related by equation (1.5) and the center of mass energy s is known it is sufficient to reconstruct only two of those variables. There are various methods to achieve a good resolution in these variables depending on the process and the region of phase space one wants to study. This section introduces the methods used in this analysis: the electron method, the sigma method and the electron sigma ($e\Sigma$) method.²

The electron method uses only the measurement of the scattered electron's energy $E_{e'}$ and its scattering angle θ_e to reconstruct the event kinematics in the following way (the lower index e indicates the electron method):

$$y_e = 1 - \frac{E_{e'}}{2E_e}(1 - \cos \theta_e) = 1 - \frac{E_{e'}}{E_e} \sin^2 \frac{\theta_e}{2} \quad (3.1)$$

$$Q_e^2 = 2E_e E_{e'}(1 + \cos \theta_e) = \frac{E_{e'} \sin^2 \theta_e}{1 - y_e} \quad (3.2)$$

It provides a good resolution of Q^2 and y at high inelasticities and is independent from any measurement of the hadronic final state. But at low inelasticities it becomes sensitive to initial state QED radiation of the electron.

Less sensitive to initial state QED radiation the Σ method makes use of energy balance between initial and final state:

²For a more detailed presentation of reconstruction of kinematics in DIS see [32].

$$\sum_i E_i - \sum_i p_{z,i} = E_p + E_e - (p_{z,p} + p_{z,e}) \quad (3.3)$$

$$= 2E_e \quad (3.4)$$

The index i runs over all final state particles including the scattered electron. The sum over all final state particles is defined as $\Sigma = \sum_i (E_i - p_{z,i})$.

Substituting $2E_e$ with Σ and $E_{e'}(1 - \cos\theta_e)$ with $E_{e'} - p_{z,e'} = \Sigma - \Sigma_{hfs}$, where $\Sigma_{hfs} = \sum_{i \in hfs} (E_i - p_{z,i})$, equation (3.1) allows for a redefinition of y which is less sensitive to initial state radiation and in terms of which the photon virtuality Q^2 and the momentum fraction x can also be redefined:

$$y_\Sigma = \frac{\Sigma_{hfs}}{\Sigma} \quad (3.5)$$

$$Q_\Sigma^2 = \frac{E_{e'} \sin^2 \theta_e}{1 - y_\Sigma} \quad (3.6)$$

$$x_\Sigma = \frac{Q_\Sigma^2}{2\Sigma E_p y_\Sigma} = \frac{Q_\Sigma^2}{2\Sigma_{hfs} E_p} \quad (3.7)$$

At low inelasticities the Σ -method offers a better resolution, but especially at higher y the electron method remains superior. Especially the resulting resolution of Q_Σ^2 is worse than the resolution of Q_e^2 . A combination of these two methods, the $e\Sigma$ -method takes the photon virtuality from the electron method, the momentum fraction from the Σ -method and redefines the inelasticity accordingly:

$$y_{e\Sigma} = \frac{Q_e^2}{x_\Sigma \cdot s} = \frac{2E_e \Sigma}{(\Sigma + E_{e'}(1 - \cos\theta_e))^2} \quad (3.8)$$

$$Q_{e\Sigma}^2 = Q_e^2 \quad (3.9)$$

$$x_{e\Sigma} = x_\Sigma \quad (3.10)$$

This method, while retaining the excellent Q^2 resolution of the electron method and the x resolution of the Σ -method, achieves a good inelasticity resolution at low y similar to the Σ -method and also a better resolution at high y , although not quite as high as the resolution of y_e .

As in another D^* meson analysis of the HERA II period[1] the $e\Sigma$ -method is used for both single and double differential cross section determinations.

A fourth method for reconstructing event kinematics, the double angle method, relies purely on measured angles of the hadronic final state and the electron, making it independent from energy measurements in the SpaCal. This method is used here to test the calibration of the energy measurement of the scattered electron and is presented in the next section.

3.2.2 The Electron Selection

Electrons are reconstructed in the SpaCal. Energy clusters are selected with a radius $r_{cluster} < 4$ cm in the electromagnetic part of the calorimeter because leptons create narrower showers than hadrons. Furthermore the fraction $f_{had} = E_{had}/E_e$ of the energy E_{had} measured in cells of the hadronic part directly behind the selected electromagnetic cluster is restricted to $f_{had} < 3\%$. This is done mostly to suppress background from photoproduction events where the scattered electron escapes the detector and a signal in the SpaCal could be falsely identified as an electron.

In addition inefficient and deficient regions in the SpaCal, termed *dead cells*, are rejected by fiducial cuts in the electron selection. Two circular cuts of 10 cm radii have been applied on the radial distances r_{Spac} and r_{beam} of the selected energy cluster from the center of the SpaCal and the beam axis, respectively, to avoid energy leaking effects at the edge of the detector. These two cuts were motivated by the asymmetry of the distribution where one cut alone would not have avoided cluster reconstruction at the edge of the SpaCal. While in the medium Q^2 analysis a more conservative radius cut of 12 cm was used, here it was necessary to lower the cut in order to reach the low Q^2 values which were the aim of this analysis.

The basic electron selection cuts are summarized in table 3.1. Dead cell cuts are not given.

Criterion	Purpose
$r_{cluster} < 4$ cm	Select leptonic cluster
$f_{had} < 3\%$	Suppress photoproduction background
$r_{Spac}, r_{beam} > 10$ cm	Avoid energy leaking at the edge of SpaCal

Table 3.1: *Criteria for the selection of the scattered electron and their purposes.*

Excluded Regions in the SpaCal

Figure 3.2 shows the distribution of reconstructed electron clusters in the SpaCal for all four run periods defined in section 2.1 after all selection cuts (see tables 3.3, 3.4 and 3.5). Excluded regions are shown as blue boxes and circles. Only the central part of SpaCal with $|x|, |y| < 30$ cm is shown. All distances are given in the H1 coordinate system.

In the years 2004 and 2005 a certain amount of cells in the SpaCal were deficient and therefore excluded from the data selection (blue boxes in fig. 3.2). In 2006 these cells were replaced, so that less cells had to be excluded.

Cells around $y = 0$ cm were hit by synchrotron radiation from the electron beam and therefore taken out of the trigger. Clusters reconstructed in these cells were excluded by applying a box cut of ~ 8.4 cm \times 18 cm.

Asymmetry of the $\phi_{e'}$ Spectrum

At $2 \text{ GeV}^2 < Q^2 < 5 \text{ GeV}^2$ most electron clusters were positioned close to the beam axis. The asymmetric shape of the SpaCal with respect to the beam axis³ then resulted in an asymmetric cluster distribution in the SpaCal. In figure 3.2 this asymmetry is visible in the fact that the clusters form a crescent around the beam axis instead of a ring.

This leads to a $\phi_{e'}$ spectrum which is falling from $\phi_{e'} = 0^\circ$ to both positive and negative $\phi_{e'}$ (see fig. 3.5). In addition the box cut around $y_{SpaCal} = 0$ cm leads to a dip in the distribution of $\phi_{e'}$ around $\phi_{e'} = 0^\circ$.

³In the H1 coordinate system the center of the SpaCal lay at $x = 2.5$ cm and $y = 0.5$ cm.

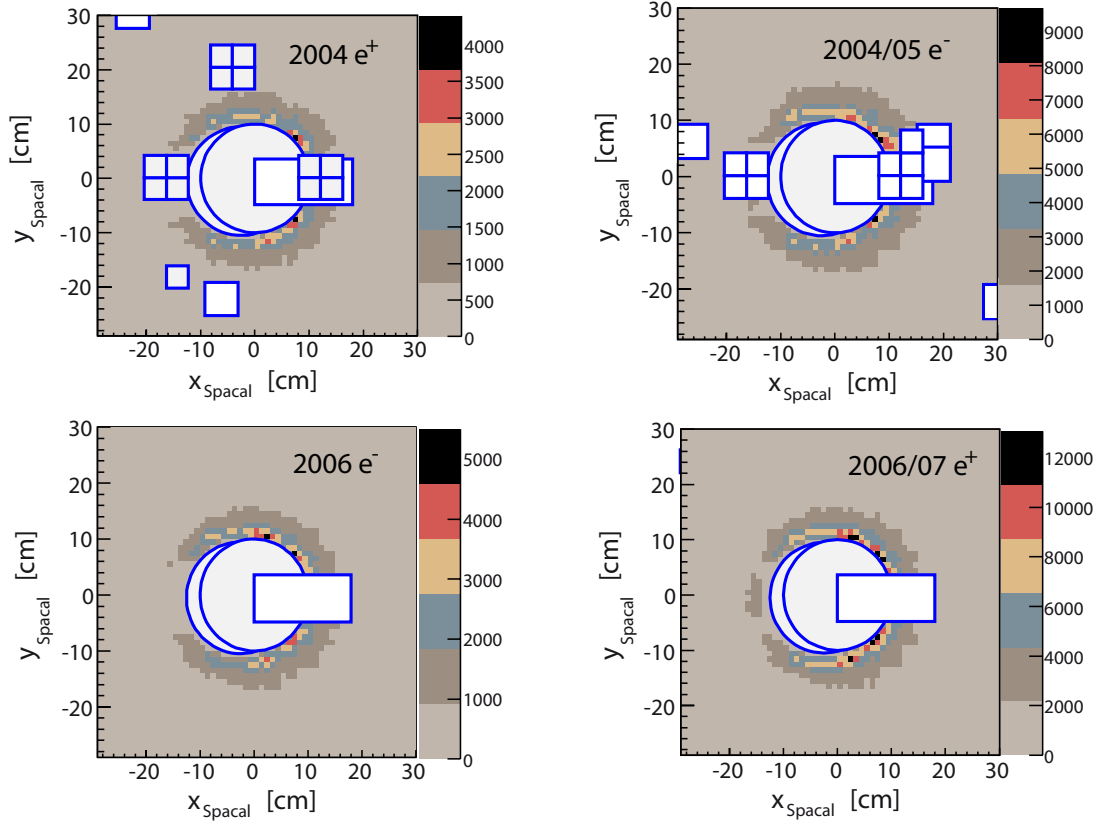


Figure 3.2: *Two dimensional distribution of x and y , i.e. the distances of selected electron clusters to the beam axis, in the central part of the detector in bins of $1 \text{ cm} \times 1 \text{ cm}$. Shown are the distributions for the four run periods defined in section 2.1 after all selection cuts (see tables 3.3, 3.4 and 3.5). Blue boxes and circles indicate areas excluded from the data selection. The color palettes on the right indicate how many clusters are reconstructed in the inclusive sample.*

3.2.3 Testing the Calibration of the Electron Energy Measurement

The calibration of the measurement of the energy $E_{e'}$ of the scattered electron is done using the *double angle (DA) method*[32]. It is used in this thesis as a test of the calibration. This method offers a better resolution in the determination of the energy of the scattered electron in a certain constrained phase space and is independent from energy measurements in the SpaCal.

The kinematics of the final state are over-constrained and one can therefore determine the energy of the scattered electron purely by measuring its polar angle $\theta_{e'}$ and the effective scattering angle of the hadronic final state, γ_h ⁴:

$$\tan \frac{\gamma_h}{2} = \frac{(E - p_z)_{hfs}}{p_{t,hfs}} \quad (3.11)$$

With this the inelasticity can be calculated,

$$y_{DA} = \frac{\tan(\gamma_h/2)}{\tan(\gamma_h/2) + \tan(\theta_{e'}/2)}, \quad (3.12)$$

and the energy of the scattered electron evaluates to

$$E_{DA} = E_e \frac{1 - y_{DA}}{\sin^2(\theta_{e'}/2)}. \quad (3.13)$$

This method is called the *double angle method*, because $E_{e'}$ is determined from the measurement of the angles γ_h and $\theta_{e'}$. It has the advantage of being independent from energy measurements in the SpaCal. Instead the electron energy is calibrated against the energy E_e of the incoming electron, which is known with high precision. The sensitivity of γ_h on the calibration of the energy measurement of the hadronic final state is small.

When comparing $E_{e'}$ with E_{DA} one has to ensure that the hadronic final state is well reconstructed. This is done by constraining the effective hadronic angle to the range $15^\circ < \gamma_h < 80^\circ$ and requiring $|y_{DA} - y_e| / (y_{DA} + y_e) < 0.2$, i. e. the inelasticities determined with the different methods should yield similar results. The constraint on γ_h mainly selects events in the region of the kinematic peak⁵. Therefore an additional requirement is $20 \text{ GeV} < E_{e'} < 32 \text{ GeV}$, also rejecting events with a

⁴In the naive parton model γ_h represents the polar angle of the struck quark.

⁵In electron-proton scattering the majority of the events features scattered electrons with an energy close to the energy of the incoming electron, $E_{e'} \approx E_e$. This region is called the *kinematic peak*.

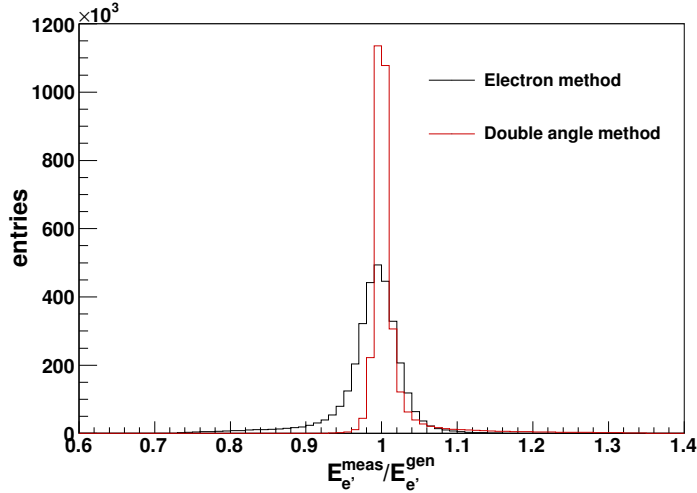


Figure 3.3: Comparison of the resolution of the double angle method and the electron method in the determination of the energy of the scattered electron.

badly reconstructed hadronic final state.

If all of these requirements are fulfilled the double angle method offers a better resolution for the electron energy determination than the electron method. Figure 3.3 shows the distribution of the ratio $E_{e'}^{meas}/E_{e'}^{gen}$ of the measured energy of the scattered electron $E_{e'}^{meas}$ to the generated scattered electron energy $E_{e'}^{gen}$. In the figure $E_{e'}^{meas}$ is either determined by the electron method (black histogram) or by the double angle method (red histogram). The double angle method shows a narrower peak around $E_{e'}^{meas}/E_{e'}^{gen} = 1$ and is therefore on average closer to the generated scattered electron energy than the electron method.

The calibration is now tested by studying the ratio $E_{e'}/E_{DA}$ of the electron energy measured with the electron method, $E_{e'}$, and measured with the double angle method, E_{DA} , as a function of the radial position of the scattered electron in the SpaCal, r_{SpaCal} . This is shown in figure 3.4 for the four running periods. Data is shown in black, Monte Carlo predictions in blue. The double ratio of the two distributions, $(E_{e'}^{data}/E_{DA}^{data}) / (E_{e'}^{MC}/E_{DA}^{MC})$, is shown as yellow triangles.

The double ratio is a measure of how well the detector is understood. If the ratio would be unity at all radii, all uncertainties due to the energy measurement would be corrected for in the determination of efficiencies. However, as can be seen from the figure, at low radii $r_{SpaCal} < 15$ cm the energy measurement is not perfectly understood, and even at large radii the Monte Carlo predictions deviate from the data. Therefore the resulting systematic uncertainty is studied by applying a systematic

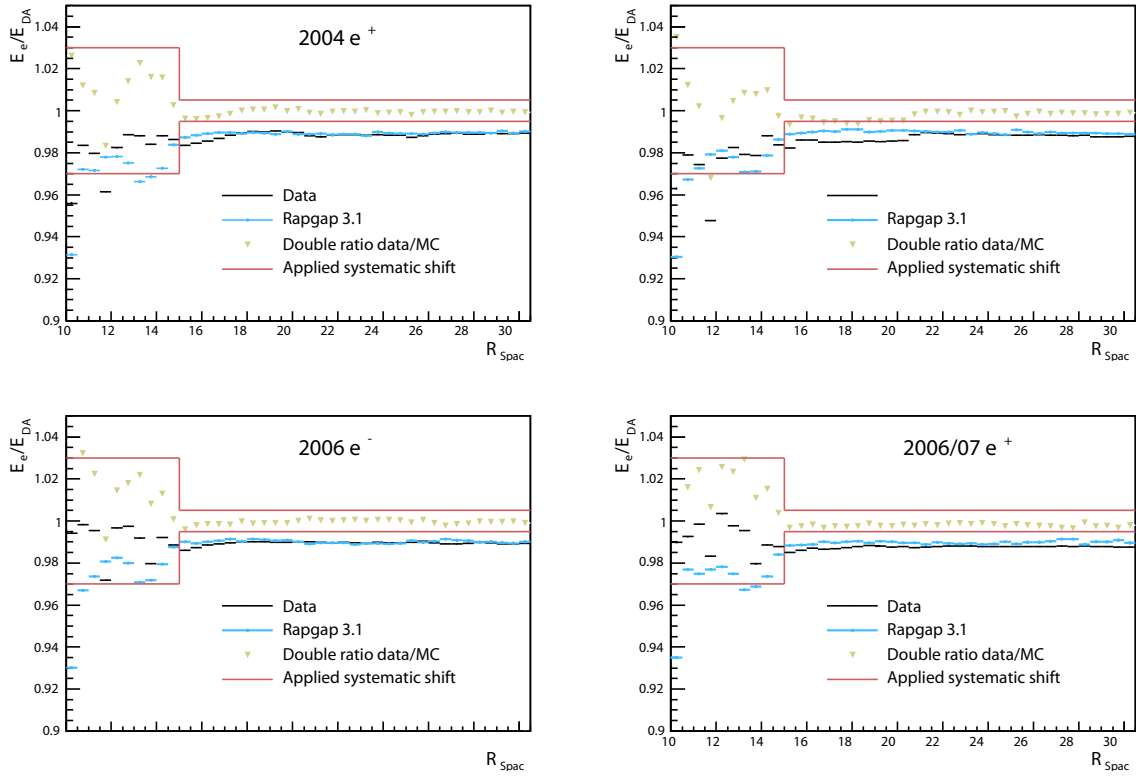


Figure 3.4: *Test of the calibration of the electron method using the double angle method as a reference. Displayed are the ratios of the electron energy measured with the two methods, E_e/E_{DA} , as a function of the radial position in the SpaCal. The data in black is compared to the Monte Carlo predictions in blue. The triangles mark the double ratio data/MC and the red lines indicate the systematic shift applied for determination of the resulting systematic uncertainty.*

shift to the energy scale in the Monte Carlo predictions and taking the difference to the unshifted cross section.

From figure 3.4 a shift $\delta_{em.}$ follows which is larger for $r_{SpaCal} < 15$ cm:

$$\delta_{em.} = \begin{cases} 3\% & \text{for } r_{SpaCal} < 15 \text{ cm} \\ 0.5\% & \text{for } r_{SpaCal} > 15 \text{ cm} \end{cases}$$

In the figure this is indicated by the red line.

The treatment of the systematic uncertainty due to the energy measurement uncertainty and how systematic energy scale shifts are applied is presented in section 3.9.

3 D^* Meson Cross Sections

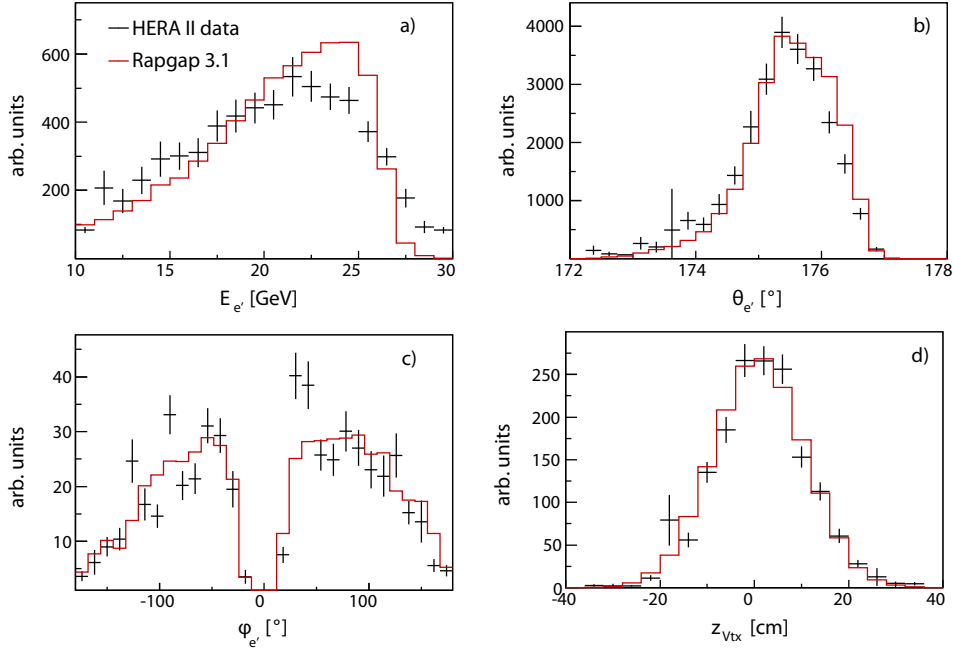


Figure 3.5: Control distributions for the scattered electron observables $E_{e'}$, $\theta_{e'}$, $\phi_{e'}$ and the interaction vertex z_{vertex} .

3.2.4 Control Distributions

A comparison of the MC calculations and the experimental data for the energy $E_{e'}$, the polar angle $\theta_{e'}$ and the azimuth $\phi_{e'}$ of the scattered electron and the z -component of the interaction vertex, z_{vertex} , is shown in figure 3.5. The dip around $\phi_{e'} = 0^\circ$ is due to the box cut around $y_{SpaCal} = 0$ cm shown in figure 3.2.

Figure 3.6 compares MC calculations and data for the observables Q_e^2 , $y_{e\Sigma}$, $p_t^{D^*}$ and η^{D^*} for which differential cross sections have been determined.

These figures show that the measured spectra of the scattered electron energy $E_{e'}$ and the inelasticity $y_{e\Sigma}$ cannot be described by the MC calculations (fig. 3.5 a) and 3.6 b), respectively). The effect of this discrepancy on the detector efficiency and the resulting systematic uncertainty is studied in section 3.9.3.

Except for these all other distributions are described rather well. RAGAP nicely describes the turnover in the $p_t^{D^*}$ spectrum in figure 3.6, which is due to the low detector efficiencies at low transverse momenta shown in section 3.6.

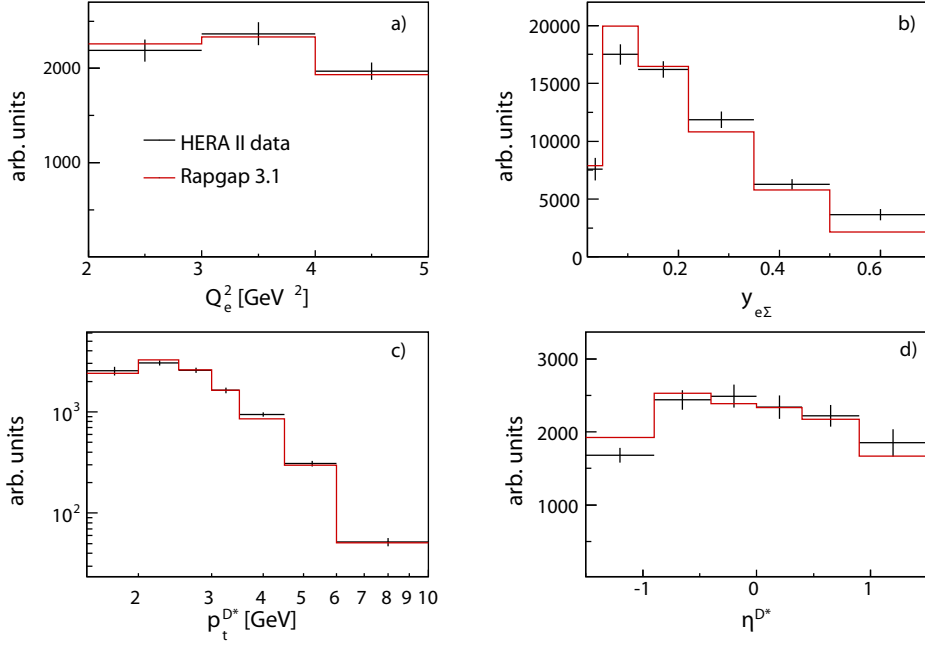


Figure 3.6: Control distributions for the photon virtuality Q_e^2 , the inelasticity $y_{e\Sigma}$, the transverse momentum $p_t^{D^*}$ and the pseudo rapidity η^{D^*} of the D^* meson.

3.3 Triggering D^* mesons in DIS

As will be explained in section 3.5, D^* mesons are reconstructed by studying their decay products which leave tracks in the detector. These tracks provide input for the trigger system to select events in which a D^* meson was produced.

In the H1 trigger system there are 128 subtriggers labeled S0 - S127 which are combinations of individual trigger elements like track conditions or energy thresholds. The sub trigger S61 which was used in this analysis for selecting the decay products of D^* mesons in DIS is a combination of track and electron triggers elements, both of which have to be fulfilled:

$$S61 \doteq \text{Spacial Condition} \wedge \text{Track Condition}.$$

In this section the individual trigger elements are introduced (sec. 3.3.1) and trigger efficiencies are presented (sec. 3.3.2).

trigger element	explanation
SpaCal Condition	
SPCLe_IET>2	$E_{e'} > \sim 9 \text{ GeV}$
SPCLe_IET_Cen_3	triggered in inner part of SpaCal with $E_{e'} > \sim 9 \text{ GeV}$
Track Condition	
DCRPh_THig	≥ 1 track with $p_t^{track} \geq 800 \text{ MeV}$
FTT_mul_Td>0	≥ 1 track with $p_t^{track} \geq 900 \text{ MeV}$

Table 3.2: *Trigger elements of sub trigger S61*

3.3.1 Trigger Elements

In 2004 the track condition of S61 was realized by the trigger element $DCr\phi$. It required at least one track with $p_t > 800 \text{ MeV}$. The track condition changed in 2005 when the Fast Track Trigger (FTT)[27] was installed which triggered on at least one track of $p_t > 900 \text{ MeV}$.

The selection of DIS events was implemented in S61 by requiring an electron in the SpaCal triggered by at least one out of two Inclusive Electron Trigger (IET) elements. This combination of two trigger elements translates into an energy threshold of about 9 GeV for the scattered electron. Table 3.2 lists the trigger elements and their explanation.

3.3.2 Trigger Efficiencies

The efficiency of individual trigger elements is determined with independent more inclusive monitor triggers or trigger elements which are expected to select events in the same kinematic region. Events that are registered by the monitor triggers and at the same time pass the event selection from tables 3.5 and 3.3 serve as a reference sample. The efficiency of the trigger element of interest, ε_{trig} , is then the ratio of events from the reference sample selected by the trigger element ($N^{trig \wedge mon}$) and the total number of events in the reference sample (N^{mon}):

$$\varepsilon_{trig} = \frac{N^{trig \wedge mon}}{N^{mon}} \quad (3.14)$$

For the SpaCal condition of S61, (SPCLe_IET>2 || SPCLe_IET_Cen_3), a large selection of track triggers independent from any SpaCal condition is used for the reference sample. Figure 3.7 shows the efficiency of those trigger elements as a function of the energy of the scattered electron, $E_{e'}$, for all HERA II run periods. This figure

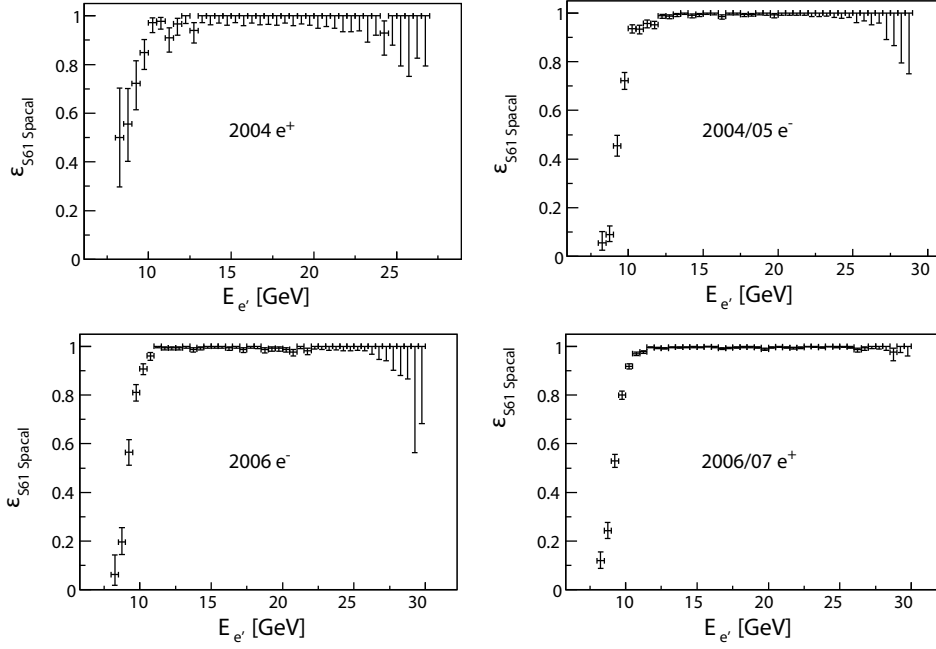


Figure 3.7: Efficiency of the SpaCal trigger elements of S61 for all four HERA II run periods.

shows that scattered electrons with an energy lower than ~ 10 GeV are not triggered efficiently. Therefore only scattered electrons with $E_{e'} > 10$ GeV are accepted.

The efficiency of the track condition in S61 is shown in figure 3.8 as a function of the number of tracks N_{track} , again separately for each run period. In the 2004 positron runs when the DCr ϕ was active a slight inefficiency for a low track multiplicities is visible. The implementation of the FTT improved the efficiency of the track trigger so that even at low track multiplicities the trigger efficiency is close to 100% within the statistical uncertainties.

The total efficiency of the combination of trigger elements in sub trigger S61 is shown in figure 3.9. The data are corrected with these efficiencies in order to derive differential cross sections in the respective observables.

3 D^* Meson Cross Sections

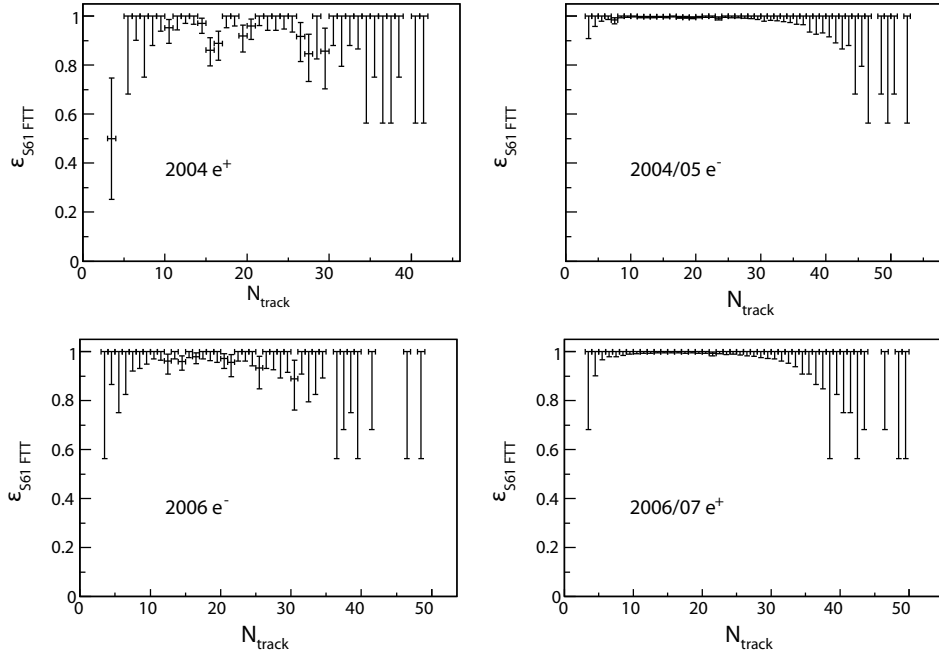


Figure 3.8: *Efficiency of the FTT elements of S61 for all four HERA II run periods.*

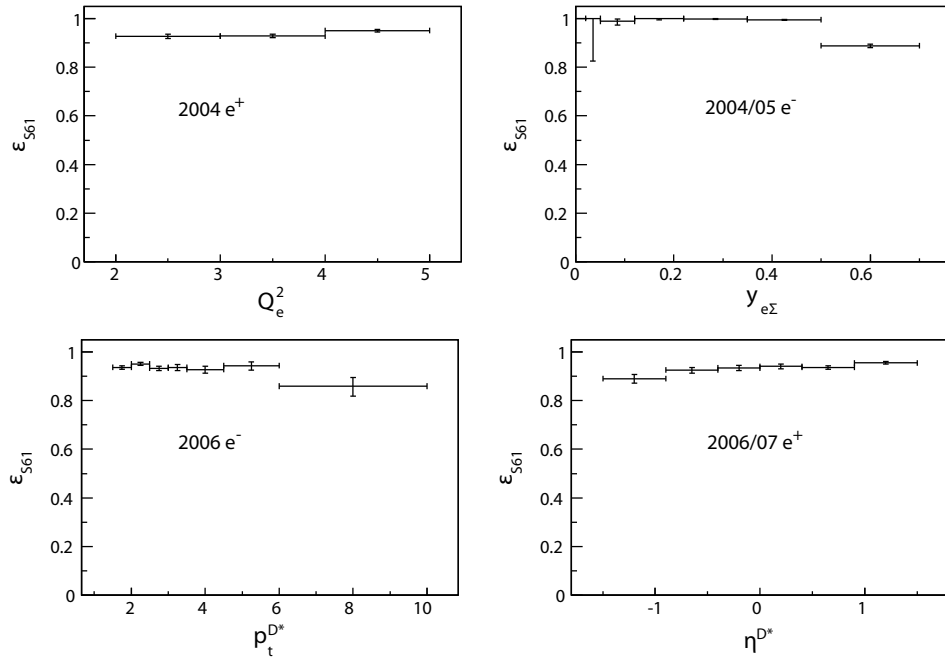


Figure 3.9: *Efficiency of the sub trigger S61 as a function of Q_e^2 , $y_{e\Sigma}$, $p_t^{D^*}$ and η^{D^*} .*

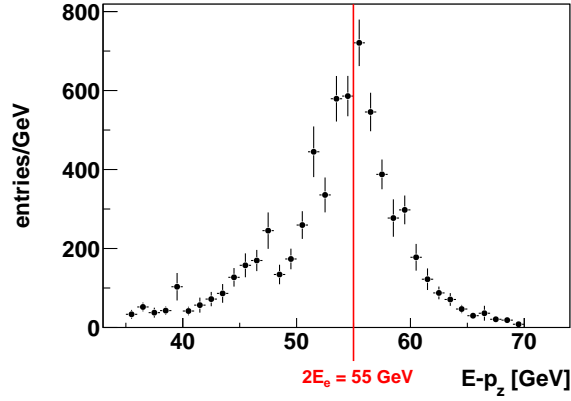


Figure 3.10: *Distribution of the sum of the energy balance, $\sum_i(E_i - p_{z,i})$. The red line indicates the nominal value of $2 \cdot E_e$.*

3.4 Event and D^* Meson Selection Criteria

In this thesis D^* meson production is analyzed in the Q^2 range $2 < Q^2 < 5 \text{ GeV}^2$. The selection criteria for the visible phase space in this range is given in table 3.3. Total and single differential cross sections for the process $ep \rightarrow eD^*X$ are measured, with X being an arbitrary final state configuration.

$$\begin{aligned}
 2 < Q^2 < 5 \text{ GeV}^2 \\
 0.02 < y < 0.7 \\
 p_t^{D^*} > 1.5 \text{ GeV} \\
 |\eta^{D^*}| < 1.5
 \end{aligned}$$

Table 3.3: *Selection criteria for the visible phase space.*

Further selection criteria for ensurance of good event reconstruction quality are given in table 3.4. Events with a measured interaction vertex z_{vertex} outside of $\pm 35 \text{ cm}$ are very rare and badly reconstructed. As known from section 3.2 $\sum_i(E_i - p_{z,i})$ sums the energy balance $E - p_z$ of all particles i in the final state and peaks at $\sum_i(E_i - p_{z,i}) = 2E_e = 55 \text{ GeV}^2$. Events with values of the energy balance outside of the range $35 < \sum_i(E_i - p_{z,i}) < 70 \text{ GeV}$ also are badly reconstructed and are excluded here. Figure 3.10 shows the distribution of $\sum_i(E_i - p_{z,i})$ after the event selection. The red line indicates the nominal value at $2 \cdot E_e = 55 \text{ GeV}$.

The cut on the energy $E_{e'}$ of the scattered electron ensures a high trigger efficiency (see section 2.5).

The reconstruction of D^* mesons needs further requirements on the tracks of its decay particles, as explained in the next section.

3.5 The D^* 's Golden Decay Channel

In this study charm production processes have been tagged with D^* mesons. Since D^* mesons decay via the strong interaction its lifetime is too short for it to leave a track in the detector. Its decay products have to be used to find and reconstruct D^* mesons and their four momenta in ep scattering events.

The $D^{*\pm}$ meson is an excited charmed meson state which always decays into charmed meson ground states, either the neutral D^0 or the charged D^\pm . The decay channel $D^{*\pm} \rightarrow D^0\pi_s^\pm$ dominates over the other two channels $D^{*\pm} \rightarrow D^\pm\pi^0$ and $D^{*\pm} \rightarrow D^\pm\gamma$ with its branching fraction of 67.7%[8]. What is more, the charged slow pion⁶ can leave a track in the detector, unlike the neutral pion and the photon from the alternative decays. This makes it an ideal candidate for the reconstruction of the $D^{*\pm}$.

For the D^0 meson the most prominent decay channel[8] (except for semi-leptonic modes including neutrinos which can't be reconstructed in the detector) is $D^0 \rightarrow K^-\pi^+$ and $\bar{D}^0 \rightarrow K^+\pi^-$ for and its anti-particle. The decay chain $D^{*\pm} \rightarrow D^0\pi_s^\pm \rightarrow K^\mp\pi^\pm\pi_s^\pm$ is therefore the most probable decay to occur in which all decay products leave tracks in the detector – hence the name "golden channel".

Note that the charge of the kaon and the slow pion are opposite. This is due to the fact that a D^{*+} meson decays into a π_s^+ and a D^0 containing a positively charged charm quark. This charm quark then decays into a negatively charged strange quark,

⁶Since the D^0 takes the bulk of the D^* momentum, the pion's momentum is small and it is labeled "slow pion".

Criterion	Purpose
$ z_{vertex} < 35$ cm	Reject badly reconstructed events
$35 < \sum_i(E_i - p_{z,i}) < 70$ GeV	Reject badly reconstructed events
$E_{e'} > 10$ GeV	Ensure high trigger efficiency

Table 3.4: *Quality Ensurance Criteria*. z_{vertex} is the measured position of the interaction vertex, the sum of the energy balance $E - p_z$ runs over all particles i in the final state, and $E_{e'}$ is the energy of the scattered electron.

K^\pm, π^\mp	$p_t > 300 \text{ MeV}$
	$l_{radial}^{track} > 15 \text{ cm}$
	$n_{hits} > 10$
	$p_t^K + p_t^\pi > 2 \text{ GeV}$
	$m(K\pi) - m(D^0) < 80 \text{ MeV}$
π_{slow}^\pm	$p_t > 120 \text{ MeV}$

Table 3.5: *Track requirements for D^* candidates.*

which together with an anti-up quark constitutes a negatively charged kaon.

3.5.1 Reconstructing D^* Mesons from Tracks

The complete final state of the golden decay channel can be reconstructed from tracks in CJC1 and CJC2. In each event three central tracks are required to fulfill the kinematic cuts listed in table 3.5. The D^* -finder algorithm first searches for two tracks that fulfill the conditions for the kaon and the pion (tab. 3.5). One of the two found tracks is then assigned the kaon mass, the other the pion mass. If the mass of the kaon-pion-system, $m(K\pi)$, lies inside a 400 MeV window around the nominal D^0 mass[33] a third track is searched for that passes the requirements for the slow pion from table 3.5. The kaon-pion-pion system is then considered a candidate for a D^* meson.

From all these candidates only those inside a mass window of 80 MeV around the nominal D^0 mass is used for the determination of the number of D^* mesons in the golden channel. Losses due to this narrow mass window are studied using the wide mass window of 400 MeV (see section 3.9.2). Figure 3.11 shows the distribution of the mass of the kaon-pion-system as determined after all selection cuts (tables 3.3, 3.4 and 3.5) except for the narrow D^0 mass window.

The difference of the mass of the D^* candidate and the mass of the D^0 candidate, $\Delta m = |m(K\pi\pi_s) - m(K\pi)|$, is well suited to extract the number of D^* s by a fit (see section 3.5.2) because by taking the mass difference many measuring uncertainties cancel out. The resolution of Δm is then mostly determined by the uncertainties arising from the track measurement of the slow pion.

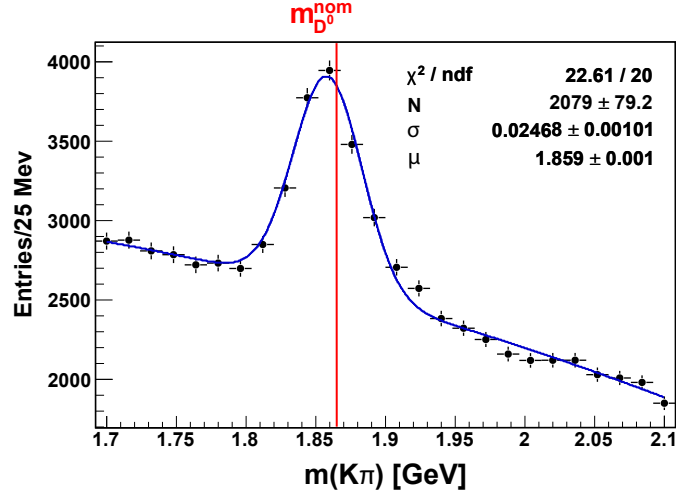


Figure 3.11: *Distribution of $m(K\pi)$ after event and D^* meson selection, but without the restriction $|m(K\pi) - m_{D^0}^{nom}| < 80$ MeV for the kinematic region. A Gaussian distribution fitted to data points is shown in blue. Its normalization N , width σ and offset μ after the fit are displayed together with the χ^2 value for the respective numbers of degrees of freedom (ndf). The red line indicates the nominal value of the D^0 mass at 1.865 GeV [8].*

3.5.2 Signal Extraction

The number of D^* s is determined by fitting the sum of a signal and a background distribution to the measured Δm distribution in the range $135 \text{ MeV} < \Delta m < 170 \text{ MeV}$.

For the signal function the Crystal Ball probability density function[34] is chosen, defined as follows:

$$f_{CB}(\Delta m) = N \cdot \begin{cases} \exp\left(-\frac{1}{2}\left(\frac{\Delta m - \mu}{\sigma}\right)^2\right) & \text{for } \frac{\Delta m - \mu}{\sigma} \geq -\alpha \\ \left(\frac{n}{|\alpha|}\right)^n \exp\left(-\frac{1}{2}\alpha^2\right) & \text{for } \frac{\Delta m - \mu}{\sigma} < -\alpha \\ \left(\frac{n}{|\alpha|} - |\alpha| - \frac{\Delta m - \mu}{\sigma}\right)^n & \end{cases} \quad (3.15)$$

This function resembles a Gaussian distribution with an additional exponential tail which allows for a very flexible adjustment to the peak region. The parameters μ and σ represent the peak position and the width of the peak, respectively, while n and α determine the shape of the exponential tail.

For the background a function by P. Granet et. al.[35] is used:

$$f(\Delta m) = (\Delta m - m_\pi)^{p_1} \cdot \exp(-p_2 \cdot \Delta m - p_3(\Delta m)^2), \quad (3.16)$$

where p_i are the fit parameters while the pion mass m_π is the threshold of the function.

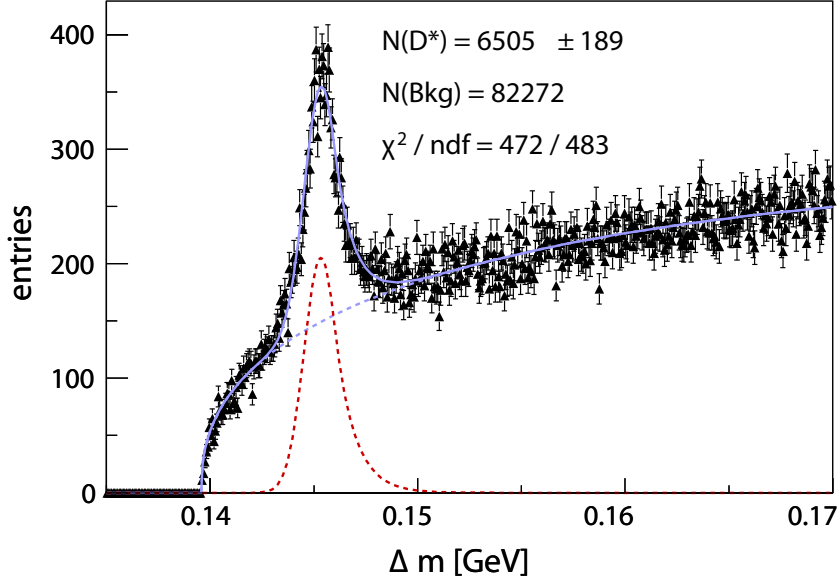


Figure 3.12: *Distribution of Δm for the kinematic region $2 \text{ GeV}^2 < Q^2 < 5 \text{ GeV}^2$. Black triangles are data points. The solid blue line represents the sum of signal and background function, the dashed blue line represents the background and the dashed red line the signal function.*

The fit is performed by the Root based fitting package RooFit [36] using a binned χ^2 fit.

In the method used here the normalization N of the signal function is of no importance, because only the fraction f_{peak} of the events in the signal peak are of interest. This is determined by the ratio of the integral of the signal function f_{sig} to the integral of the sum of signal and background function (f_{bg}):

$$f_{peak} = \frac{\int f_{sig}}{\int (f_{sig} + f_{bg})}.$$

The number of D^* mesons in the Δm peak is then given by

$$N_{D^*} = f_{peak} \cdot N_{hist},$$

where N_{hist} is the total number of entries in the fitted histogram.

In figure 3.12 the final result of the fit for the kinematic region $2 \text{ GeV}^2 < Q^2 < 5 \text{ GeV}^2$ is shown. The complete event selection as presented in section 3.4 has been applied to the data points presented here.

Shown is the number of D^* candidates per 0.07 MeV. Data points are presented

as black dots with statistical uncertainties, the signal function as a dashed red line, the background function as a dashed blue line and the sum of signal and background functions as a solid blue line. The asymmetry of the signal function is clearly visible and described the data very well. Also the fitted background function is in excellent agreement with data points.

The resulting number of D^* mesons from this fit amounts to

$$N_{D^*} = 6505 \pm 189.$$

It is used in the determination of the total visible cross in section 3.10.

3.5.3 Choice of Fit Function

The Crystal Ball function is not the only function with which a good description of the D^* signal can be achieved, nor is the Granet function the only function suited for describing the background. In order to determine a systematic uncertainty for the ambiguity of the fit function the Novosibirsk function[37] is used to determine the total number of D^* mesons for the complete HERA II period. The Novosibirsk function is defined by:

$$f_{N\omega}(\Delta m) = N_{N\omega} \cdot \exp\left(-1/2 \cdot \ln^2(1 + \rho_1 \rho_2 (\Delta m - \mu)) / \rho_2 + \rho_2^2\right) \quad (3.17)$$

The fit parameters are the normalization factor $N_{N\omega}$ and the parameters ρ_1 and ρ_2 .

For the background a polynomial of the form

$$f_{poly}(\Delta m) = N_{poly} \cdot (\Delta m - m_\pi)^{p_1} \cdot (1 - p_2(\Delta m)^2), \quad (3.18)$$

with the normalization factor N_{poly} and the fit parameters p_1 and p_2 is used for the uncertainty determination.

Figure 3.13 shows the results of fits with all four combinations of the two signal and the two background functions. In order to estimate the quality of the the description of the background by the Granet function and the polynomial the so-called *wrong charge* distributions are shown to the right of the Δm distributions. The wrong charge sample is obtained by looking for a track combination of candidates for kaon, pion and slow pion so that the charge of the kaon has the same sign as the charge of the slow pion. Such a track combination cannot stem from the golden channel, since there the charges of kaon and slow pion are opposite. For statistical reasons the

distribution of the wrong charge combinations in Δm , however, is the same as the distribution of the background in the D^* sample. Therefore such a distribution can be used to estimate how well the background function describes the actual background.

The value extracted with the Crystal Ball function for the signal and the Granet function for the background is taken as a reference for determining the systematic uncertainty due to the selection of the fit function. For this the maximum relative difference between combinations of signal and background functions is calculated:

$$\delta_{fit} = \max\left(\frac{N_i - N_{CB \& Gr}}{N_{CB \& Gr}}\right), \quad (3.19)$$

where $N_{CB \& Gr}$ is the number of D^* mesons extracted with the Crystal Ball function for the signal and the Granet function for the background parametrization, and N_i represent all other signal and background function combinations from table 3.6.

The systematic uncertainty then evaluates to $\delta_{fit} = 0.5\%$.

3.5.4 Control Distributions for Track Quantities

In figures 3.14 to 3.19 the control distributions for track quantities are displayed. The uncorrected number of reconstructed D^* mesons obtained from fits to the mass difference spectrum is shown in bins of various observables of the D^* mesons and their decay particles. The MC calculations from RAPGAP are normalized to the data in order to compare the shapes. This comparison provides a crucial test of the detector simulation needed for efficiency determination and bin migration studies (see section 3.6).

Figure 3.14 shows the distribution of the transverse momentum $p_t^{D^*}$, the pseudo rapidity η^{D^*} and the azimuthal angle ϕ^{D^*} of the reconstructed D^* meson. All three distributions show very good agreement between MC predictions and experimental data. The apparent deviations in ϕ^{D^*} seem to be due to statistical fluctuations, so that the overall shape of the ϕ^{D^*} distribution in the RAPGAP is in agreement with the data. The turnover in the $p_t^{D^*}$ spectrum mentioned in section 3.2.4 is also present here.

Figures 3.15, 3.16 and 3.17 show the distributions in transverse momentum p_t , polar angle θ and azimuthal angle ϕ of the decay particles kaon, pion and slow pions used to reconstruct the D^* meson in the golden decay channel. All distributions are

⁷The pseudo rapidity is a measure for the longitudinal Lorentz boost of the D^* meson. It is determined by the polar angle θ^{D^*} : $\eta^{D^*} = -\ln(\tan(\theta^{D^*}/2))$.

3 D^* Meson Cross Sections

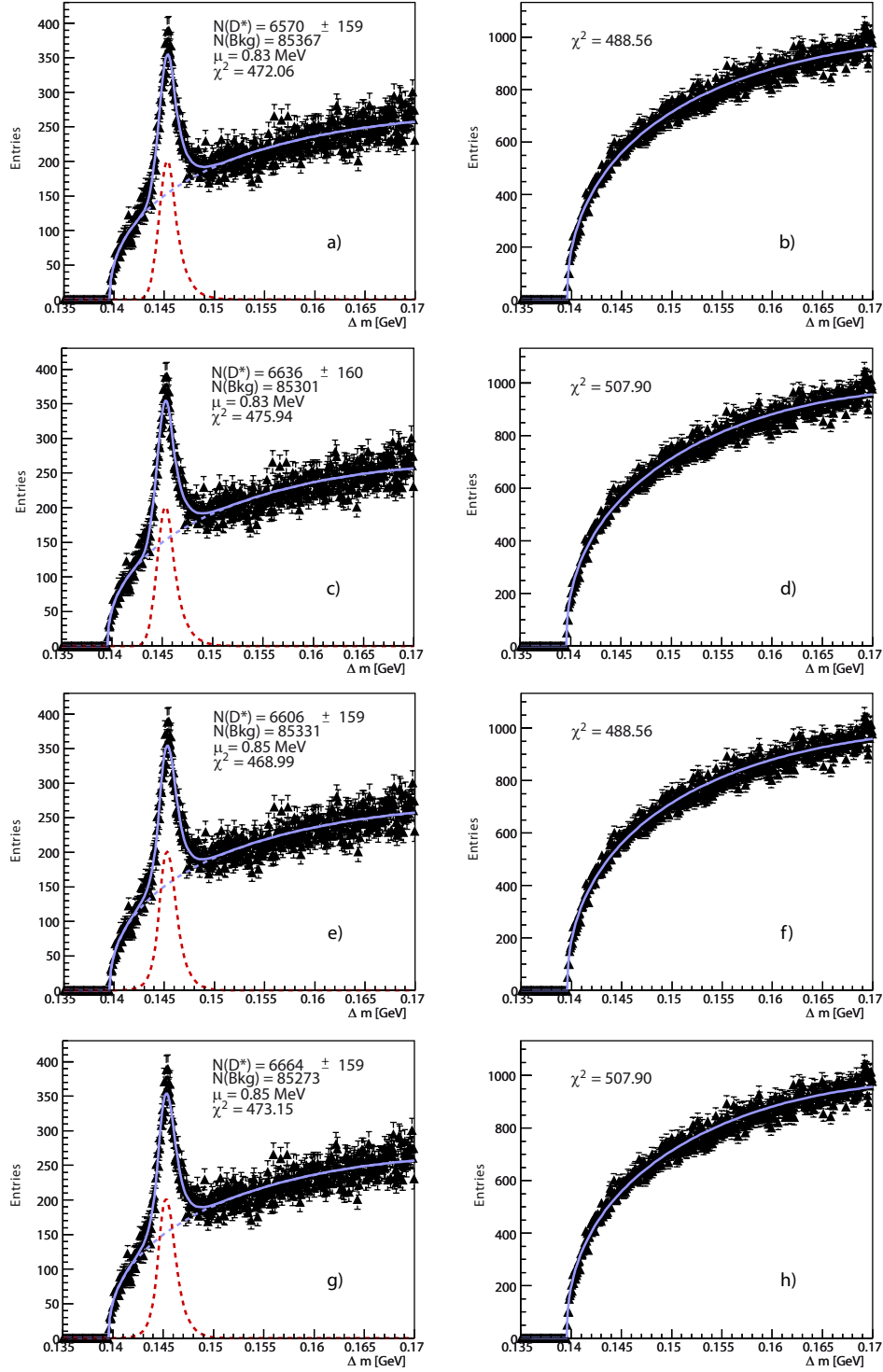


Figure 3.13: *Fit results of different combinations of signal and background functions: a) Crystal Ball signal with Granet background; c) Crystal Ball signal with polynomial background; e) Novosibirsk signal with Granet background; and g) Novosibirsk signal with polynomial background. The quality of the background function is estimated using wrong charge combinations (see text) shown with the Granet function in b) and f) and for the background polynomial in d) and h).*

Signal	&	Background PDF	Results
Crystal Ball	&	Granet	$N(D^*) = 6570 \pm 159$ $\chi^2/\text{ndf} = 472/487 = 0.97$ $\chi_{Bg}^2/\text{ndf} = 489/487 = 1.0$
Crystal Ball	&	polynomial	$N(D^*) = 6636 \pm 160$ $\chi^2/\text{ndf} = 476/487 = 0.98$ $\chi_{Bg}^2/\text{ndf} = 508/487 = 1.04$
Novosibirsk	&	Granet	$N(D^*) = 6606 \pm 159$ $\chi^2/\text{ndf} = 469/486 = 0.96$ $\chi_{Bg}^2/\text{ndf} = 489/487 = 1.0$
Novosibirsk	&	polynomial	$N(D^*) = 6664 \pm 159$ $\chi^2/\text{ndf} = 473/486 = 0.97$ $\chi_{Bg}^2/\text{ndf} = 508/487 = 1.04$

Table 3.6: Comparison of fit quality and results for different combinations of signal and background probability density functions as described in the text.

3 D^* Meson Cross Sections

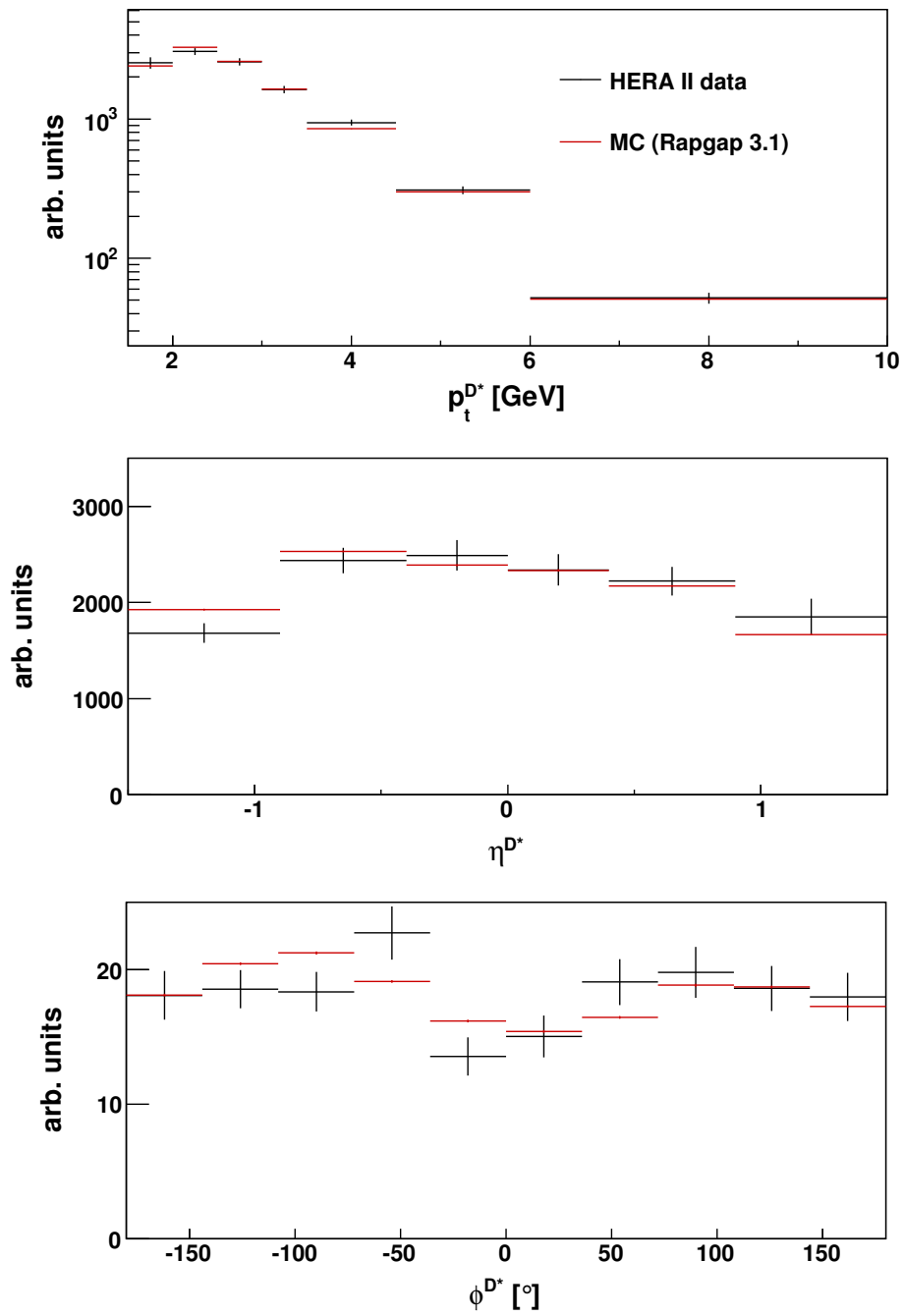


Figure 3.14: *Control Distribution for the D^* meson.*

described well by the RAPGAP calculations.

The distribution of the number of hits in the tracking devices and the track length are shown in figures 3.18 and 3.19 for the three decay products. The double peak signature visible in the hits distributions is due to the fact that not all tracks are reconstructed in both tracking chambers. Except for the second peak being shifted towards slightly lower values in Monte Carlo no significant disagreement between Monte Carlo and data is found in these distributions. As apparent from figure 3.15 these shifts have no significant effect on the reconstruction of the transverse momentum of the tracks.

3 D^* Meson Cross Sections

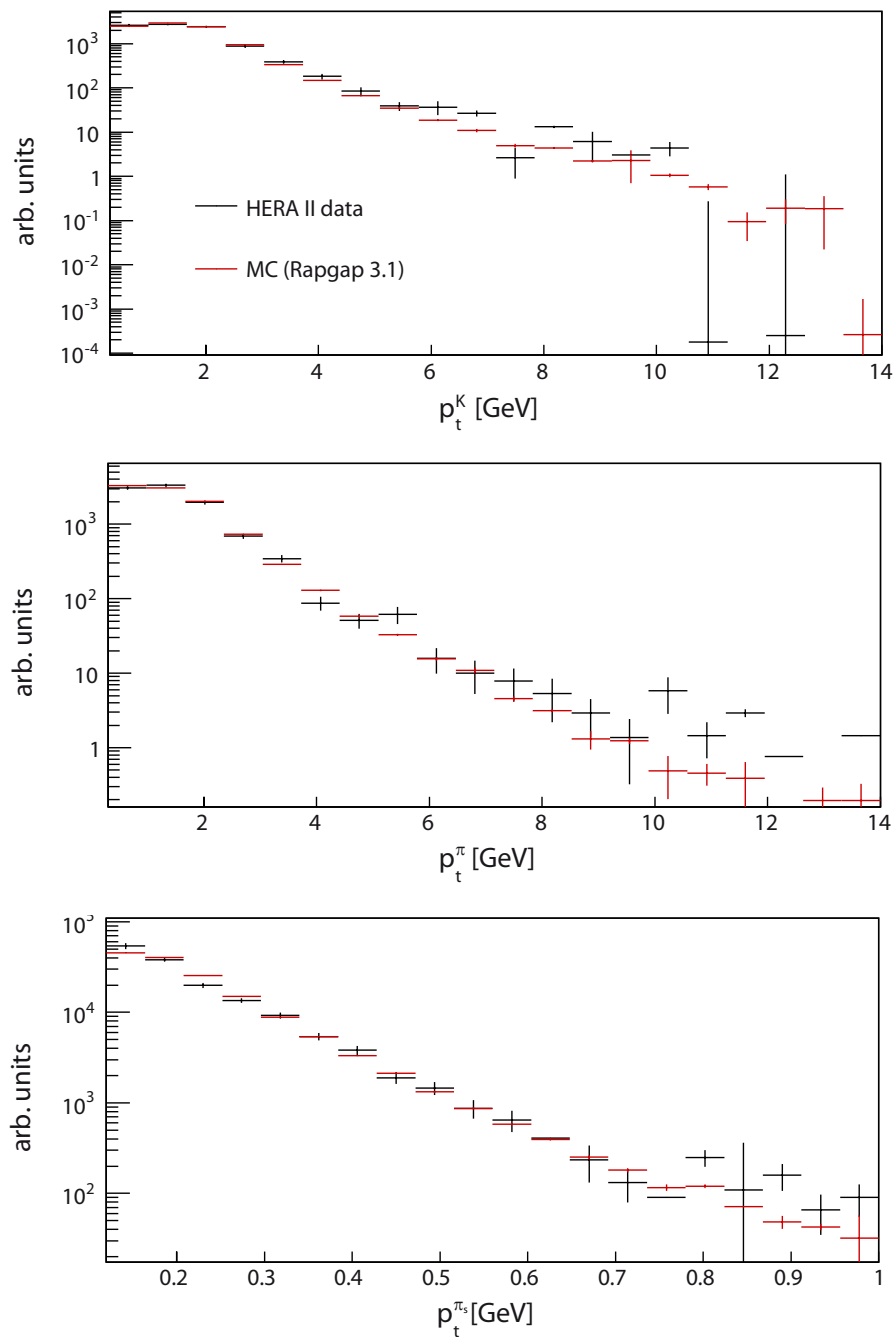


Figure 3.15: *Control Distribution for the transverse momentum of the decay particles kaon, pion and slow pion.*

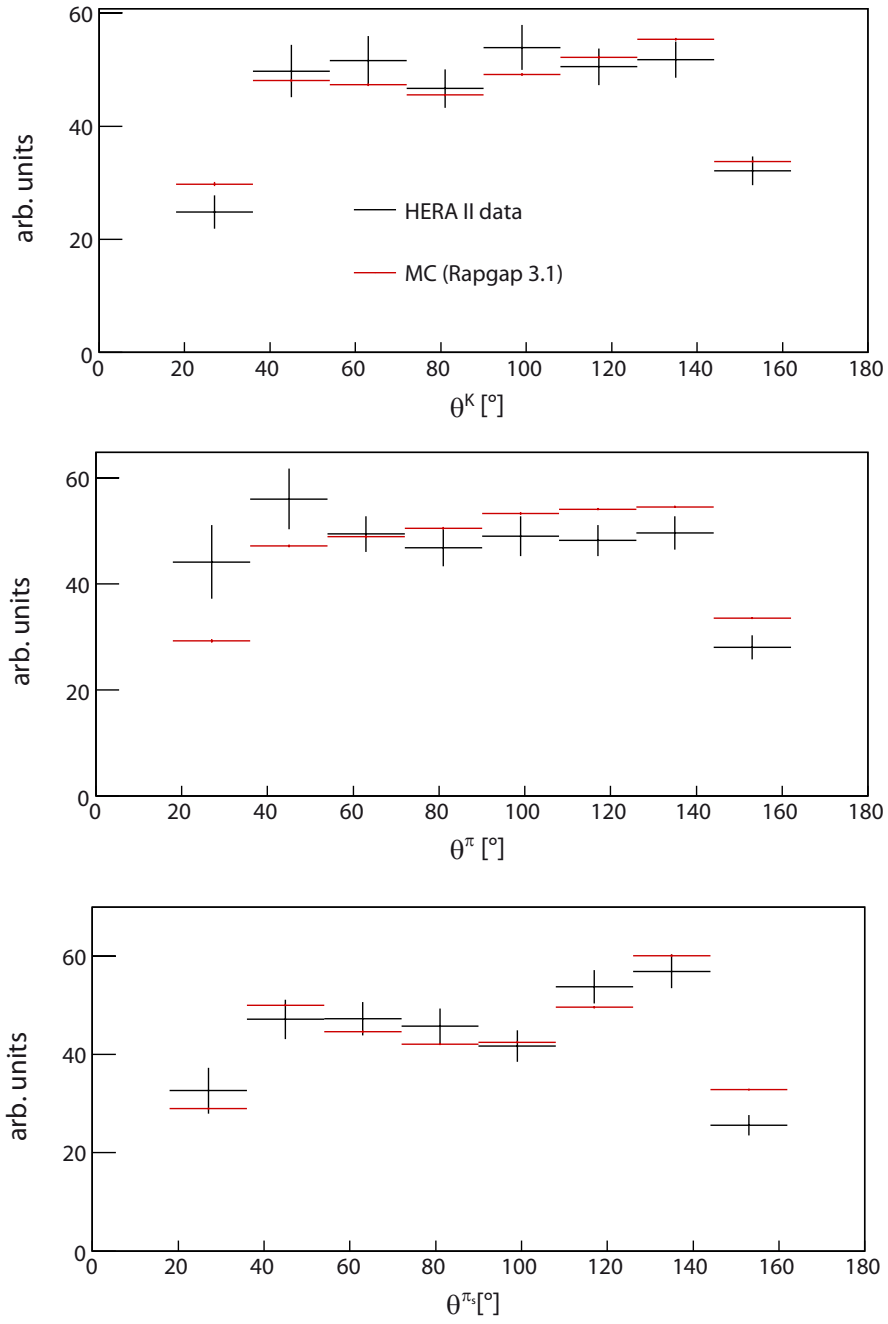


Figure 3.16: *Control Distribution for θ of the decay particles kaon, pion and slow pion.*

3 D^* Meson Cross Sections

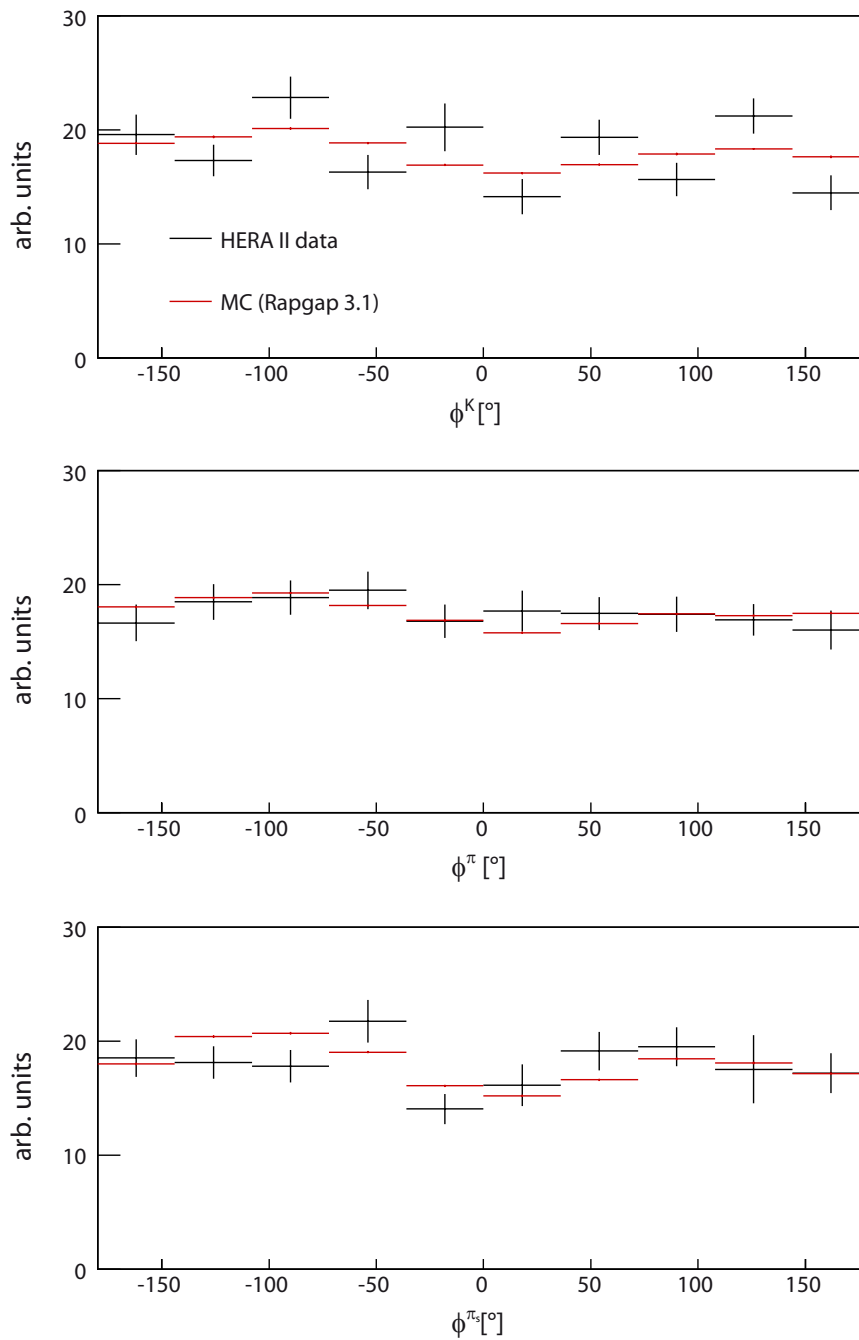


Figure 3.17: *Control Distribution for ϕ of the decay particles kaon, pion and slow pion.*

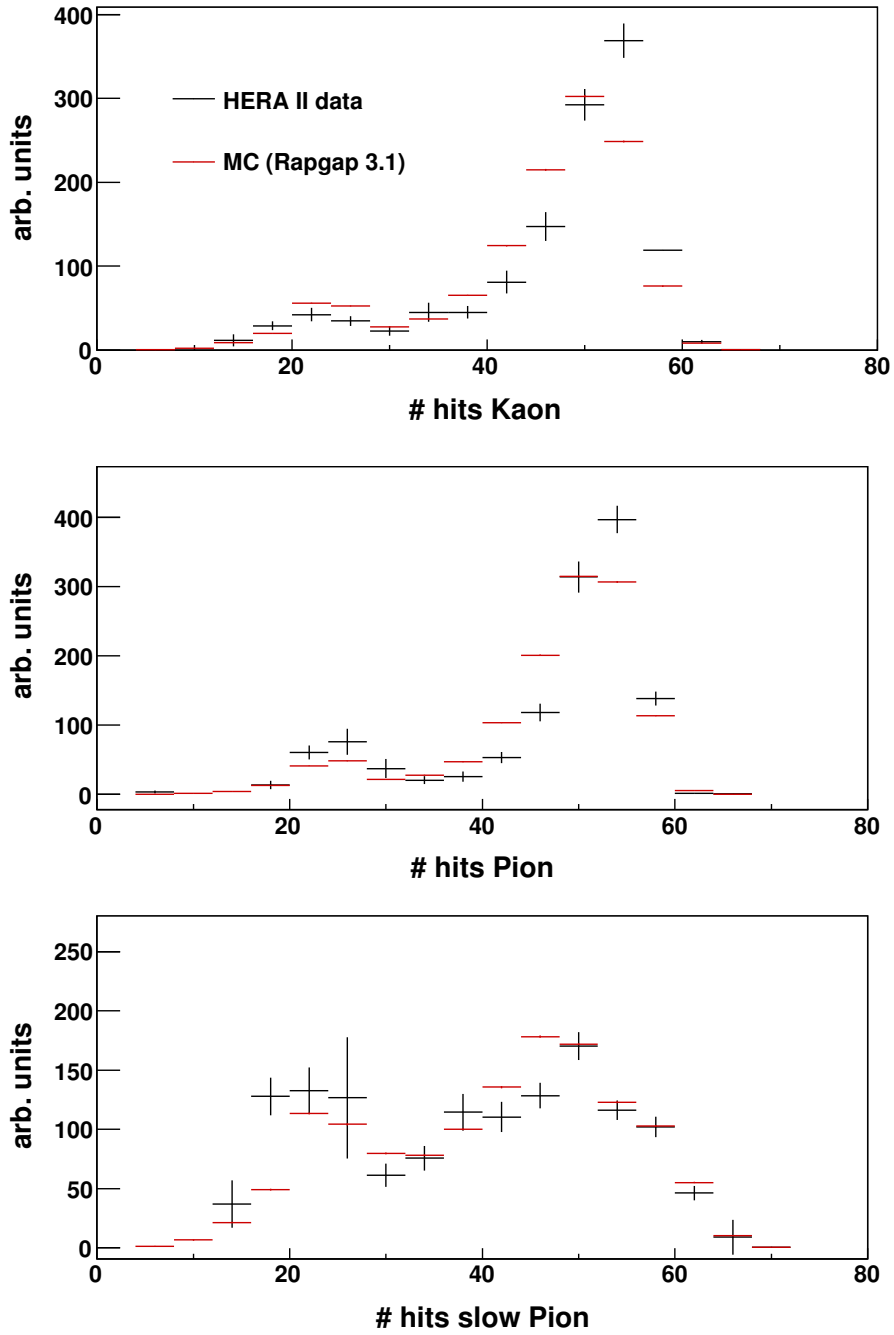


Figure 3.18: Control Distribution for the number of hits of tracks from the decay particles kaon, pion and slow pion.

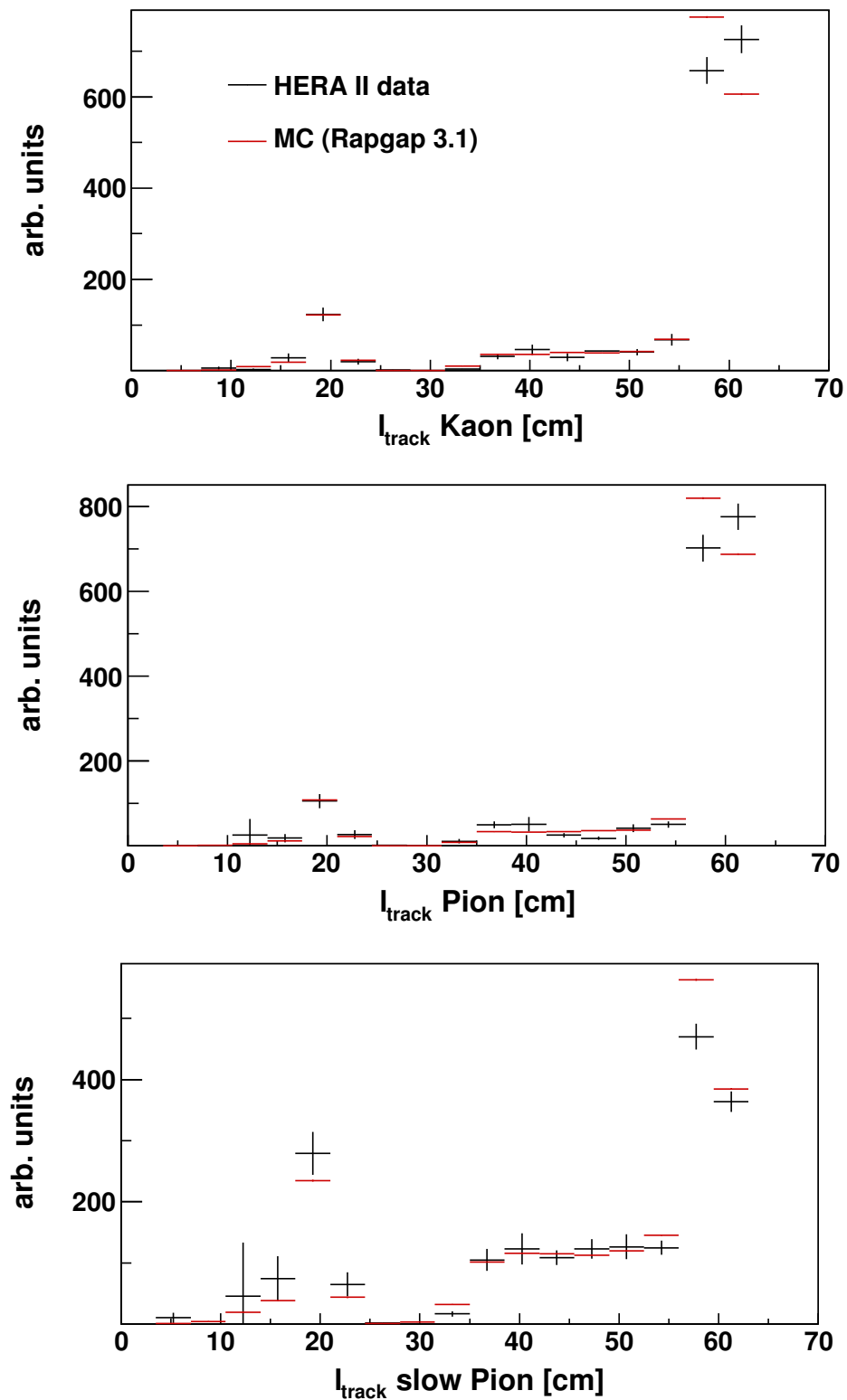


Figure 3.19: Control Distribution for the length of tracks from the decay particles kaon, pion and slow pion.

3.6 Detection Efficiencies and Migration Effects

In measurements of statistical quantities, there are essentially two sources of inefficiencies: detection inefficiencies and migration effects. Detection inefficiency means that not all particles passing through a detector are detected, while migration effects arise from measurement uncertainties.

Because every measurement comes with an uncertainty particles might be measured with a different value of a certain observable than they actually have. For example, if the actual transverse momentum of a D^* meson is $p_{t,ac}^{D^*} = 2.4$ GeV, the measurement might well result in $p_{t,meas}^{D^*} = 2.6$ GeV.

In histograms bins are defined by intervals in observables such as $p_t^{D^*}$ and have well defined boundaries. In the $p_t^{D^*}$ -binning in this analysis one bin is defined as the interval $2.0 < p_t^{D^*} < 2.5$ GeV, so that the D^* meson in the example above would belong to that bin: $2.0 < p_{t,ac}^{D^*} = 2.4 < 2.5$ GeV. The measured value, on the other hand, would be registered in the neighboring bin with $2.5 < p_t^{D^*} < 3.0$ GeV. That means that the particle *migrated* to a different bin than it would be found in if one knew the actual value of, for example, its transverse momentum.

These two phenomena - detection inefficiencies and migration effects - have to be accounted for by a detailed study of the reconstruction method of the detector.

In general one has to apply a proper unfolding method to correct for migrations. This would exploit information about the migrations given by MC simulations for the true value of the measured observable. In addition to the true hadron level⁸ value of an observable one also needs to apply a detector simulation⁹ to the MC predictions to obtain a simulated and reconstructed value of the measured observable. One can then use the correlation matrix – a two dimensional histogram of the true (i. e. generated) value and the reconstructed value of an observable – to unfold the data.

However, if migrations are small compared to detection inefficiencies (meaning considerably less particles are detected in a different bin from the one on hadron level than not being detected at all) it is sufficient to apply a correction factor to each data bin which accounts only for detection loss in that bin. This is called bin-by-bin method.

A measure for the magnitude of migrations into a bin is given by the purity P :

⁸The term *hadron level* refers to final state particles as simulated by MC generators, *parton level* refers to particles before the hadronisation stage, and *detector level* refers to particles as measured by the detector.

⁹See section 2.6.

3 D^* Meson Cross Sections

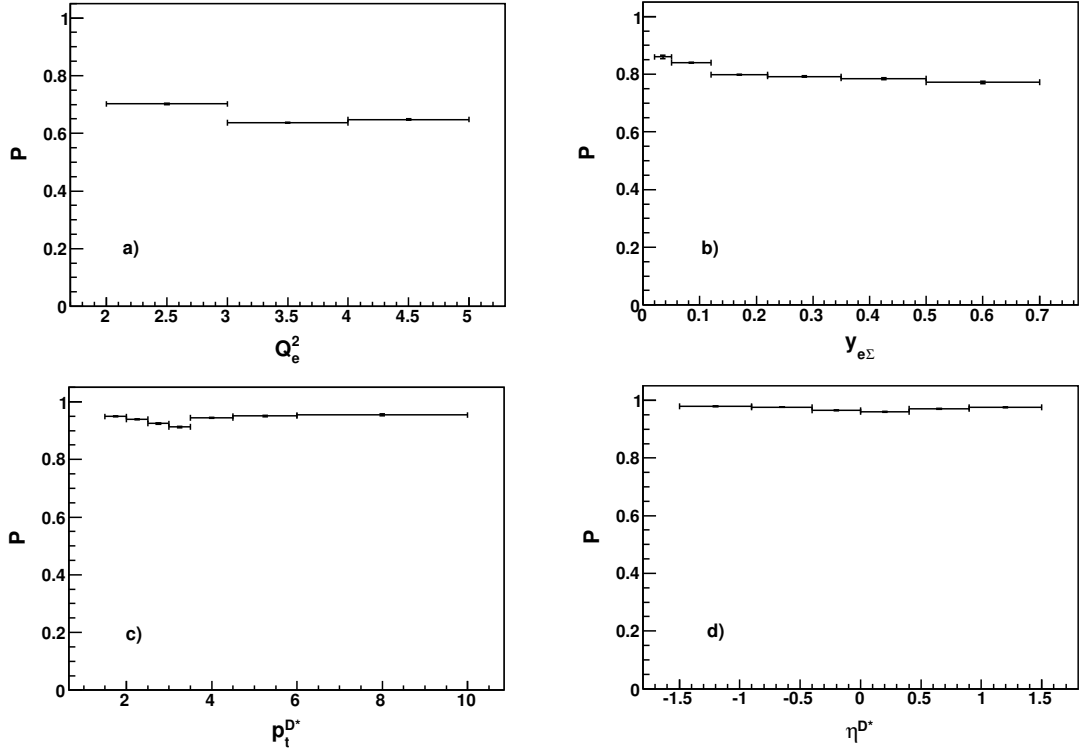


Figure 3.20: *Purity as a function of a) Q_e^2 , b) $y_{e\Sigma}$, c) $p_t^{D^*}$ and d) η^{D^*} as determined with RAPGAP.*

$$P = \frac{N^{rec\wedge gen}}{N^{rec}}, \quad (3.20)$$

where $N^{rec\wedge gen}$ is the number of D^* mesons reconstructed and generated in the same bin and N^{rec} is the number of D^* mesons reconstructed in that bin. Their ratio represents what fraction of D^* s measured in certain a bin also originated there.

In figure 3.20 the purity is shown as a function of a) Q_e^2 , b) $y_{e\Sigma}$, c) $p_t^{D^*}$ and d) η^{D^*} . These distributions show that the purity in all observables for which cross sections are determined are $\gtrsim 70\%$ with no strong dependence on the respective observables. This means that migrations between the individual bins of the observables are small.

The correction factor applied in case of small migrations is defined as the inverse of the detection efficiency ε_{det} in that bin, which is defined as

$$\varepsilon_{det} = \frac{N^{rec}}{N^{gen}}. \quad (3.21)$$

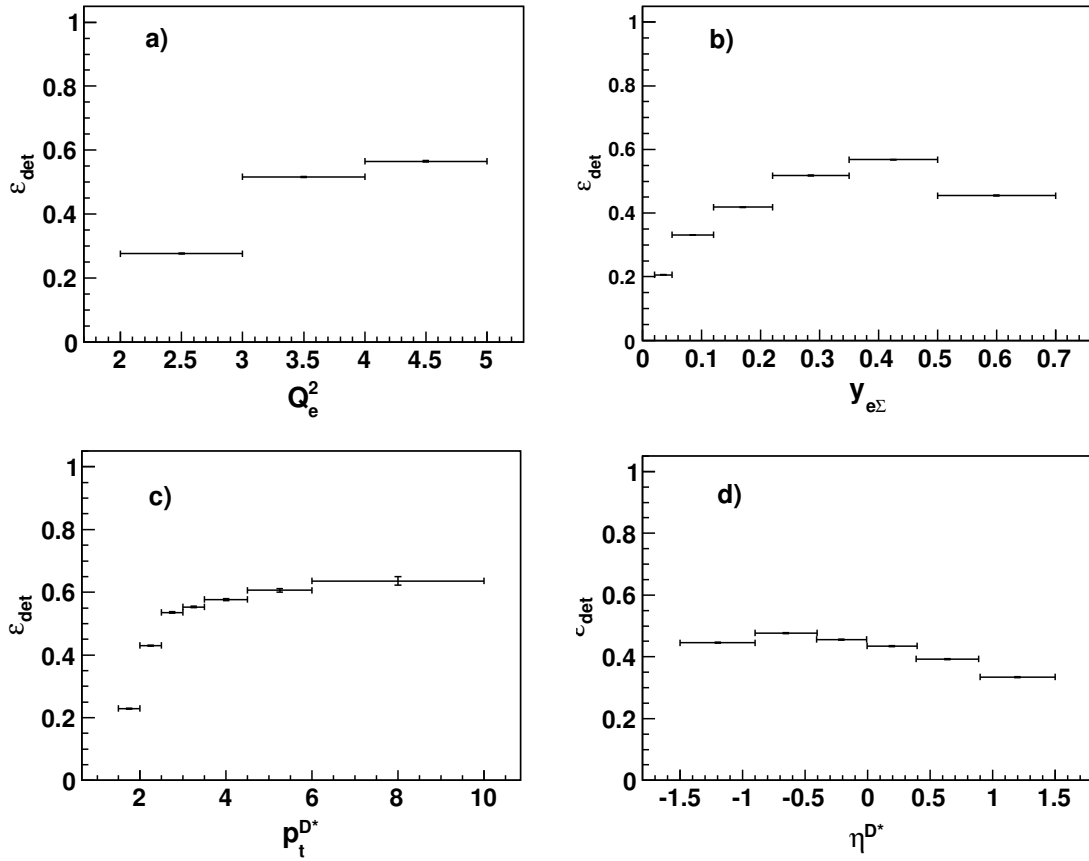


Figure 3.21: *Detection Efficiency ϵ_{det} as a function of a) Q_e^2 , b) $y_{e\Sigma}$, c) p_t^{D*} and d) η^{D*} as determined with RAPGAP.*

The distribution of ε_{det} is shown in figure 3.21, again as a function of a) Q_e^2 , b) $y_{e\Sigma}$, c) $p_t^{D^*}$ and d) η^{D^*} . The detection efficiency as a function of $p_t^{D^*}$ is decreasing strongly towards low values. This leads to a turnover in the pure uncorrected distribution of $p_t^{D^*}$ seen in figures 3.6 and 3.14.

That these efficiencies are small while purities are large shows that the largest part of the particle loss in all bins is due to detector inefficiencies and not from migrations. In this case it is justified to correct the single differential cross sections in the respective observables with $1/\varepsilon_{det}$.

3.7 Contributions from Reflections and Photoproduction

The selection of tracks as candidates for the kaon and the two pions by itself does not ensure a selection of a D^* meson. In addition to the combinatorial background there are also two important contributions to take into account: background from photoproduction events where a signal in the SpaCal has been falsely identified as the scattered electron, and background from other D^* meson decay channels apart from the golden channel, called reflections.

3.7.1 Reflections

A D^* meson can only decay in three possible ways: $D^{*\pm} \rightarrow D^0\pi_s^\pm$, $D^{*\pm} \rightarrow D^\pm\pi^0$ and $D^* \rightarrow D^\pm\gamma$. The track requirements for the slow pion are already strong enough to suppress contributions from the two latter processes, so that only alternative decays of the D^0 meson might give an additional contribution to the Δm -peak.

Table 3.7 lists all D^0 decay channels with at least two charged particles. Together with the slow pion these channels, termed *reflections*, all have at least three charged particles in the final state.

Because for cross section determination the number of D^* mesons is corrected with the branching ratio of the golden channel, the contribution from these reflections have to be subtracted from the fitted number of D^* mesons in the golden channel. This contribution has been determined by the Monte Carlo generator RAPGAP.

In the search for the golden decay channel of D^* mesons the tracks of these decay products will be assigned either the mass of a kaon or a pion. After that the resulting kinematics have to fulfill the track requirements mentioned in section 3.5.1 in order

3.7 Contributions from Reflections and Photoproduction

Decay channel	Branching ratio
$D^0 \rightarrow K^\pm K^\mp$	$(3.84 \pm 0.1) \cdot 10^{-3}$
$D^0 \rightarrow K^\mp \pi^\pm \pi^0$	$(14.1 \pm 0.5) \cdot 10^{-2}$
$D^0 \rightarrow \pi^\pm \pi^\mp$	$(1.36 \pm 0.03) \cdot 10^{-3}$
$D^0 \rightarrow \pi^\pm \pi^\mp \pi^\pm \pi^\mp$	$(7.31 \pm 0.27) \cdot 10^{-3}$
$D^0 \rightarrow \pi^\pm \pi^\mp \pi^0$	$(1.31 \pm 0.06) \cdot 10^{-2}$
$D^0 \rightarrow K^\pm e^\mp \nu_e^{(-)}$	$(3.51 \pm 0.11) \cdot 10^{-2}$
$D^0 \rightarrow K^\pm \mu^\mp \nu_\mu^{(-)}$	$(3.19 \pm 0.16) \cdot 10^{-2}$
$D^0 \rightarrow \pi^\pm e^\mp \nu_e^{(-)}$	$(2.81 \pm 0.19) \cdot 10^{-3}$
$D^0 \rightarrow \pi^\pm \mu^\mp \nu_\mu^{(-)}$	$(2.4 \pm 0.4) \cdot 10^{-3}$

Table 3.7: Alternative D^0 decay channels contribution to the Δm peak.

to be identified as a D^* . In the rare case when this happens for tracks of decay products from reflections the mass difference $\Delta m = m_{D^*} - m_{D^0}$ – calculated under the assumption that the golden channel has been found – only shows deviation from the nominal Δm value too small to be measured and therefore also form a peak in the distribution.

If identified correctly the invariant mass of the two charged daughters of the alternative D^0 decays of table 3.7 does not peak at the nominal D^0 mass but at lower values. In this case the D^0 mass window rejects these particles. It is only because of wrong mass assignments that these particles are “reflected” from their actual mass peak into the D^0 mass window, which is how these D^* candidates have gotten their name.

The fraction of reflections in the Δm peak is given by,

$$\mathcal{R} = \frac{N_{refl}}{N_{refl} + N_{gc}},$$

N_{refl} being the number of D^* meson candidates from reflections (figure 3.22, left) and N_{gc} the number of D^* meson candidates from the golden channel (figure 3.22, right). \mathcal{R} is determined from a dedicated RAPGAP sample for D^* mesons decaying in the golden channel and additionally allowing for the reflections of table 3.7. The full event selection and reconstruction cycle was applied to the RAPGAP sample. The relative contribution from reflections amounts to

$$\mathcal{R} = (4.6 \pm 0.018)\%.$$

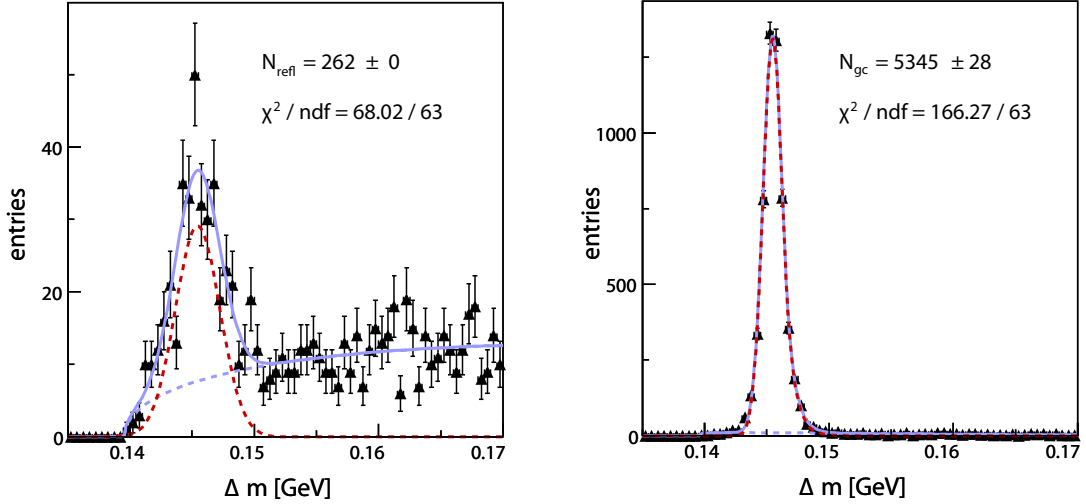


Figure 3.22: Contributions from reflections (left plot) to the golden channel (right plot) as determined by a fit to RAPGAP predictions (black triangles). The blue solid line represents the sum of the signal and background functions, the blue dashed line the background and the red dashed line the signal function.

3.7.2 Photoproduction Background

In photoproduction (γp) events, where $Q^2 \sim 0$, the incoming electron is scattered under such a large angle $\theta_{e'}$ that it escapes detection by the backward calorimeter SpaCal. In such an event it can still occur that a signal in the SpaCal is falsely identified as the scattered electron. These events then form a background to the cross section measurement which has to be determined from a MC generator.

For this purpose a D^* MC sample was generated with $Q^2 = 0$ GeV with the MC generator RAPGAP. After the detector simulation was applied the sample has been analyzed with exactly the same procedure as the data. The resulting *false γp cross section*¹⁰ $\sigma_{\gamma p}^{sel} = N_{\gamma p}^{sel}(D^*) / \mathcal{L}_{\gamma p}$ has been determined, where $\mathcal{L}_{\gamma p}$ is the luminosity of the photoproduction MC sample and $N_{\gamma p}^{sel}(D^*)$ is the number of D^* mesons determined from the γp -sample after applying all DIS selection cuts. It represents the probability that D^* mesons in photoproduction events are falsely identified as DIS events in the analyzed visible phase space.

The contribution from photoproduction events \mathcal{P} to be subtracted from the data

¹⁰“False” because strictly speaking it is only the number of D^* mesons per luminosity in events falsely identified DIS events and not a cross section of a physical process.

is then determined by :

$$\mathcal{P} = \frac{\sigma_{\gamma p}^{sel}}{\sigma_{\gamma p}^{sel} + \sigma_{DIS}} . \quad (3.22)$$

Here σ_{DIS} is the total D^* meson cross section in the visible phase space determined from the DIS Monte Carlo sample which is used for the determination of detector efficiencies and various systematic uncertainties.

With a total D^* meson cross section in DIS of $\sigma_{DIS} = (1.327 \pm 0.007)$ nb and a false γp cross section of $\sigma_{\gamma p}^{sel} = (0.01255 \pm 0.00005)$ nb the photoproduction contribution amounts to

$$\mathcal{P} = (0.937 \pm 0.002)\% .$$

3.8 Radiative Corrections

The electron can radiate photons both before and after the interaction with the proton. The Monte Carlo sample used to determine the detector efficiencies includes this additional QED radiation. In the cross section determination the number of D^* mesons is corrected for this effect by a comparison of two Monte Carlo samples, one including QED radiation (labeled *rad*) and one without (labeled *non-rad*). The correction factor $c_{rad} = N^{non-rad}/N^{rad}$ is the ratio of the number of D^* mesons determined without QED radiation, $N^{non-rad}$, and with QED radiation, N^{rad} .

Figure 3.23 shows the distribution of c_{rad} as a function of Q^2 (a), y (b), $p_t^{D^*}$ (c) and η^{D^*} (d). Since the distributions in 3.23a), c) and d) are flat a single global value for c_{rad} can be applied to correct the respective differential cross sections. A fit of single parameter $p0$ has been performed to determine the correction factor. It is nicely visible that all fits in Q^2 , $p_t^{D^*}$ and η^{D^*} yield the same result

$$c_{rad} = 1.033 \pm 0.001 \quad (3.23)$$

The inelasticity y is more sensitive to QED radiation, which can be seen in figure 3.23. This is why the histogram of $N^{D^*}(y_{e\Sigma})$ is multiplied with histogram of $c_{rad}(y)$ shown in figure 3.23 b) to correct for QED radiation in the determination of the differential cross section $d\sigma(ep \rightarrow D^*X)/dy$.

3 D^* Meson Cross Sections

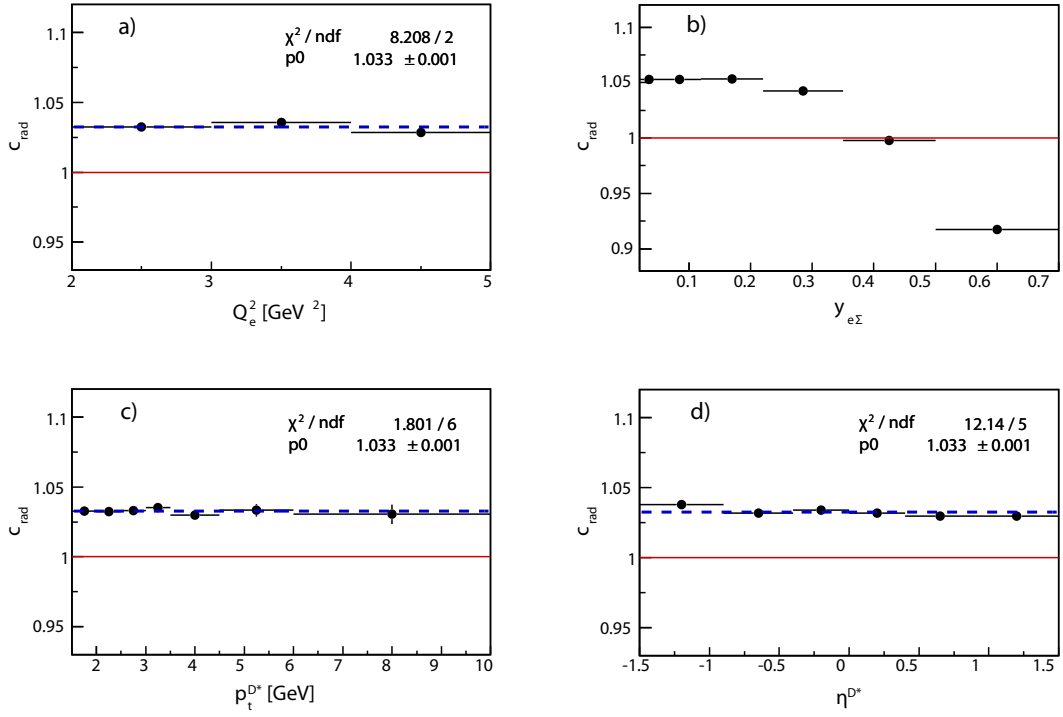


Figure 3.23: The correction factor c_{rad} as a function of a) Q^2 , b) y , c) $p_t^{D^*}$ and d) η^{D^*} as determined by RAPGAP. The blue dashed lines in a), c) and d) show the result of fit of a single parameter $p0$ assuming the distributions to be flat.

Source of Uncertainty	Variation	Uncertainty
Luminosity [1]		3.2%
Branching Ratio [33]		2.3%
Primary Vertex Fit Efficiency [38]		2.5%
Radiative Corrections		0.1%
Signal Extraction		0.5%
Track Finding[38]		6% (2%/track)
Em. Energy Scale ¹¹	$\pm 3\%/0.5\%$	+1.1% -0.8%
Had. Energy Scale	$\pm 4\%$	< 0.1%
D^0 mass window		1%
Reweighting		+0.4% -4.7%
Detector Efficiency		0.1%
Trigger Efficiency		0.4%
Total Uncertainty		+7.8% -9.1%

Table 3.8: *Systematic Uncertainties: Listed are the source, the uncertainty on the source and the resulting uncertainty on the cross section.*

3.9 Systematic Uncertainties

Due to the largely increased luminosity during the HERA II period systematic uncertainties dominate over statistical uncertainties. This chapter gives an overview of the systematic uncertainties considered in this analysis.

Table 3.8 lists all the sources and values of the applied systematic uncertainties. In those cases where no reference is given in the table the determination is presented in detail below.

3.9.1 Uncertainty of Energy Measurements

To determine the effect of the uncertainty of the energy scale on the cross section the electromagnetic (em.) and hadronic (had.) energy scales have been varied up or down in the MC simulation by the respective uncertainties, δ_{em} and δ_{had} (for the values of these uncertainties see below). The relative uncertainty on the number of reconstructed D^* meson candidates has been determined using

$$\delta_{rel} = \frac{N - N^{\uparrow\downarrow}}{N}.$$

Here, $N^{\uparrow\downarrow}$ denotes the number of reconstructed D^* candidates after the energy scale has been varied up or down by $\delta_{em.}$ or $\delta_{had.}$, and N denotes the number of reconstructed D^* candidates without any variation of the energy scale. This uncertainty, δ_{rel} , has been determined as a function of Q_e^2 , $y_{e\Sigma}$, $p_t^{D^*}$ and η^{D^*} .

As shown in section 3.2.3 the uncertainty of the em. energy scale is larger at low radii in the SpaCal. Therefore the following relative uncertainties have been used for the variation of the energy scale:

$$\delta_{em.} = \begin{cases} 3\% & \text{for } r_{SpaCal} < 15 \text{ cm} \\ 0.5\% & \text{for } r_{SpaCal} > 15 \text{ cm} \end{cases}$$

The results are displayed in figure 3.9.1. The number of D^* mesons N^\uparrow (N^\downarrow) after varying the electromagnetic energy scale up (down) is represented by solid red lines (blue dashed lines).

The relative uncertainty due to the hadronic energy scale has been determined in the same fashion with systematic variations of $\delta_{had} = 4\%$. The two lower plots in figure 3.9.1 show the results. Again, the solid red lines (blue dashed lines) represents the number of D^* mesons N^\uparrow (N^\downarrow) after varying the electromagnetic energy scale up (down).

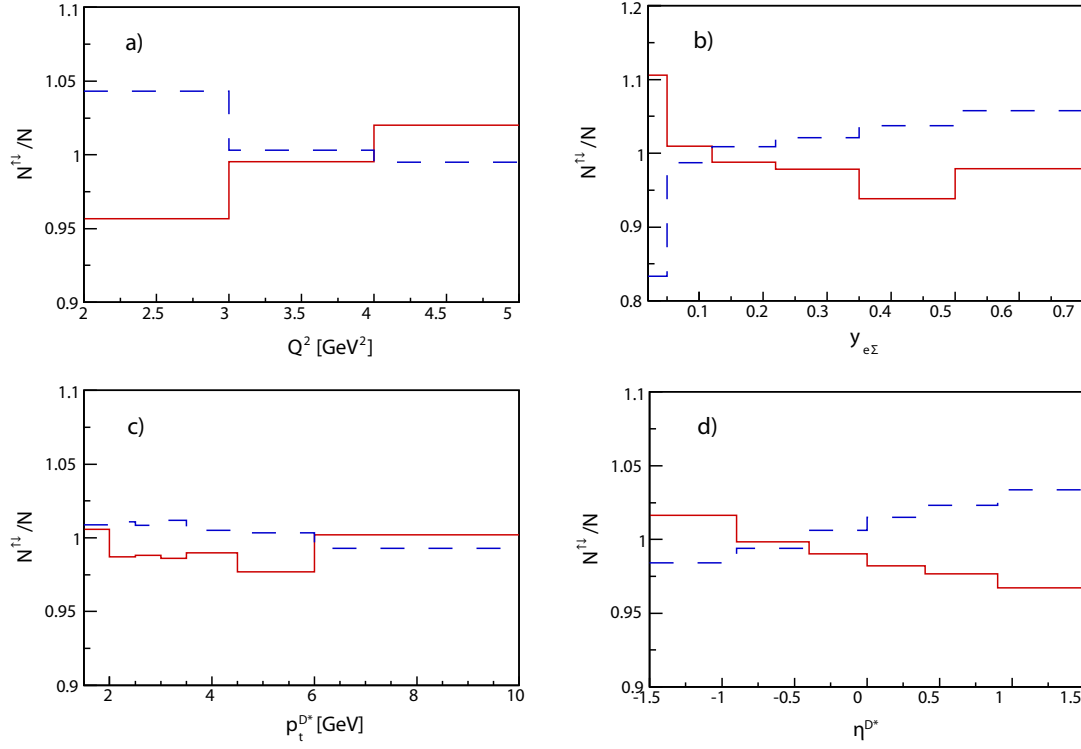


Figure 3.24: Ratio $N^{\uparrow\downarrow}/N$ resulting from variation of the electromagnetic energy scale as a functions of a) Q_e^2 , b) $y_{e\Sigma}$, c) $p_t^{D^*}$ and d) η^{D^*} as determined with RAPGAP. The number of D^* mesons N^\uparrow (N^\downarrow) after varying the electromagnetic energy scale up (down) is represented by solid red lines (blue dashed lines).

3 D^* Meson Cross Sections

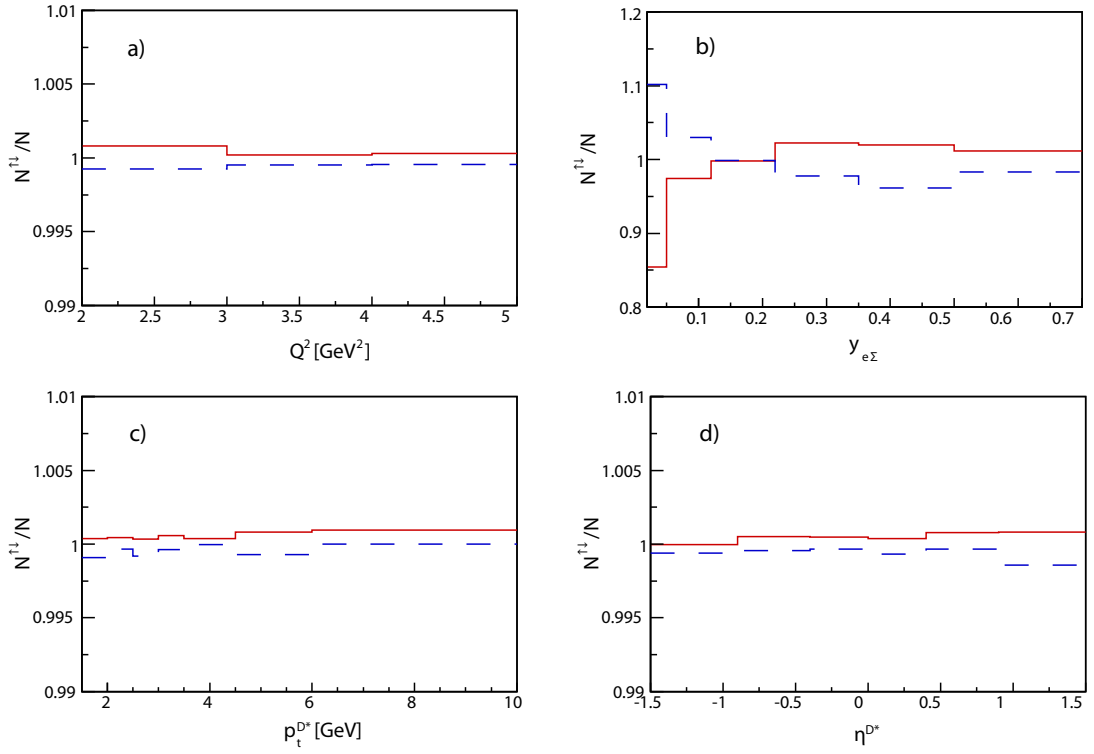


Figure 3.25: Ratio $N^{\uparrow\downarrow}/N$ resulting from variation of the hadronic energy scale as a functions of a) Q_e^2 , b) $y_{e\Sigma}$, c) $p_t^{D^*}$ and d) η^{D^*} a determined with RAP-GAP. The number of D^* mesons N^\uparrow (N^\downarrow) after varying the hadronic energy scale up (down) is represented by solid red lines (blue dashed lines).

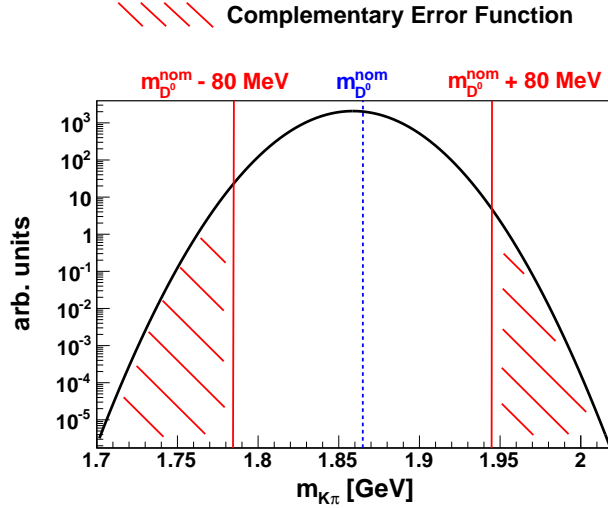


Figure 3.26: An example of how the loss due to the narrow D^0 mass window is calculated: After a Gaussian distribution (here taken from a fit to the distribution of $m(K\pi)$ from figure 3.11) has been fitted to a $m(K\pi)$ distribution the complementary error function erfc (see text) gives the integral of the Gaussian distribution outside the D^0 mass window $m_{D^0}^{\text{nom}} \pm 80 \text{ MeV}$ (red lines). The nominal D^0 mass $m_{D^0}^{\text{nom}} = 1.865 \text{ GeV}$ [8] is indicated as a blue dashed line.

3.9.2 Losses From The D^0 Mass Window

The Selection of kaon and pion candidates inside a window of 80 MeV around the nominal D^0 mass, $|m(K\pi) - m(D^0)| < 80 \text{ MeV}$ with $m(D^0) = 1.864 \text{ GeV}$ [8], excludes a certain amount of D^* mesons. This loss is estimated by fitting a normal distribution to the mass peak in the $m(K\pi)$ spectrum and a line to the background in bins of the transverse momentum of the D^* candidate.

Figure 3.27 shows the resulting values and uncertainties for $m(K\pi)$ as a function of $p_t^{D^*}$ (left). The fraction f_{loss} of D^* mesons lost to the D^0 mass cut is estimated with the complementary of the Gaussian error function:

$$f_{\text{loss}} = \text{erfc} \left(\frac{m_{\text{cut}}}{\sqrt{2}\sigma_{m_{K\pi}}} \right) = \frac{2}{\sqrt{\pi}} \int_{m_{\text{cut}}/\sqrt{2}\sigma_{m_{K\pi}}}^{\infty} e^{-t^2} dt.$$

This function gives the integral of a Gaussian distribution with width $\sigma_{m_{K\pi}}$ outside the boundary $\pm m_{\text{cut}} = 80 \text{ MeV}$, which amounts to the relative loss f_{loss} of D^* mesons. An example of the calculation of f_{loss} with the complementary error function is shown in figure 3.26.

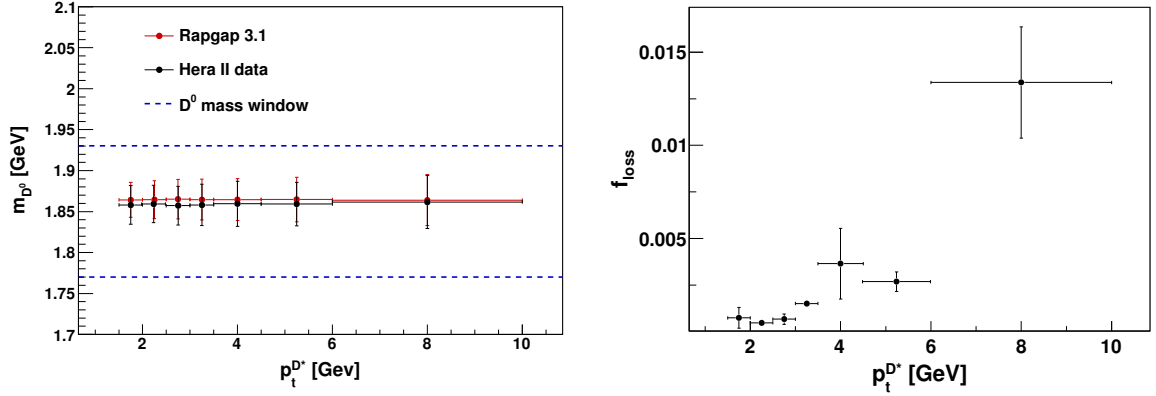


Figure 3.27: On the left: Invariant mass of the decay products kaon and pion as a function of $p_t^{D^*}$. Central values and uncertainties are taken from fits of a normal distribution to data (black) and MC (red). The D^0 mass window is shown as blue dashed lines. On the right: loss due to the D^0 mass window as a function of $p_t^{D^*}$.

Figure 3.27 on the right shows the distribution of f_{loss} as a function of $p_t^{D^*}$. Except for the largest $p_t^{D^*}$ bin the loss is always lower than 1%, and even in that bin the uncertainty – estimated by comparing the loss in data and MC with $\sigma_{loss} = (f_{loss}^{data} - f_{loss}^{MC})/f_{loss}^{data}$ – is large enough to be compatible with a one percent loss. To account for this a systematic uncertainty of 1% is assigned to the number of D^* mesons.

3.9.3 Reweighting Uncertainty

Due to the discrepancy of MC calculations and experimental data described in section 3.2.4 the MC sample has been reweighted in the energy $E_{e'}$ of the scattered electron and the inelasticity $y_{e\Sigma}$. The results of the reweighting are shown in figures 3.28 and 3.29. Experimental data is shown as black dots, the unweighted MC sample as red dashed lines, the MC sample reweighted in $E_{e'}$ as blue open diamonds and the MC sample reweighted in $y_{e\Sigma}$ as red open squares.

The sample reweighted in $y_{e\Sigma}$ still cannot describe the energy spectrum of the scattered electron (fig. 3.28), and the sample reweighted in $E_{e'}$ still shows a discrepancy in $y_{e\Sigma}$ (fig. 3.29).

The effect of these discrepancies on the detector efficiency ε_{det} has been studied and is shown in figure 3.30. The strongest difference is seen in the distribution of $y_{e\Sigma}$. The largest difference between unweighted and reweighted samples is seen at high $y_{e\Sigma}$, where the detector efficiency determined by the sample reweighted in $E_{e'}$

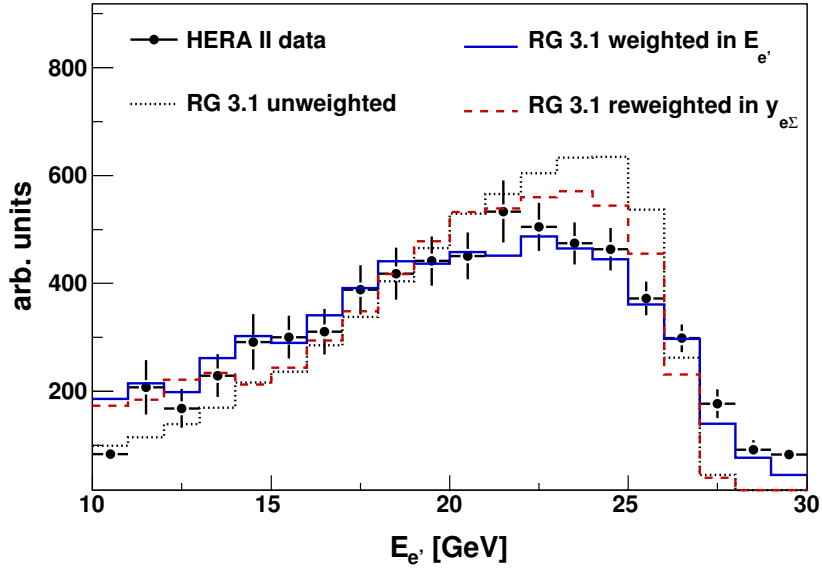


Figure 3.28: Comparison of the MC predictions and experimental data for the scattered electron energy $E_{e'}$. The MC sample is shown after reweighting in $E_{e'}$ (blue) and $y_{e\Sigma}$ (red dashed) as well as without weights (black dotted).

deviates by about 10% from the unweighted one.

From these results a systematic reweighting uncertainty σ_{rew} is determined. It is defined by

$$\sigma_{rew} = 1 - \frac{\varepsilon_{det}^{rew}}{\varepsilon_{det}}, \quad (3.24)$$

where ε_{det} is the detector efficiency of the unweighted sample and ε_{det}^{rew} the one of the reweighted sample with the maximal deviation from the unweighted sample.

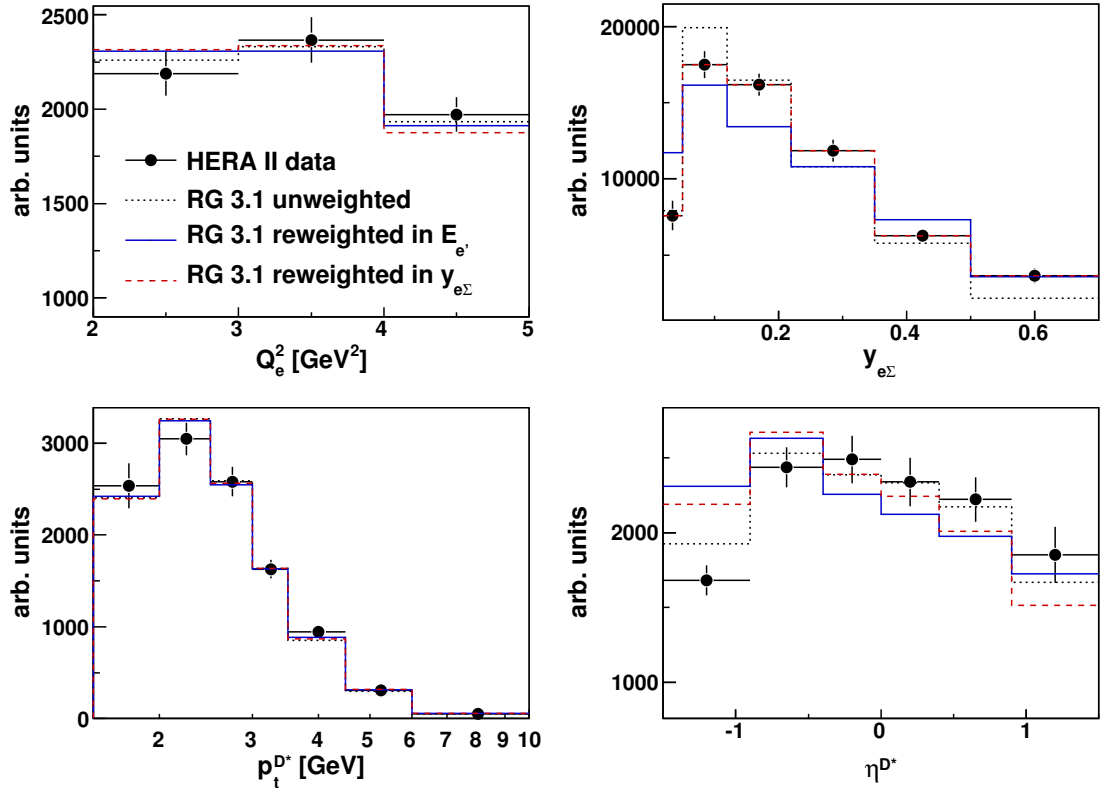


Figure 3.29: Comparison of the MC predictions and experimental data for the photon virtuality Q_e^2 , the inelasticity $y_{e\Sigma}$, the transverse momentum $p_t^{D^*}$ and the pseudo rapidity η^{D^*} of the D^* meson. The MC sample is shown after reweighting in $E_{e'}$ (solid blue line) and $y_{e\Sigma}$ (dashed red line) as well as without weights (black dash-dotted).

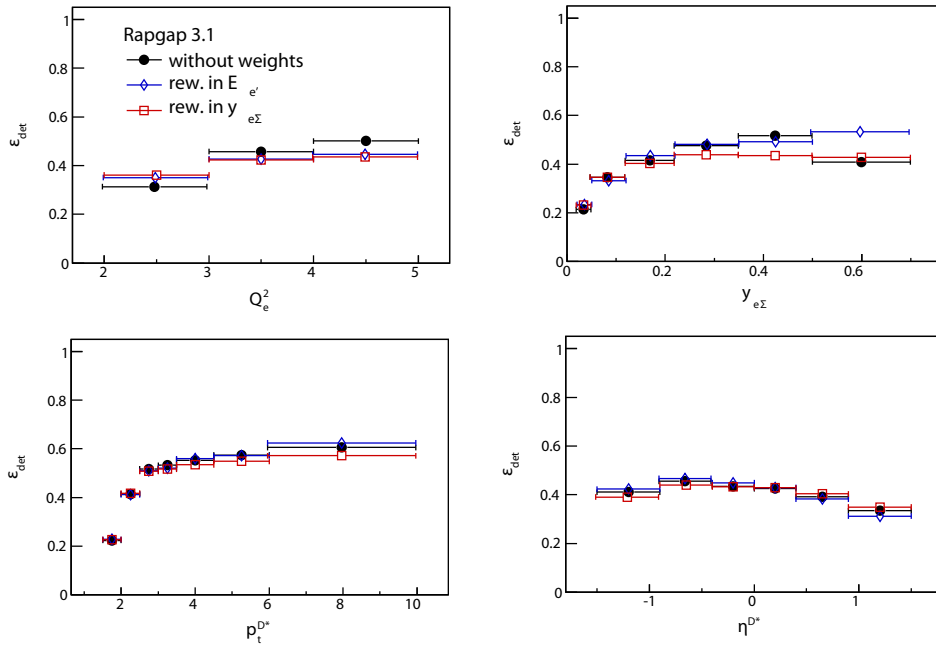


Figure 3.30: Comparison of the detector efficiency in Q_e^2 , $y_{e\Sigma}$, p_t^{D*} and η^{D*} as determined with the unweighted sample (black dots), the sample reweighted in $E_{e'}$ (blue open diamonds) and the sample reweighted in $y_{e\Sigma}$ (red open squares).

	σ_{tot} [nb]	total [%]	stat. [%]	sys. [%]
HERA II data	1.853	+8.3 -9.5	2.90	+7.8 -9.1
detector level MC	1.32608	+7.8 -9.1	0.18	+7.8 -9.1
hadron level MC	1.32653	0.20	0.20	–

Table 3.9: Total D^* meson production cross section σ_{tot} in nb and total, statistical and systematic uncertainties in the visible phase space at $2 < Q^2 < 5 \text{ GeV}^2$.

3.10 The Total D^* Meson Cross Section at low Q^2

The total cross section for D^* meson production is given by

$$\sigma^{\text{vis}} = \frac{N_{tot}^{D^*}}{\mathcal{L}} \cdot \frac{(1 - \mathcal{R} - \mathcal{P}) \cdot c_{rad}}{\mathcal{BR}(D^* \rightarrow K\pi\pi_s) \cdot \varepsilon_{det} \cdot \varepsilon_{trig}}, \quad (3.25)$$

where \mathcal{L} is the luminosity of the data sample, which amounts to

$$\mathcal{L} = (348 \pm 11) \text{ pb}^{-1} \quad (3.26)$$

From the total number of D^* s determined at low Q^2 , $N_{tot}(D^*)$, the fraction of reflections $\mathcal{R} = (4.6 \pm 0.018)\%$ (see section 3.7.1) and the fraction of photoproduction background $\mathcal{P} = (0.937 \pm 0.002)\%$ (see section 3.7.2) are subtracted. The factor $c_{rad} = 1.033 \pm 0.001$ (see section 3.8) corrects for higher order QED radiation. The branching ratio $\mathcal{BR}(D^* \rightarrow K\pi\pi_s)$ is needed because only D^* mesons decaying in the golden channel are counted. Finally, the cross section also has to be corrected by the detection and trigger efficiencies ε_{trig} and ε_{det} , which amount to (see sections 2.5 and 3.6, respectively):

$$\begin{aligned} \varepsilon_{det} &= (40.6 \pm 0.1)\% \\ \varepsilon_{trig} &= (93.7 \pm 0.4)\% \end{aligned}$$

The total visible cross section at $2 < Q^2 < 5 \text{ GeV}^2$ and its total, statistical and systematic uncertainties for the complete HERA II data sample, the Monte Carlo sample after detector simulation and reconstruction procedure (detector level MC) and the hadron level Monte Carlo sample (hadron level MC) is shown in table 3.9.

3.11 Differential Cross Sections

For each observable \mathcal{O} the single differential cross section $d\sigma/d\mathcal{O}$ is determined for each bin i of the observable by

$$\left. \frac{d\sigma^{\text{vis}}}{d\mathcal{O}} \right|_{\text{bin } i} = \frac{1}{\mathcal{L}} \frac{\Delta N_i^{D^*}(\mathcal{O})}{\Delta \mathcal{O}_i} \cdot \frac{(1 - \mathcal{R} - \mathcal{P}) \cdot c_{\text{rad}}}{\mathcal{BR}(D^* \rightarrow K\pi\pi_s) \cdot \varepsilon_{\text{det}} \cdot \varepsilon_{\text{trig}}}, \quad (3.27)$$

where the number of D^* s in bin i with width $\Delta \mathcal{O}_i$ is given by $\Delta N_i^{D^*}(\mathcal{O})$. Double differential cross sections are determined in a similar fashion:

$$\left. \frac{d\sigma_{\text{vis}}^2}{d\mathcal{O}_1 d\mathcal{O}_2} \right|_{\text{bin } i} = \frac{1}{\mathcal{L}} \frac{\Delta N_i^{D^*}(\mathcal{O}_1 \mathcal{O}_2)}{\Delta \mathcal{O}_{1,i} \Delta \mathcal{O}_{2,i}} \cdot \frac{(1 - \mathcal{R} - \mathcal{P}) \cdot c_{\text{rad}}}{\mathcal{BR}(D^* \rightarrow K\pi\pi_s) \cdot \varepsilon_{\text{det}} \cdot \varepsilon_{\text{trig}}}, \quad (3.28)$$

These cross section are not bin center corrected and therefore give only the (double) differential cross sections in the respective bin but is shown at the center of the bin in the following figures.

Figure 3.31 shows the single differential cross section in Q_e^2 , $y_{e\Sigma}$, $p_t^{D^*}$ and η^{D^*} . Inner error bars represent the statistical uncertainties σ_{stat} , outer error bars represent the total uncertainties σ_{tot} . For each bin they are determined by

$$\sigma_{\text{tot}} = \sqrt{\sigma_{\text{stat}}^2 + \sigma_{\text{sys}}^2}, \quad (3.29)$$

where σ_{sys} is the systematic uncertainty in that bin as described in 3.9. Below each cross section the ratio

$$R = \frac{\int d\mathcal{O} \frac{d\sigma^{\text{exp.}}}{d\mathcal{O}}}{\int d\mathcal{O} \frac{d\sigma^{\text{MC}}}{d\mathcal{O}}} \left. \frac{d\sigma^{\text{MC}}/d\mathcal{O}}{d\sigma^{\text{exp.}}/d\mathcal{O}} \right|_{\text{bin } i} \quad (3.30)$$

is presented as a measure to compare the shapes of Monte Carlo prediction and experimental data. The latter is presented as black dots, the solid red lines represent the predictions from RAPGAP and the dashed blue lines the prediction from CASCADE.

It can be seen that the prediction from both Monte Carlo generators, RAPGAP and CASCADE, undershoot the data. The shapes of all distribution are described well by both event generators, as the ratio plots below the cross section show.

The differential cross section as a function of Q^2 (fig. 3.31 a)) complements the measurements at higher virtualities. The three bins presented here lie in a region which, in the $D^{*\pm}$ production analysis of the HERA I period published by the H1 collaboration[25], was covered only by three broader bins. As shown in 3.32, the

3 D^* Meson Cross Sections

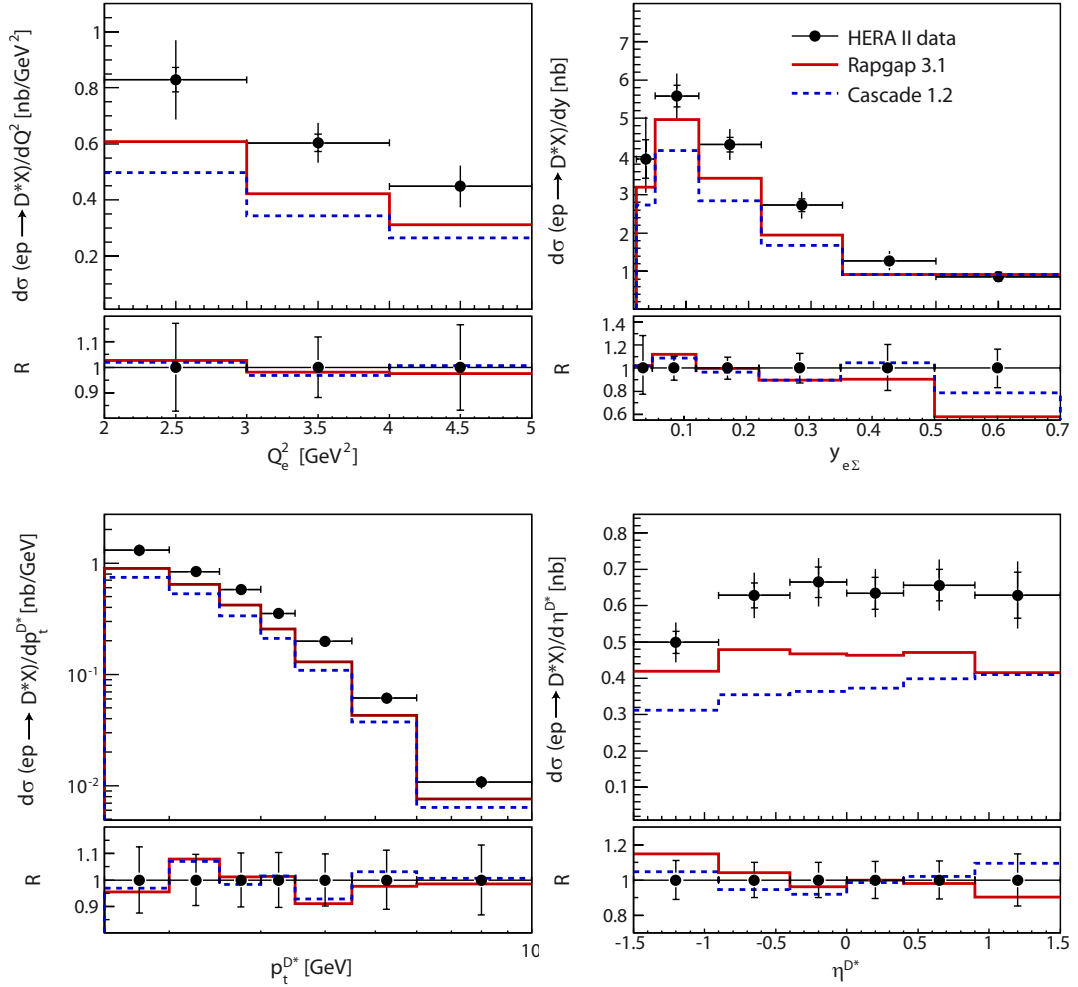


Figure 3.31: *The differential D^* meson production cross section $d\sigma(ep \rightarrow D^*X)$ in the range $2 < Q^2 < 5 \text{ GeV}^2$ as a function of a) Q_e^2 , b) $y_{e\Sigma}$, c) $p_t^{D^*}$ and d) η^{D^*} . Inner and outer error bars show the statistic and total uncertainties, respectively. The data are presented as black dots, predictions from RAPGAP as a solid red line and predictions from CASCADE as a dashed blue line. Below each differential cross section a ratio plot is shown comparing the shapes of the Monte Carlo predictions to the data. There only total uncertainties are shown.*

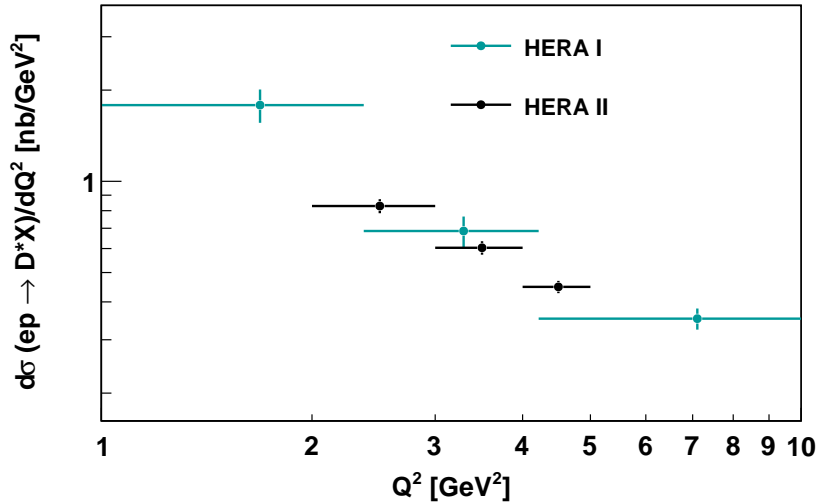


Figure 3.32: *The differential D^* meson production cross section $d\sigma(ep \rightarrow D^*X)/dQ^2$ as measured by the H1 collaboration using HERA I data (cyan) in the range $1 < Q^2 < 10 \text{ GeV}^2$ compared to the HERA II measurement presented here (black). Only statistical uncertainties are shown.*

HERA II data (black) offer a finer binning in Q^2 than was possible with the HERA I data (cyan).

The differential cross section as functions of the inelasticity y (fig. 3.31 b)) and the pseudo rapidity η^{D^*} (fig. 3.31 d)) are similar to the same cross sections measured at higher photon virtualities[1], although that analysis featured more bins along η^{D^*} . The $p_t^{D^*}$ -distribution (fig. 3.31 c)), on the other hand, is much steeper, as is expected at low Q^2 .

In figures 3.33 and 3.34 double differential cross sections are presented as functions of $y_{e\Sigma}$ in bins of Q_e^2 and as functions of η^{D^*} in bins of $p_t^{D^*}$.

$d\sigma^2/dQ^2 dy$ is in general well described by both Monte Carlo generators. Also the normalization is not as far off as in the single differential distributions. Shapes are equally well described by CASCADE and RAPGAP 3.1.

In the first y bin of the second Q^2 interval a notable deviation from the shapes of the other Q^2 intervals can be seen in the experimental data. Checks of efficiencies, correction factors and mass peak fits could not reveal the source of this deviation.

Also visible is that CASCADE undershoots the experimental cross section $d\sigma^2/d\eta dp_t$ more significantly than visible in the the other distributions. The description of the shapes is only slightly worse than from RAPGAP 3.1. This is seen in the distribution

3 D^* Meson Cross Sections

of the ratio R in figure 3.34.

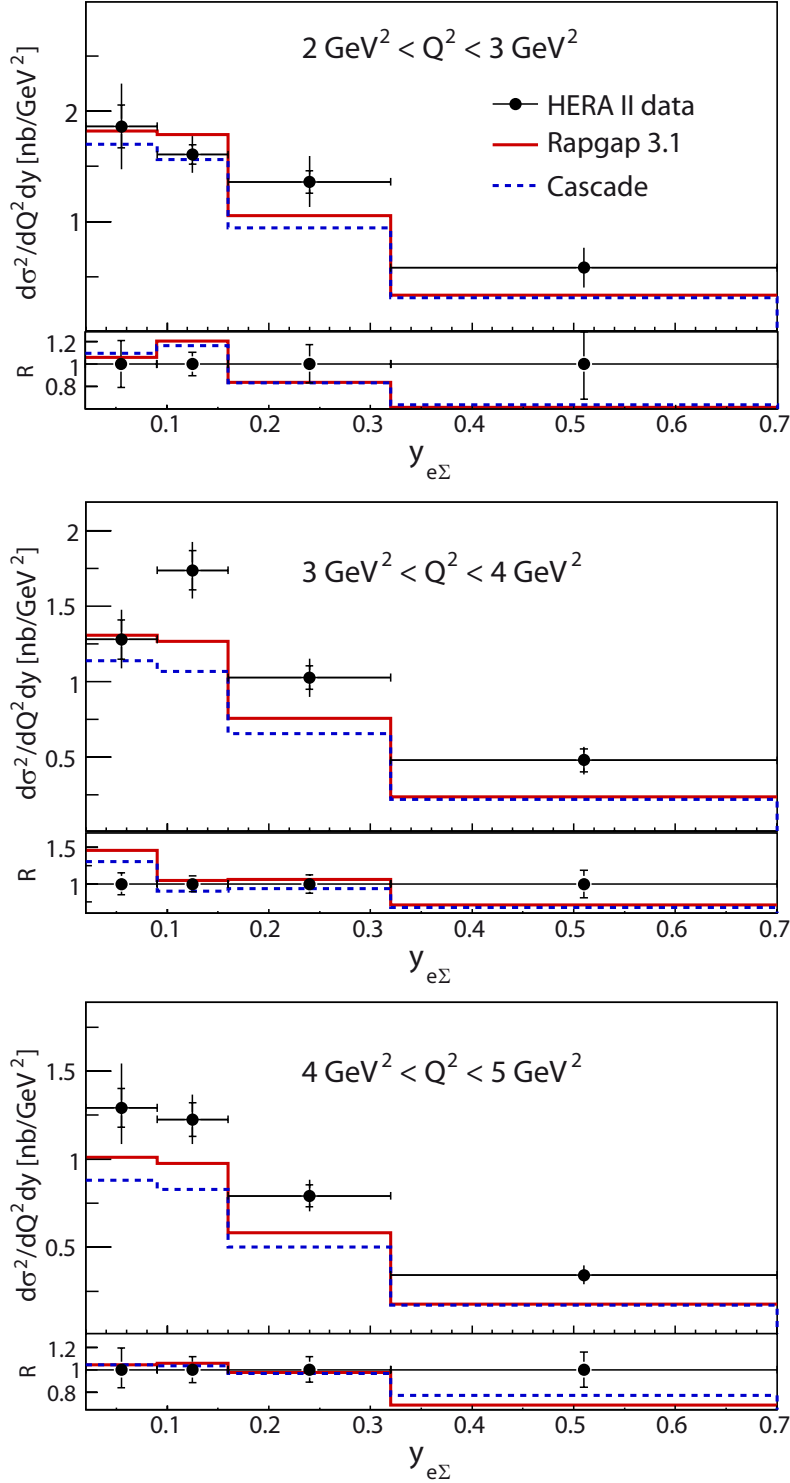


Figure 3.33: Double differential D^* meson production cross section $d\sigma(ep \rightarrow D^*X)$ in the range $2 < Q^2 < 5 \text{ GeV}^2$ as a function of $y_{e\Sigma}$ in bins of Q_e^2 . Inner and outer error bars show the statistical and total uncertainties, respectively. The data are presented as black dots, predictions from RAPGAP as a solid red line and predictions from CASCADE as a dashed blue line. Below each double differential cross section a ratio plot is shown comparing the shapes of the Monte Carlo predictions to the data. There only total uncertainties are shown.

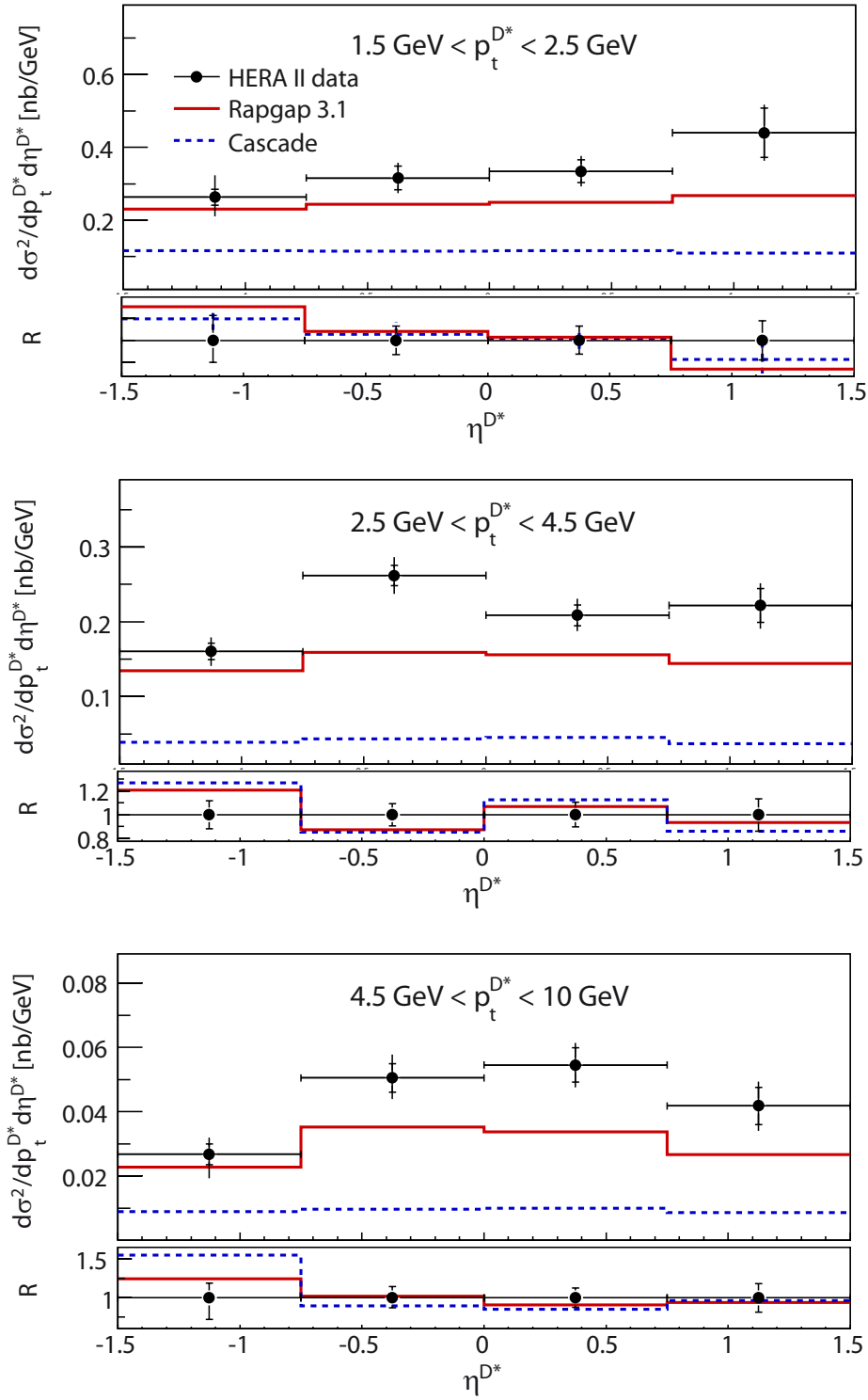


Figure 3.34: Double differential D^* meson production cross section $d\sigma(ep \rightarrow D^* X)$ in the range $2 < Q^2 < 5 \text{ GeV}^2$ as a function of η^{D^*} in bins of $p_t^{D^*}$. Inner and outer error bars show the statistic and total uncertainties, respectively. The data are presented as black dots, predictions from RAPGAP as a solid red line and predictions from CASCADE as a dashed blue line. Below each double differential cross section a ratio plot is shown comparing the shapes of the Monte Carlo predictions to the data. There only total uncertainties are shown.

4 Parton Distribution Functions

In chapter 1 the concept of parton densities has already been mentioned, as well as the basics of electron-proton scattering. This chapter offers deeper theoretical insight into the subject of parton distribution functions, starting with an introduction to factorization theorems in section 4.1 before the concept of parton evolution is explored in section 4.2. The theoretical approach behind unintegrated PDFs, called k_t -factorisation, is also explained in that section.

4.1 Factorization and the Hard Interaction

As Collins, Soper and Sterman stated in [39], “[factorization] allows us to derive predictions for [lepton-hadron and hadron-hadron large momentum transfer] cross sections, **by separating (factorizing) long-distance from short-distance behavior in a systematic fashion**”. The need for this comes from the fact that in QCD the coupling constant grows with the distance of interacting particles, making perturbative calculations possible only for short-distance processes. The long-distance parts which cannot be calculated perturbatively are accounted for by functions describing the probability to find partons in hadrons or, for hadronisation, hadrons to arise from partons.

In electron-proton scattering one makes use of the asymptotic freedom of QCD, which states that at high energy scales – i. e. short distances – the strong coupling constant is small and therefore the interaction between the quarks can be neglected compared to the photon-quark scattering process. This process can then be treated as an interaction between free particles so that perturbative methods can be applied.

While the radiation of the virtual photon by the electron can be approximated using the Weizsäcker-Williams formalism[40, 41], the low momentum component on the proton side, i. e. the interactions between the partons, is hidden in the parton densities – functions describing the momentum distribution of partons in the proton.

In lowest order perturbation theory a PDF $f_{i/h}(x)$ can be interpreted as the prob-

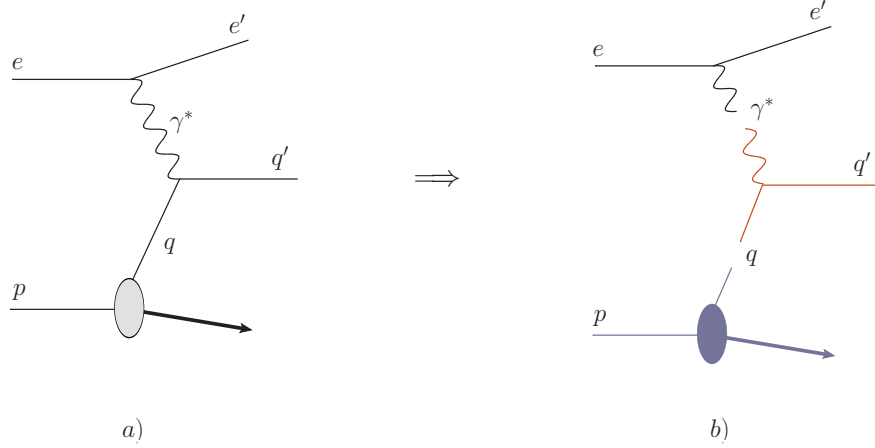


Figure 4.1: *Illustration of factorisation of the ep cross section: An electron e interacts with a quark q in a proton by exchange of a virtual photon γ^* (a)). The cross section can be factorized (b)) into the photon flux (red), the hard interaction (red) and the parton density (blue).*

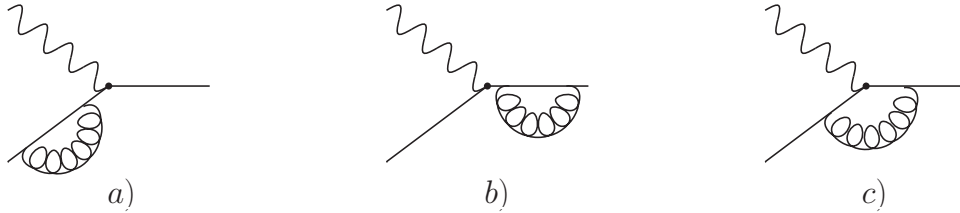


Figure 4.2: *The naive parton model $\gamma^*q \rightarrow q$ and its lowest order virtual pQCD corrections: the quark line (a and b) and the vertex corrections (c).*

ability of finding a parton of flavor i inside a hadron h with a momentum fraction x . The scattering cross section σ can then be factorized as follows:

$$\sigma \sim \phi(y) \otimes \hat{\sigma}(\gamma^*q \rightarrow q') \otimes f_{i/h}(x), \quad (4.1)$$

where $\phi(y)$ is the photon flux as a function of the inelasticity y ¹, $\hat{\sigma}(\gamma^*q \rightarrow q')$ is the cross section for the hard scattering of virtual photon and quark, and \otimes represents mathematical convolution. Figure 4.1 illustrates the separation of the photon flux (black), the hard scattering (red) and the parton density (blue). That this approximation holds is the subject of various factorisation theorems.

This picture does not yet include the strong interaction. The first step in incor-

¹Remember that in the proton rest frame the inelasticity y is the fraction of the electron energy carried by the virtual photon

porating perturbative QCD in this model is to consider the lowest order virtual and real corrections to $\gamma^*q \rightarrow q$. This is depicted in figures 4.2 and 4.3: for the virtual corrections the gauge boson of the strong interaction, the gluon, is introduced as a self interaction term of the quark line; the real corrections include initial and final state gluon radiation in QCD Compton (QCDC) processes $\gamma^*q \rightarrow gq$ and in addition boson gluon fusion (BGF) processes $\gamma^*g \rightarrow q\bar{q}$ where a boson, in this case a photon, interacts with a gluon via a quark propagator.

4.2 Parton Evolution

Factorisation theorems offer the possibility to calculate the hard scattering separately from the softer long distance processes. The momentum of a parton – quark and gluon alike – entering the hard scattering is not fixed but determined from parton distribution functions.

The concept of parton evolution answers the question of what soft processes can happen to a quark before the hard scattering occurs. It allows to account for mostly soft parton emission happening before the hard interaction without having to include these processes in the matrix element. This is done by *evolution equations*: perturbatively calculated equations bearing information of the influence of soft parton emissions on parton densities.

In the following two sections two approaches to this concept are introduced. The collinear factorisation approach (section 4.2.1) assumes that the influence of the transverse momentum of the parton entering the hard scattering is negligible. In the framework of k_t -factorisation (section 4.2.2), on the other hand, the transverse momentum is explicitly taken into account and plays an important role especially at low momentum fractions x_{Bj} .

4.2.1 Collinear Factorisation

At leading order (LO) perturbation theory the electron-quark scattering cross section can be written as:²

$$\frac{d^2\sigma}{dx dQ^2} = \frac{2\pi\alpha_{em}^2}{xQ^4}(1 + (1 - y)^2)F_2(x), \quad (4.2)$$

²The Callan-Gross relationship $F_L = F_2 - 2xF_1 = 0$ is used here.

4 Parton Distribution Functions

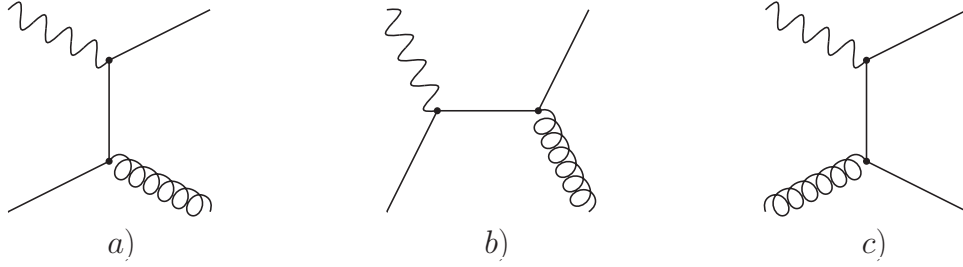


Figure 4.3: *The lowest order real corrections to $\gamma^*q \rightarrow q$: QCD Compton in a) and b), Boson Gluon Fusion in c).*

where α_{em} is the electromagnetic coupling constant and F_2 is the structure function for electron-proton scattering.

Considering only photon-quark scattering the structure function depends on the momentum distribution of quarks of flavor i in the proton:

$$F_2(x) = \sum_i e_i^2 x q_i(x), \quad (4.3)$$

where e_i is the charge of a quark of flavor i in units of the elementary charge $e = 1.602 \cdot 10^{-19}$ C. Note that at this stage the structure function as well as the quark density $q(x)$ only depend on the momentum fraction x , not on the energy scale Q^2 .

The momentum distribution of the quark is changed if the quark radiates a gluon before coupling to the virtual photon. Therefore the PDF $q_i(x)$ will change if the processes from figure 4.3 a) and c) are to be taken into account. Including the process $\gamma^*q \rightarrow qg$ from figure 4.3 a) introduces a scale dependence into the parton densities:

$$F_2(x, Q^2) = \sum_i e_i^2 \int_x^1 d\xi q_i(\xi, \mu_f) \left[\delta\left(1 - \frac{x}{\xi}\right) + \frac{\alpha_s}{2\pi} P_{qq}\left(\frac{x}{\xi}\right) \ln\left(\frac{Q^2}{\mu_f^2}\right) \right]. \quad (4.4)$$

Here ξ represents the proton momentum fraction carried by the incoming quark, while x is the proton momentum fraction of the quark line which coupling to the virtual photon. The factorisation scale μ_f serves the purpose of absorbing collinear divergences into the PDFs. The *splitting function* $P_{qq}(x/\xi)$ is derived from the matrix element of the process $\gamma^*q \rightarrow qg$ and represents the probability that a quark emitted a soft gluon. It depends only on the ratio x/ξ , which is the fraction of the incoming quark's momentum carried by the quark which couples to the virtual photon.

When the process $\gamma^* g \rightarrow q\bar{q}$ (fig. 4.3 c) is incorporated the splitting function P_{qg} for the gluon splitting $g \rightarrow q\bar{q}$ and the gluon density $g(x, Q^2)$ are introduced, resulting in the following contribution to the structure function:

$$F_2(x, \mu_f)|_{\gamma^* g \rightarrow q\bar{q}} = e_i^2 x \int_x^1 d\xi g(\xi, \mu_f) P_{qg} \left(\frac{x}{\xi} \right) \quad (4.5)$$

The scale dependence of the parton densities q_i and g is an important feature which can be further exploited by examining their derivatives with respect to $\ln \mu_f$:

$$\frac{\partial q_i(x, \mu_f)}{\partial \ln \mu_f} = \frac{\alpha_{em}}{2\pi} \int_x^1 d\xi \left[q_i(x, \mu_f) P_{qq} \left(\frac{x}{\xi} \right) + g(x, \mu_f) P_{qg} \left(\frac{x}{\xi} \right) \right] \quad (4.6)$$

$$\frac{\partial g(x, \mu_f)}{\partial \ln \mu_f} = \frac{\alpha_{em}}{2\pi} \int_x^1 d\xi \left[q_i(x, \mu_f) P_{gq} \left(\frac{x}{\xi} \right) + g(x, \mu_f) P_{gg} \left(\frac{x}{\xi} \right) \right] \quad (4.7)$$

These equations are known as the DGLAP (after **D**okshitzer, **G**ribov, **L**ipatov, **A**ltarelli and **P**arisi) equations. More generally equations which describes the change of a parton distribution function with the energy scale are called *parton evolution equations*. They treat the evolution of both quark (eq. (4.6)) and gluon (eq. (4.7)) densities under the influence of soft QCD radiation. The splitting functions $P_{ij}(x/\xi)$ represent the probability that a parton i with momentum fraction x originates from a parton j with a momentum fraction ξ by undergoing soft QCD radiation. For example, P_{qg} represents the probability that a quark q originates from a gluon g , i. e. that a gluon splits into a quark anti-quark pair. Note that these splitting functions do not, however, contain any kind of information about the emitted soft parton.

Factorisation Schemes

How the structure function F_2 can be factorized into long and short distance contributions depends on how finite $\mathcal{O}(\alpha_s)$ corrections are applied. Above no such corrections were introduced in the definition of the structure function: $F_2(x, Q^2) = \sum_i e_i^2 x q_i(x, Q^2)$. This treatment is called *DIS scheme*. It means that all QCD corrections are absorbed into the parton densities.

If only minimal contributions of finite $\mathcal{O}(\alpha_s)$ corrections are absorbed into the parton densities one ends up with a different form of the structure function with additional coefficient functions:

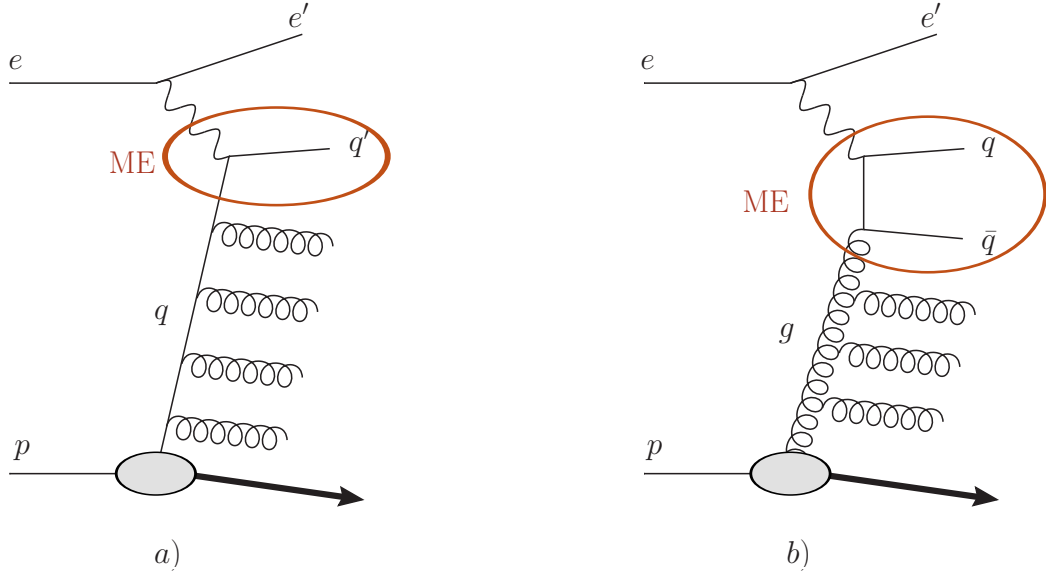


Figure 4.4: Examples of parton cascades for a) the photon-quark scattering $\gamma^*q \rightarrow q'$ and b) boson gluon fusion $\gamma^*g \rightarrow q\bar{q}$.

$$F_2(x, Q^2) = \sum_i e_i^2 \int_x^1 \frac{dx'}{x'} q_i(x', Q^2) \left\{ \delta\left(1 - \frac{x}{x'}\right) + \frac{\alpha_s}{2\pi} C_{MS} \left(\frac{x}{x'}\right) + \dots \right\}. \quad (4.8)$$

This scheme is called \overline{MS} (modified minimal subtraction) scheme and is a modification of the MS scheme introduced by t'Hooft and Weinberg. In practice it is more common than the DIS scheme.

The choice of scheme is, in principle, arbitrary. Once chosen, it has to be used consistently throughout all cross section calculations in order to obtain reliable predictions.

Parton Cascades

Parton evolution equations can be interpreted to account for the effect of parton showers not calculated in the matrix element on parton densities. As figure 4.4 a) illustrates the evolution of the quark density takes into account gluons emitted by the quark line before the hard process $\gamma^*q \rightarrow q$ takes place. Figure 4.4 b) depicts the gluon density evolution (eq. (4.7)) before the hard BGF process.

It is important to understand that by solving the evolution equations (4.6) and (4.7) one does not obtain any information on the emitted soft partons. What is obtained

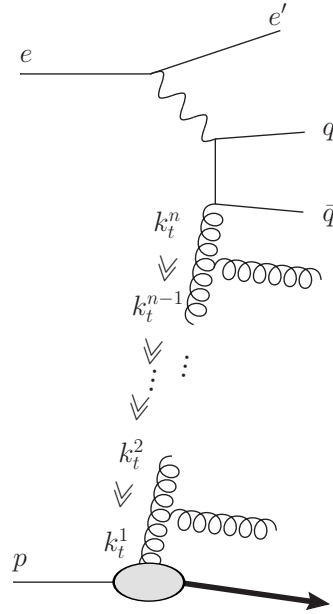


Figure 4.5: *Transverse momentum ordering for a gluon cascade in boson gluon fusion.*

is information about the influence of possible parton radiation on the parton density at the scale of the hard interaction. The larger the scale, the larger the phase space available for parton radiation.

If one considers, for example, the process $\gamma^*q \rightarrow q'$ (fig. 4.4 a)), the distribution of the scattered quark q' is affected by the parton evolution, but no information is gained about the gluons radiated in the parton cascade. When Studying BGF processes the parton evolution affects the momentum distribution of the outgoing quark and anti-quark, but again no information is gained about the gluons radiated in a parton cascade as shown in figure 4.4 b).

Strong Transverse Momentum Ordering

In order to derive equations (4.6) and (4.7) an important approximation has to be made:

$$k_t^1 \ll k_t^2 \ll \dots \ll k_t^{n-1} \ll k_t^n \ll \mu, \quad (4.9)$$

where k_t^i is the transverse momentum of parton i in the parton cascade, as illustrated in figure 4.5. This ordering is a consequence of the infrared divergence in the quark propagators of the partonic cross sections of QCD and BGF in the derivation of the splitting functions.

4.2.2 k_t -factorisation

In k_t -factorisation approaches parton densities explicitly depend on the transverse momentum of the partons, k_t , and enter the cross section σ in the following way:

$$\sigma \sim \int \frac{dx'}{x'} \int dk_t^2 \hat{\sigma}\left(\frac{x}{x'}, k_t\right) \mathcal{G}(x', k_t).$$

The cross section of the hard scattering, $\hat{\sigma}$, is convoluted with the *unintegrated* parton density $\mathcal{G}(x', k_t)$. Both depend explicitly on the longitudinal momentum fraction x' as well as the transverse momentum k_t . The k_t -dependence is also present in the matrix element of the hard scattering, which the partons enter off mass shell.

The unintegrated gluon density $\mathcal{G}(x, k_t)$ can be related to the collinear gluon by

$$xg(x, Q^2) \simeq \int^{Q^2} \frac{dk_t^2}{k_t^2} \mathcal{G}(x, k_t) \quad (4.10)$$

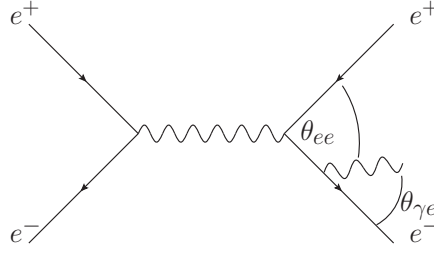
The transverse momentum of the partons becomes important particularly at low x . Here the strong ordering in transverse momenta is broken and the transverse momenta of all partons involved in a parton cascade can take on any kinematically allowed value.

Two approaches are presented in the following sections: the BFKL approach by Balitsky, Fadin, Kuraev and Lipatov, which is expected to become important at small momentum fractions x , and the CCFM approach by Catani, Ciafaloni, Fiorani and Marchesini, which is valid at both large and small x .

The BFKL approach

Balitsky, Fadin, Kuraev and Lipatov addressed the problem of the scattering of two perturbative hadrons where, on one hand, the squared center-of-mass energy, s , is large compared to the transverse scales t_1 and t_2 of these objects, $t_i \ll s$. On the other hand the transverse scales are demanded to be large compared to the QCD scale, $t_i \gg \Lambda_{QCD}$, so that perturbation theory is applicable. In deep inelastic scattering one expects phenomena related to the BFKL approach to arise at small momentum fractions x , since $x \sim t/s \ll 1$.

At these small momentum fractions it is clear from the splitting functions that

Figure 4.6: Illustration of angular ordering in $e^+e^- \rightarrow e^+e^-\gamma$.

gluons drive the evolution:

$$\begin{aligned}
 P_{qq}, P_{gq} &\simeq \text{const.}, \\
 P_{qg} &\simeq \frac{4}{3} \frac{1}{z} \\
 P_{gg}(z \ll 1) &\simeq 6 \frac{1}{z} > P_{qg}
 \end{aligned}$$

The limit $z \ll 1$ implies that in this kinematic regime gluon cascades dominate the cross section, and since $z = x_{i+1}/x_i$ it also implies a strong ordering in longitudinal momenta:

$$x_0 \gg \dots \gg x_i \gg \dots \gg x_{Bj} \quad (4.11)$$

In the collinear scenario we also have a strong ordering in the transverse scales, e. g. $t_1 \gg t_2$. BFKL studied a case where this no longer needs to hold. Rather the case where transverse scales are of the same order, $t_1 \sim t_2$, has to be considered. Since the transverse momentum k_t of a parton is essentially given by the transverse scale of the hadron, $k_t^2 \sim t$, we have a situation where the strong ordering in transverse momenta (eq. 4.9) is not valid anymore. Instead the transverse momenta of all partons taking part in the evolution can have any kinematically allowed value, which is often referred to as a *random walk* in k_t . The parton densities themselves, then, also explicitly depend on the transverse momentum of the partons, as described in the introductory note above.

Color Coherence, Angular Ordering and the CCFM approach

In order to get a consistent description of the kinematics of all final state partons one also has to account for the transverse momentum of partons emitted in a parton cascade. This is done in the CCFM approach, which bases its study of parton cascades

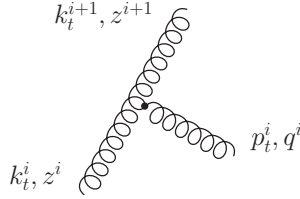


Figure 4.7: *Definitions of the variables for gluon splitting in the CCFM approach.*

on color coherence effects. Instead of the strong k_t -ordering of the collinear approach (eq. (4.9)) or the strongly ordered momentum fractions in BFKL (eq. (4.11)), color coherence yields an ordering in emission angles. This angular ordering is a general feature of gauge theories and not only of QCD. It can also be found, for example, in the process $e^+e^- \rightarrow e^+e^-\gamma$, in which emission angle of the photon can never exceed the opening angle of the electron positron pair: $\theta_{\gamma e} < \theta_{ee}$ (see fig. 4.6).

The angular ordering of gluon³ emissions, $\theta^i < \theta^{i+1}$, leads to the following statement:

$$z^i q^i < q^{i+1} . \tag{4.12}$$

Here $q^i = p_t^i / (1 - z^i)$ is the rescaled transverse momentum of the *emitted* gluon, and z^i the momentum fraction carried by the *incoming* gluon, as shown in figure 4.7.

A few features of this ordering are worth mentioning. Instead of the strong ordering in transverse momenta of the *propagating* partons in the DGLAP approach we now have an ordering for the rescaled transverse momenta of the *emitted* gluons. At large momentum fractions z^i this translates into a weak ordering for the transverse momentum of the propagating gluons, $k_t^i < k_t^{i+1}$. At small z^i , however, the transverse momenta can obtain nearly any value, since then the smallness of z^i fulfills the ordering for nearly any value of q^i .

Thus we see that at relatively large x a DGLAP-like ordering, although not as strong, is obtained, while at small x a feature of the BFKL evolution, the random walk in k_t , is reproduced. This, among other features, makes the CCFM approach a promising candidate for a unified description of parton showers both at large and small momentum fractions x .

The integral form of the CCFM equation reads[9, 42, 43, 44, 45]:

³As stated before, at small x the gluon density dominates over the quark densities, which is why in the following only gluons are considered.

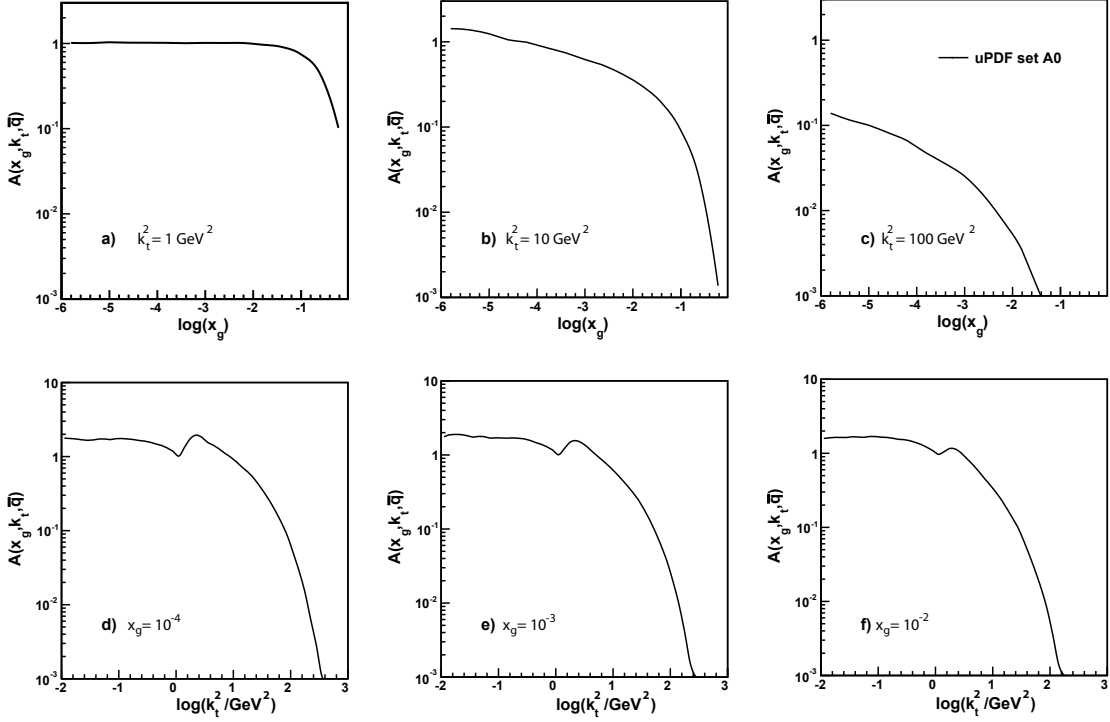


Figure 4.8: The unintegrated gluon density from set A0 as a function of $\log x_g$ in bins of the transverse momentum k_t (a - c) and as a function of $\log k_t$ in bins of x_g (d - f).

$$\mathcal{A}(x, k_t, \bar{q}) = \mathcal{A}_o(x, k_t, \bar{q}) + \int \frac{dz}{z} \int \frac{dq^2}{\pi q} \theta(\bar{q} - zq) \Delta_s(\bar{q}, zq) P_{gg}(z, k_t, q) \mathcal{A}\left(\frac{x}{z}, k_t', q\right) \quad (4.13)$$

Here $\bar{q} = \hat{s} + Q^2$ is the upper scale of the parton evolution, so that for n emissions $z_n q_n < \bar{q}$. The Sudakov form factor $\Delta_s(\bar{q}, zq)$ describes the probability of parton emission between the energy scales \bar{q} and zq , while the theta-function $\theta(\bar{q} - zq)$ ensures the ordering in of equation (4.12). The splitting function P_{gg} now depends on k_t , as does the unintegrated parton density $\mathcal{A}(x, k_t, \bar{q})$.

Unintegrated Parton Densities

The unintegrated parton densities $\mathcal{A}(x, k_t, \bar{q})$ are obtained by fits to deep inelastic scattering data such as structure functions and non-inclusive final state measurements like jet or heavy flavor production. For the use in the Monte Carlo generator CASCADE various sets are available. They differ in details such as the renormalization

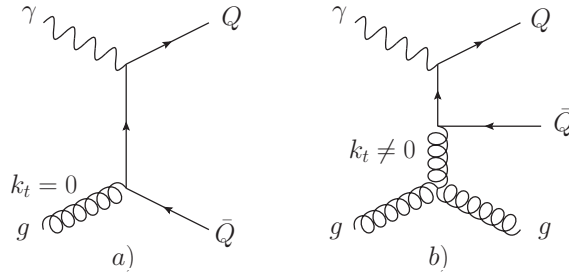


Figure 4.9: *Two examples for heavy quark production: a) LO and b) NLO contribution. For heavy quark production with three jets in the final state, the diagram in b) would be the LO contribution. What is more, the collinear approach means that in a) the gluon producing the $Q\bar{Q}$ pair carries no transverse momentum while in b) $k_t \neq 0$.*

scale, the splitting functions or the cut-off for the transverse momentum k_t .

For comparison to data the *set A0* has been used, which is described in reference [46]. Figure 4.8 shows the unintegrated gluon distribution of set A0 as function of $\log x_g$ in bins of k_t (a - c) and as a function of $\log k_t$ in bins of x_g (d - f).

4.3 Next-To-Leading Order Corrections

In the previous sections all QCD calculations were given in first order of the strong coupling α_s . In processes such as heavy quark production, $\gamma q \rightarrow Q\bar{Q}$, this is the leading order (see fig. 4.9 a)). Other processes such as heavy quark production with three jets in the final state cannot be accounted for by a matrix element calculation of first order in α_s , because all the first order calculations only have two particles in the final states (e.g. $\gamma q \rightarrow qg$). An example for a leading order contribution for heavy quark production with three jets is $\gamma q \rightarrow Q\bar{Q}g$, as depicted in figure 4.9 b). Note that for heavy quark production without any additional requirement figure 4.9 b) is already next-to-leading order (NLO).

Every perturbative calculation includes approximations, and higher order contributions represent corrections to these. An example is the transverse momentum k_t of a gluon splitting into a heavy quark pair (fig. 4.9 a)). In the collinear approach $k_t = 0$ in the LO diagram. In the NLO contribution, however, $k_t \neq 0$ for this gluon, because the collinear approach requires the *incoming* gluon to be on-shell. In figure 4.9 b) this is not the gluon that produces the heavy quarks. There the heavy quarks originate from a gluon propagator which may obtain any k_t .

As described in the previous section, the k_t -factorisation approach already accounts for a finite transverse momentum of the gluon producing the heavy quark pair. A correct and thorough treatment of kinematics already at leading order means that NLO corrections potentially become smaller than in the collinear approach.

5 Event Generators and Parton Distributions

For collider experiments it is of crucial importance to model the final state of collisions in order to correct for detector effects in the cross section determinations and to compare measurements to theoretical predictions. One possibility is to simulate collisions by using random numbers to choose a hard process from a wide array of available matrix elements according to the kinematics of the event. In such a simulation various effects like QED radiation, parton evolution, fragmentation and hadronisation are taken into account. Such simulations are referred to as *Monte Carlo (MC) simulations*, *Monte Carlo event generators* or simply *Monte Carlos*.

Section 5.1 provides a general overview of how these physics phenomena are accounted for in event generators. The treatment of parton evolution is of particular interest here and will be described in more detail in section 5.2.2.

5.1 Simulation of scattering events

Quantum physics can only make probabilistic statements about underlying processes of observable phenomena. This means that initial conditions of colliding particles do not determine the outcome of a single collision, no matter how accurately they are known. Particle collisions are therefore simulated by using random numbers to choose one process for every single event. Figure 5.1 gives an overview of what is needed for such an event simulation.

By generating a large number of simulated events one can then obtain statistical predictions such as scattering cross sections for a wide array of measurable quantities.

5.1.1 Matrix Element Calculation

The first step is the calculation of the matrix element (ME) at a fixed order of the strong coupling α_s . The event generators used in this analysis perform this calculation

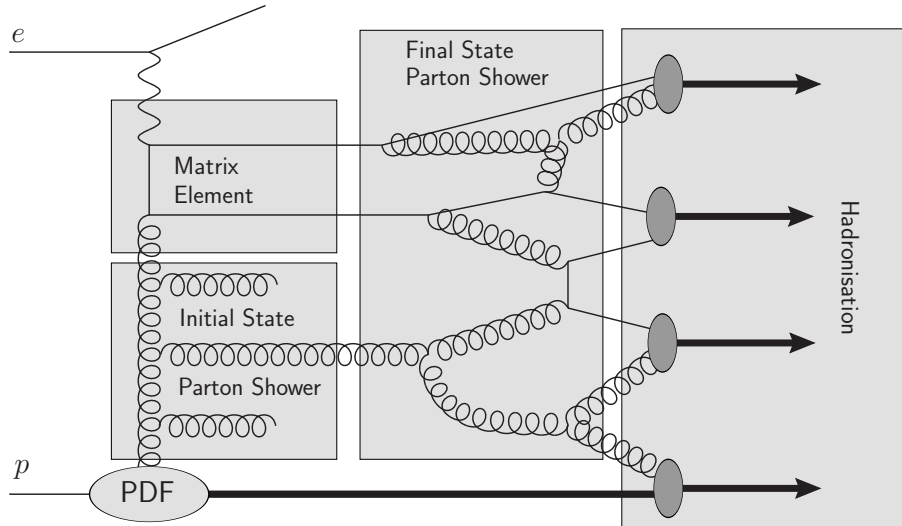


Figure 5.1: Overview of the various stages of event generation in Monte Carlo generators.

to first order in α_s . This does include the quark parton model (QPM) process as well as the BGF and QCD-Compton processes which in figure 4.3 were considered as real corrections to the QPM.

In the event generator CASCADE only the BGF process is included, because CASCADE is dedicated to study gluon evolution at small momentum fractions x where the BGF process dominates the cross section.

5.1.2 Process Selection

For electron-proton collisions the matrix element is calculated at a certain photon virtuality Q^2 and inelasticity y using Monte Carlo techniques for integration. Because the cross section is calculated in this step for each process contributing to the matrix element, the relative contribution of every process to the total cross section at that particular Q^2 and y can be determined. Figure 5.2 illustrates schematically how a process is then selected:

- the relative cross sections σ_i/σ_{tot} of the processes i are calculated
- the interval $[0, 1]$ is divided according to the relative cross sections
- a random number r between 0 and 1 is generated

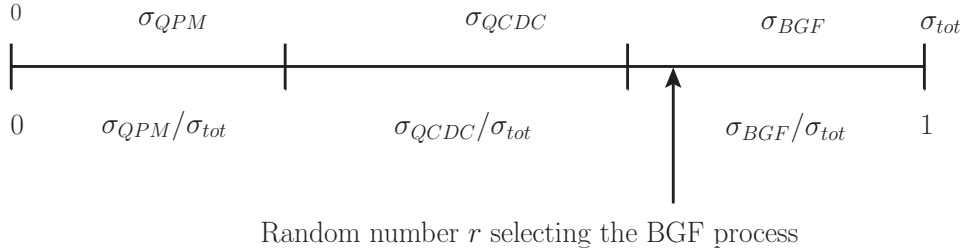


Figure 5.2: *Schematic example of process selection in MC simulations. The upper labels represent the cross sections σ_i of the QPM, QCDC and BGF processes at the generated Q^2 and y and span values between 0 and the total cross section σ_{tot} at the generated Q^2 and y . The lower labels are the relative contributions σ_i/σ_{tot} of the individual processes and span values from 0 to 1. A process is selected by generating a random number between 0 and 1 and examining afterwards in which interval it is found, indicated by the arrow.*

- the interval in which r lies is determined and the corresponding process i is selected for the event

5.1.3 Parton Showers

After the process selection higher order effects not accounted for in the matrix elements are approximated by parton showers (see fig. 5.1). In each event this is done by integration of the evolution equation for the selected process, as described in more detail in section 5.2.1.

One has to separate initial state and final state parton showers. Although intuitively IS parton showers take place before the hard scattering they are applied only after the calculation of the matrix element because this allows a more efficient event generation. This is called backward evolution because one starts at the highest possible energy scale and evolves the parton density backwards towards a lowest cut-off energy scale. As explained in more detail below (section 5.2.1) initial state parton radiation affects the four momentum of the hard parton which, in the matrix element, is considered the incoming particle.

Final state parton showers are also calculated with evolution equations. Since the phase space for this is not as limited they can be applied straight forward from the outgoing partons of the matrix element until some condition has been reached.

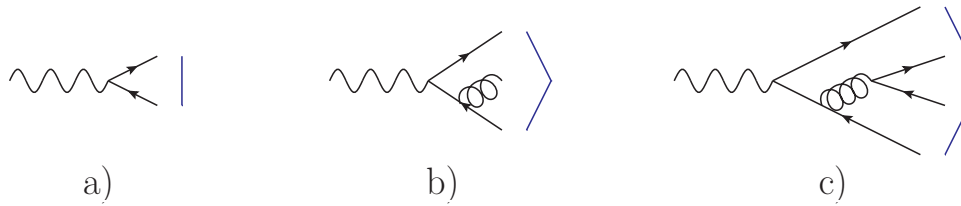


Figure 5.3: *Example of a breaking string in the Lund string model. Quarks are represented by the endpoints of strings while kinks represent gluons, as illustrated in b).*

5.1.4 Fragmentation and Hadronisation

In order to produce hadrons out of the quarks one has to apply a mechanism modeling hadronisation and fragmentation. In the non-perturbative phase space region where parton showers cannot be applied anymore one has to rely on phenomenological models for hadron production. The two most widely spread models are the Lund string model[47] and the cluster fragmentation model[48, 49].

The Lund String Model

The Lund string model considers color connections between quarks as strings. In this picture gluons carrying two color charges are represented by kinks on a string, and the splitting of a gluon into two quarks means that a string breaks at a kink. This is illustrated in figure 5.3 for the process $\gamma \rightarrow q\bar{q}q\bar{q}$, where the blue lines represent color strings between two quarks. When created from the splitting of the photon the two quarks are connected by a string (fig. 5.3 a)). When one of the quarks emits a gluon, the string gets kinked (fig. 5.3 b)), and the breaking of the string at the kink means the creation of a quark anti-quark pair from the splitting of the gluon (fig. 5.3 c)).

The Cluster Fragmentation Model

Another one also widely used in high energy physics is the cluster fragmentation model. In this model clusters are formed out of color singlet quark anti-quark or quark diquark pairs remaining after final state parton showers. If any gluons are left they are forced to split into quark anti-quark pairs before clustering.

Clusters themselves cannot yet be considered hadrons but decay into two hadrons each. Only on the low and high end of the cluster mass spectrum cluster decay has to be treated differently.

A cluster with too low a mass for decaying into two hadrons forms only one hadron and the excess momentum is distributed equally onto neighboring clusters.

On the other hand a heavy cluster can have such a large mass that the two daughter hadrons would have unnaturally high momenta. In this case it decays into daughter clusters with additional light quark anti-quark pairs whose momenta are aligned with the mother cluster's. The mechanism of cluster-to-cluster decay is similar to the Lund string fragmentation.

This model is used for example in the Monte Carlo generator HERWIG (Hadron Emission Reaction With Interfering Gluons).

Fragmentation Functions

The mechanism with which hadronisation and fragmentation models are applied in MC simulations is similar to parton density evolution, only that instead of parton densities so called fragmentation functions $D_{h/q}(z)$ are evolved. These represent the probability of a hadron h being produced from a quark q with a fraction z of the quark's momentum. A parametrization that is widely used for heavy quarks is the Peterson fragmentation function

$$D_{h/q}(z) = \frac{N}{z \cdot (1 - 1/z - \varepsilon_q(1 - z))^2}, \quad (5.1)$$

where N normalizes the function to 1 and ε_q represents the hardness of the fragmentation process. In figure 5.4 the Peterson function is shown for the fragmentation of a charm quark into a D^* meson with $\varepsilon_c = 0.05$. This value has been used here in all Monte Carlo generators.

5.1.5 Decays Of Unstable Particle

The results of the fragmentation and hadronisation phase are four momenta of hadrons and leptons. Because some of the hadrons have lifetimes too short for the particle to be detected decays of unstable hadrons have to be simulated as well. An example are D^* mesons, which are measured in this analysis by selecting a particular decay channel¹, $D^* \rightarrow K\pi\pi$.

¹For more details see chapter 3.

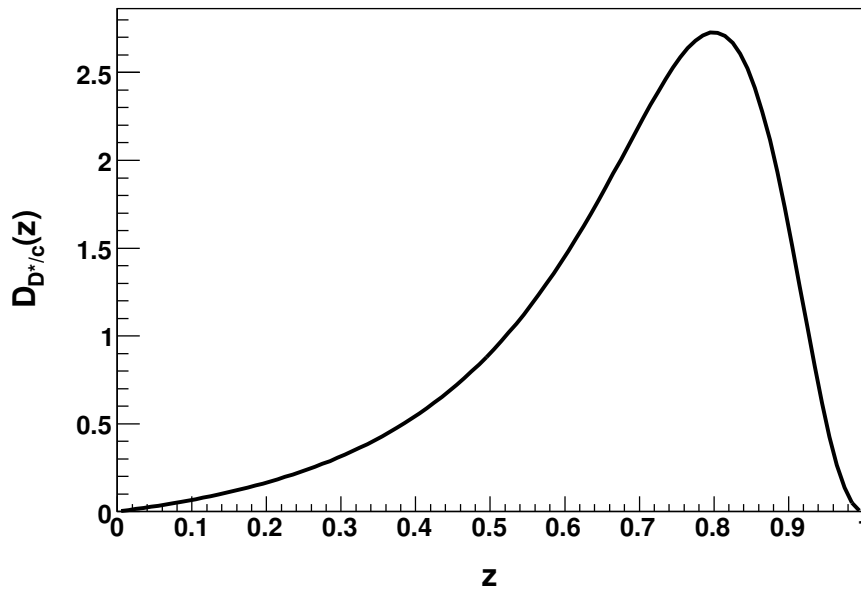


Figure 5.4: *Peterson fragmentation function for the production of D^* mesons out of charm quarks with $\varepsilon_c = 0.05$.*

5.2 Parton Evolution in Event Generators

The two different approaches to parton evolution introduced in section 4.2 each have their advantages and disadvantages when it comes to implementing them in event generators. In section 5.2.1 I describe how the collinear approach is handled in MC generators. A short review of a proposal how the general concept of parton densities can be redefined for event generators is given in section 5.2.2, followed by a comment on why unintegrated parton densities are more suited for the implementation in MCs in section 5.2.3.

5.2.1 The Collinear Approach in Event Generators

In order to correctly account for parton showers one has to implement evolution equations such as equations (4.6) and (4.7). This is usually done by rewriting these equations in an integral form:

$$f(x, \mu) = f(x, \mu_0) \Delta_s(\mu, \mu_0) + \int \frac{d\xi}{\xi} \int \frac{d\mu'}{\mu'} \frac{\Delta_s(\mu')}{\Delta_s(\mu)} P(\xi) f\left(\frac{x}{\xi}, \mu'\right), \quad (5.2)$$

where the parton density f is to be evaluated at the scale μ . The Sudakov form factor Δ_s is present again, giving probabilities of emission between the scales μ and μ_0 . Especially this last feature is very useful for the implementation into a computer program, because in combination with random numbers it offers a simple method to decide – event by event, parton by parton – if a parton is emitted at a certain scale or not.

As explained in section 4.2 the DGLAP equations do not give any information on emitted partons. Since in a computer simulation the whole final state is of interest one has to introduce such information by hand. This can lead to inconsistent treatment of parton emissions and parton evolution. Note that the two are not necessarily the same: parton evolution refers to the influence of parton emissions on parton distribution functions under certain assumptions, e. g. collinearity, transverse momentum ordering or on-shell partons.

An example for inconsistent treatment of parton evolution and parton emission in event generators is the strong transverse momentum ordering of the collinear approach (eq. (4.9)). Technically it is only possible to implement a weak ordering $k_t^i < k_t^{i+1}$, so that the strict approximation of the DGLAP formalism is never fully satisfied in any Monte Carlo program based on it.

5.2.2 PDF4MC

The inconsistencies mentioned above do not mean that leading order Monte Carlo generators are inappropriate for comparing theoretical predictions to data. MC generators are valuable tools needed by experimentalists to account for, e.g., detector effects.

It has thus been proposed[50] that rather than using PDFs which are numerically determined from theory calculations based on completely different approaches, dedicated parton densities should be determined for each individual MC generator. Event generators do not strictly implement factorisation theorems like the DIS or the \overline{MS} scheme and therefore need a dedicated definition of MC PDFs as well as a dedicated MC factorisation theorem.

The project PDF4MC in the Helmholtz Analysis Center at DESY is working on implementations of parameter estimation tools for the determination of PDFs for the Monte Carlo generators RAPGAP and PYTHIA. The general method is explained in chapter 6.

5.2.3 Unintegrated Parton Distributions in Monte Carlo Generators

The evolution equation (4.13) is used for gluons in the MC generator *CASCADE* in its integral form to calculate the probability of parton emission as described in section 5.2.1. In contrast to MCs based on the DGLAP formalism the CCFM equation allows MC generators based on it to keep track of the longitudinal *and* transverse momenta of both emitted and propagating gluons. MC generators based on DGLAP have to add information about the transverse momentum each time a parton is emitted, while this information is already present in the CCFM equation.

That the CCFM approach offers information on both the influence of parton emission on uPDFs and on the emitted partons themselves makes it more suited for an implementation in MC event generators than the DGLAP approach. This is also the reason why the CCFM approach does not necessitate parton densities dedicated to MC generators. Since the full information of the uPDFs is used in the evolution and no information is added, as is the case for collinear MCs, uPDFs are universal.

Unfortunately the calculation of matrix elements – especially at NLO – is far more complicated than in the DGLAP approach, which is why there is only a limited number of processes yet for which a matrix element has been derived. What is more in the MC generator *CASCADE* only gluon evolution is implemented so far, neglecting effects of valence and sea quark distributions. Especially at low momentum fractions x this does not pose a problem, because the strongly gluon dominates this phase space region.

6 Determination of Parton Densities

The basic formalism of parton density extraction and a description of the choice of the parametrization of the initial parton densities is outlined in section 6.3. There are, in principle, two methods to obtain parton densities from experimental data. The *analytic method* described in section 6.1 is based on numerical solutions of analytic expressions, while the Monte Carlo method described in section 6.2 uses event generators to obtain PDFs. First Results are presented in section 6.4.

The results are only a rough sketch of what is possible inside this framework. The treatment of systematic errors, correlated and uncorrelated errors is not covered, nor are uncertainties on the extracted parameters determined here.

The presentation here is based on the book “Deep Inelastic Scattering” by Devenish and Cooper-Sarkar [51], where a thorough description of the subject can be found in chapter 6.

6.1 The Analytic Method

The more common method is to start with a set of initial parton densities $f_i^0(x)$ which is evolved by numerically solving the evolution equations (4.6) and (4.7). Cross sections are then calculated which can be compared to measurements. The difference between measurement and theoretical prediction is then minimized by iteratively adjusting the parameters of the initial parton densities and in each step comparing theory prediction and experimental data.

Collaborations like CTEQ[52] and MSTW[53] use this method with data from a large set of experiments¹ in order to extract parton densities. The collaborations H1 and ZEUS both determined sets of PDFs with this method using their own data of the proton structure function F_2 . Their results are widely used in predictions for

¹In [51] pp. 146,147 a complete list of experiments contributing to global PDF fits is given.

proton collision experiments such as H1 and ZEUS, the CDF and D0 collaborations at Tevatron or the LHC collaborations CMS, ATLAS, ALICE and LHCb. Since analytic expressions are solved by numerical expressions I use the term *analytic method*.

6.2 The Monte Carlo Method

The method which was used for this thesis follows a different path. The calculation of cross sections is not done by numerically solving analytical expressions, but instead with Monte Carlo event generators. In this method a set of initial parton densities is used in order to generate a certain number N_{evt} of events. After an event selection is applied cross sections of certain processes are calculated and compared to experimental data. Similar to the analytic method, the difference between theory prediction and data is then minimized by iteratively adjusting the parameters of the initial parton density and in each step *generating N_{evt} events*.

This method has the advantage of giving parton densities dedicated to a certain MC generator. Instead of treating parton densities as universal quantities applicable by every kind of theoretical prediction and event generator, this method incorporates the PDF4MC concept mentioned in section 5.2.2.

In this analysis, however, unintegrated parton densities were obtained by the event generator CASCADE. As mentioned in section 5.2.3 uPDFs are universal in the sense that event generators based on the CCFM approach have no need for dedicated uPDFs and vice versa: uPDFs determined by the Monte Carlo method using CASCADE are universally applicable in numerical methods based on CCFM.

6.3 Outline of the Fitting Formalism

The fitting formalism is based on the χ^2 method, where the value

$$\chi^2 = \sum_{i=n}^{22} \frac{(\sigma_i^{meas} - \sigma_i^{theo})^2}{u_i^2} \quad (6.1)$$

is calculated from the single differential cross sections determined in this analysis (sec. 3.11). The index i runs over all 22 bins of the cross sections $d\sigma/dQ^2$, $d\sigma/dy$, $d\sigma/dp_t^{D^*}$ and $d\sigma/d\eta^{D^*}$ presented in section 3.11. The value χ^2 is the sum of the squared differences of each measured value σ_i^{meas} and the corresponding theoretical prediction

σ_i^{theo} in units of the statistical measurement uncertainties u_i .² In order to calculate χ^2 the software package HZTOOL[13] (see section 1.5.2) is interface with CASCADE .

Since for a large number of data points χ^2 as defined in equation (6.1) can become large it is common to use the quantity χ^2/ndf to estimate the quality of a theoretical description of experimental data, where ndf is short for number of degrees of freedom. These are given by the number of data points less the number of free parameters. Values of a good theoretical description lie around $\chi^2/ndf \approx 1$. This is because $\chi^2/ndf = 1$ means that on average the theoretical prediction is one standard deviation away from the data.

When determining parton densities with the Monte Carlo method from the single differential D^* meson production cross sections measured in this thesis, χ^2 is calculated from events generated by the Monte Carlo generator CASCADE which have passed the event selection in table 3.3. As described above it is minimized by changing the initial parton density in order to find a minimum χ^2 value.

6.4 Unintegrated Gluon Densities Extracted from D^* Meson Production at low Q^2

Collaborations working on PDF extraction use the general form

$$f_i(x) = N_i \left(\frac{1}{x}\right)^{A_i} (1-x)^{B_i} P_i(x) \quad (6.2)$$

as parametrization of initial PDF s of flavor i . Here N_i is a normalization factor which is varied together with the exponents A_i and B_i to fit the data. The exponent A_i of the $\frac{1}{x}$ -term is responsible for the low x behavior of the parton density while B_i handles the large x behavior by means of the $(1-x)$ -term. Some groups like CTEQ or MSTW (formerly MRST) use an additional polynomial $P_i(x)$, usually a polynomial in x or \sqrt{x} , for example:

$$P_i(x) = (1 + C_i x^{D_i}) \quad (6.3)$$

$$P_i(x) = (1 + C_i \sqrt{x} + D_i x) . \quad (6.4)$$

²Systematic uncertainties have to be treated differently are not included in the fits here.

CASCADE only treats gluon evolution, so that only the unintegrated gluon density is determined here. The initial gluon density used here is given by

$$\mathcal{A}_0(x, k_t) = N_g \left(\frac{1}{x}\right)^{A_g} (1-x)^{B_g} (1+C_g x) e^{-\frac{k_t^2}{k_0^2}}. \quad (6.5)$$

The parameters N_g and A_g are determined by generating $N_{evt} = 1\,000\,000$ events with CASCADE, calculating χ^2 , changing the parameters and repeating the procedure until a minimum χ^2 is found. The minimization is carried out with the software package MINUIT using the simplex method. Both are explained in the MINUIT manual[54]. The parameter $k_0 = 1$ GeV parametrizes the width of the initial k_t distribution and is not varied in the fit. The k_t distribution is therefore assumed to have a Gaussian shape with a maximum at 0 GeV and a width of 1 GeV.

In reference [55] fits of unintegrated gluon densities to inclusive structure function data were presented. The results of those fits were to serve as starting values for the gluon density parameters here. That the results of reference [55] give sensible values is tested in parameter scans, i.e. one parameter was changed while all other ones were fixed. This gives a distribution of χ^2 values as a function of the scanned parameter.

The parameter B_g is responsible for the high x behavior and is not very sensitive to the data used here. As figure 6.1 illustrates a minimum χ^2 is achieved with a value $B_g \approx 4$, which corresponds nicely to the value used in reference [55]. Around this value the χ^2 distribution is more or less flat, which is why it has been fixed to $B_g = 4$ in the extraction of the gluon density parameters.

A scan of the parameter C_g showed a minimum at around $C_g \approx 1.3$ (see fig. 6.1, lower right plot). This contradicts the value found in [55], which was $C_g = -9.2$. First fit results in this analysis, however, showed that $C_g < 0$ could not yield a minimum χ^2 . Therefore $C_g = 1.3$ was used as starting parameter for the uPDF fits here.

Two points in the distribution of χ^2 as a function of C_g (lower right plot, fig. 6.1) strongly deviate from their surrounding values. These fluctuations stem from integration problems in CASCADE which have been fixed in newer versions of the generator.

For N_g and A_g the results from [55] correspond nicely to the minima shown in figure 6.1 and were used as starting values in the fits of uPDFs here.

Table 6.1 lists all the starting and final values as well as the χ^2 values for the respective number of degrees of freedom (n.d.f.). The resulting uPDF is referred to as *fit A*. The achieved $\chi^2/n.d.f. = 1.27$ points to a good description of the data by

6.4 Unintegrated Gluon Densities from D^* Mesons at low Q^2

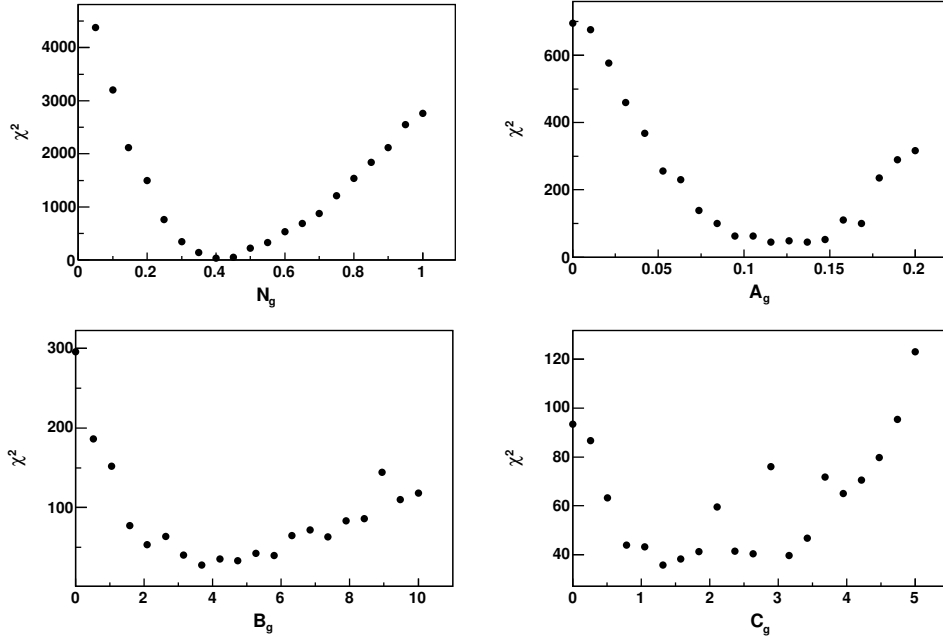


Figure 6.1: Scans of the parameters N_g , A_g , B_g and C_g of the initial unintegrated gluon density $\mathcal{A}_0(x_g, k_t)$, giving distributions of χ^2 values as functions of the four parameters.

the cross section predictions from CASCADE using fit A.

The initial gluon density of fit A is presented in figure 6.2 as a function of $\log x_g$ (upper plot) and $\log k_t^2$ (lower plot). Shown are gluon densities evolved according to the CCFM equation at different constant k_t^2 and x_g , respectively.

Bacchetta et al. found that “the addition of [the parameter C_g] substantially improves the description of the data we consider.” ([55], p. 5) Since their result $C_g = -9.2$ could not be brought in good agreement with the measurement presented here, a third fit (*fit B*) was done where the parameter C_g has been fixed to zero. The

Parameter	starting value	final value
N_g	0.417	0.418
A_g	0.125	0.121
B_g	4.0	4.0
C_g	1.3	1.24
$\chi^2/n.d.f.$	51.1/19	24.1/19

Table 6.1: Starting and final parameter values of the unintegrated gluon density fit A as determined with CASCADE.

uPDF	N_g	A_g	B_g	C_g	$\chi^2/n.d.f.$
fit A	0.418	0.121	4.0	1.24	1.21
fit B	0.454	0.089	4.0	0.	1.69
setA0 norm fit	0.61	0.	4.0	0.	2.06

Table 6.2: Comparison of final parameter values of three fitted sets of uPDF as determined with CASCADE.

purpose of this was to estimate the significance of the $C_g \cdot x$ term in equation 6.5. It was found that a good description of the data is possible with $C_g = 0$ resulting in $\chi^2/n.d.f. = 1.69$, but at the same time giving a significantly different value for A_g of about 0.089. This seems to point to a strong correlation between the parameters A_g and C_g .

Table 6.2 summarizes these results. The parameters N_g , A_g , B_g and C_g for all three uPDF fits are shown together with the corresponding $\chi^2/n.d.f.$. Errors given in the tables are rough estimates by the simplex method used for the fits here.

In addition to the results of fit A and B a third fit has been performed which is referred to as *setA0 norm fit* in table 6.2 and in the following. Set A0 is defined by

$$\mathcal{A}^{setA0}(x_g) = N_g(1 - x_g)^4.$$

In order to compare the resulting gluon density from fit A to the formerly used set A0 only the normalization factor N_g has been varied. The result was $\chi^2/n.d.f. = 43.3/21$, which is considerably larger than for fit A and fit B.

Figure 6.3 shows a comparison of the differential cross sections from this measurement (black dots) as presented in section 3.11, CASCADE using the uPDF from fit A (solid red line) and CASCADE using set A0 norm fit. (dashed blue line). Although the overall χ^2 is better for fit A, these cross section predictions indicate that the inclusion of the parameters A_g and C_g do not significantly improve the data presented in this analysis. Also the shapes are not improved much, as can be seen from the ratio plots below each cross section (see eq. 3.30). This is mainly due to the large systematic uncertainties, which haven't been included in the fits.

Figure 6.4 shows a comparison of the three uPDFs from the three fits (fit A: solid line, fit B: coarsely dashed line and setA0 norm fit: finely dashed line). Shown is the energy weighted gluon density $x\mathcal{A}(x_g, k_t, \bar{q})$ as a function of $\log x_g$ for different fixed values of the squared transverse momentum k_t^2 of the gluon, with $k_t^2 = 1 \text{ GeV}^2$ presented in black, $k_t^2 = 50 \text{ GeV}^2$ in blue and $k_t^2 = 100 \text{ GeV}^2$ in light blue. The

evolution variable $\bar{q} = \hat{s} + Q^2$ sets the upper scale of parton emission in the evolution. The evolution with the transverse momentum is nicely visible.

What can also be seen is the difference in shape of the three uPDFs. The normalization fitted set A0 (finely dashed line) does not include the $1/x$ term, and at lowest k_t^2 this visible in the fact that at low x_g the uPDF is flat in $\log x_g$. Towards larger k_t^2 its shapes more and more resembles that of the other uPDFs.

Fit B (coarsely dashed line) is more similar to fit A in shape, but with $C_g = 0$ its shape is less steep. It can be seen here that the parameter C_g strongly influences the low x_g behavior of the uPDFs and seems to be correlated to the parameter A_g , as noted above.

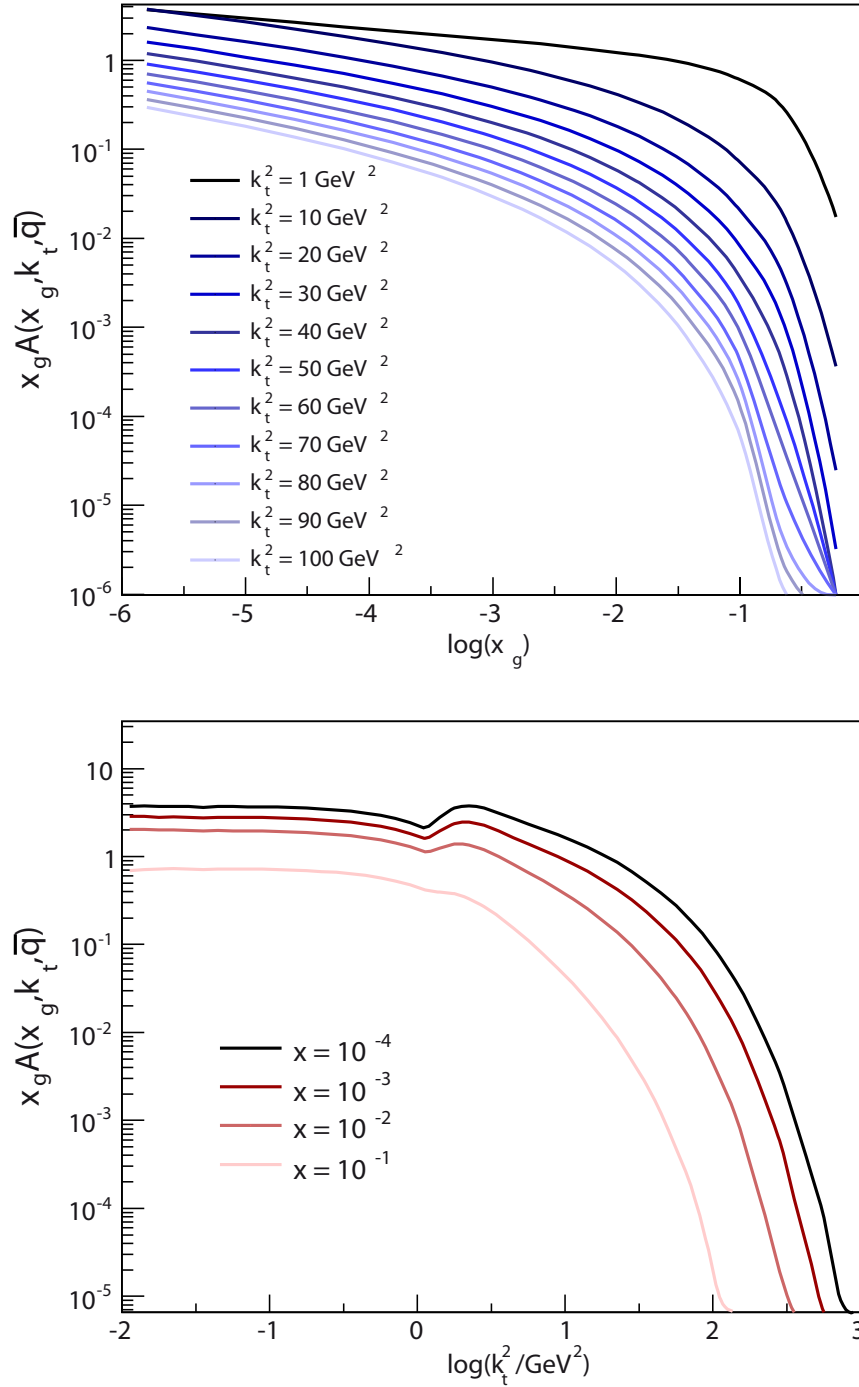


Figure 6.2: Unintegrated gluon densities as a function of $\log x_g$ (upper plot) and $\log k_t^2$ (lower plot) for different constant k_t^2 and x_g , respectively. In the upper (lower) plot the unintegrated gluon densities are presented at different k_t^2 ($\log x_g$), with black representing the lowest k_t^2 ($\log x_g$) and the lightest blue (red) representing the highest k_t^2 ($\log x_g$). The evolution variable $\bar{q} = \hat{s} + Q^2$ sets the upper scale of parton emission in the evolution.

6.4 Unintegrated Gluon Densities from D^* Mesons at low Q^2

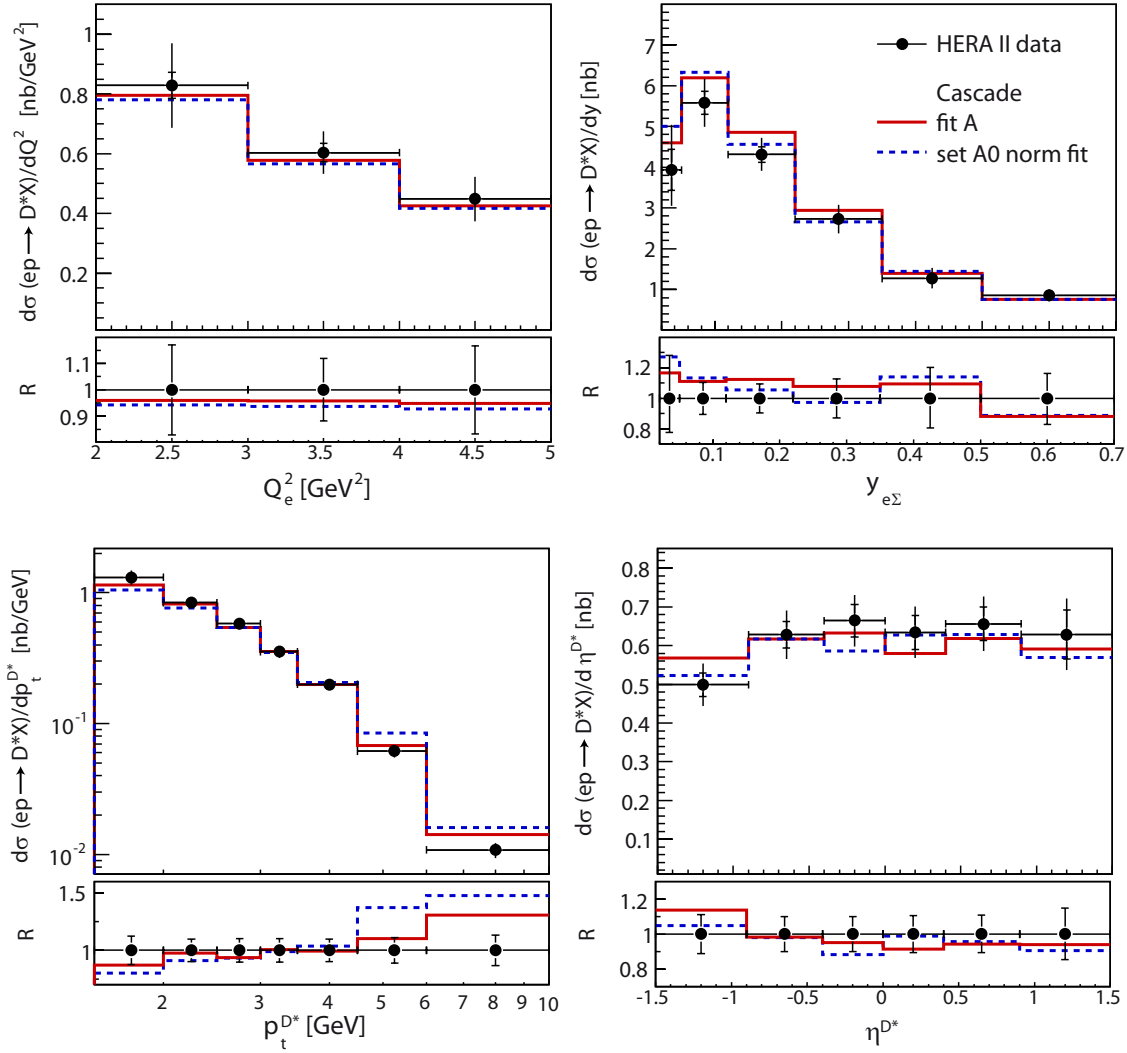


Figure 6.3: Comparison of single Differential D^* meson cross sections as measured in this thesis and predictions from CASCADE using the extracted parameters for the initial unintegrated gluon density. Shown are the cross sections in Q_e^2 , $y_{e\Sigma}$, $p_t^{D^*}$ and η^{D^*} . Data is shown as black dots, the solid red line represents the prediction of CASCADE using the $uPDF$ of fit A, and the dashed blue line represents the prediction of CASCADE using the $uPDF$ of set A0 norm fit. Statical uncertainties of the data are presented as inner error bars, while the outer error bars represent the total uncertainties.

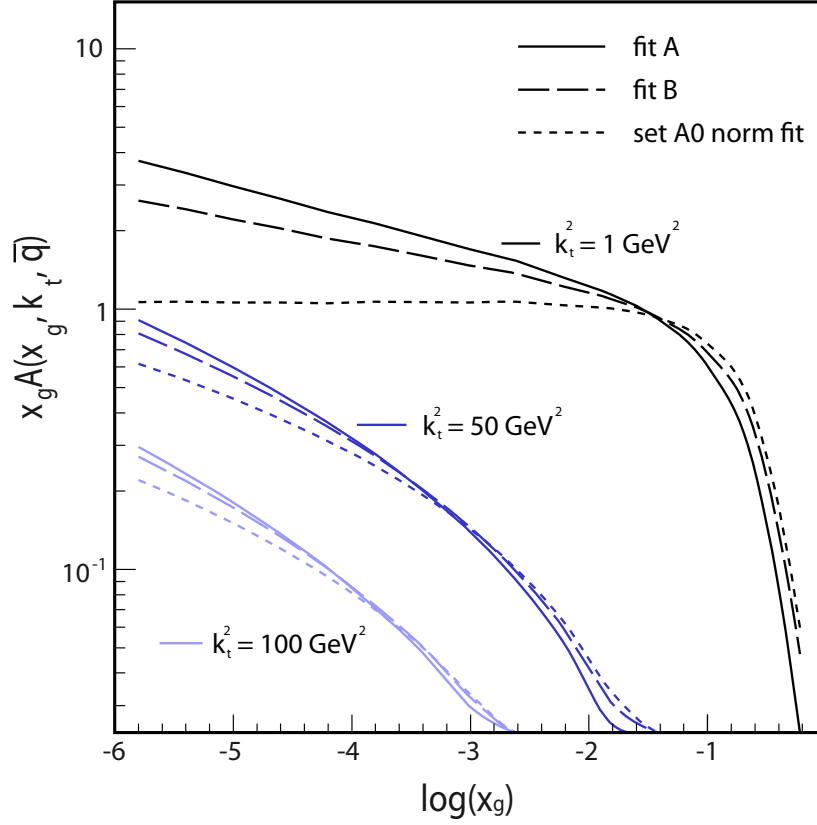


Figure 6.4: *Unintegrated gluon densities as a function of $\log x_g$. The solid lines are results from fit A, the coarsely dashed lines results from fit B and the finely dashed lines results from the setA0 norm fit. Black lines represent the respective unintegrated gluon densities at $k_t^2 = 1 \text{ GeV}^2$, blue lines at $k_t^2 = 50 \text{ GeV}^2$ and light blue lines at $k_t^2 = 100 \text{ GeV}^2$. The evolution variable $\bar{q} = \hat{s} + Q^2$ sets the upper scale of parton emission in the evolution.*

Summary and Conclusion

For the first time unintegrated gluon densities have been determined by measurements of single differential $D^{*\pm}$ meson production cross sections at H1 using the Monte Carlo event generator CASCADE.

The total, single differential and double differential cross sections have been measured for the production of $D^{*\pm}$ mesons at low photon virtualities with the H1 detector. The full HERA II data sample with an integrated luminosity of 348 pb^{-1} was exploited to measure cross sections more differentiated than previous $D^{*\pm}$ meson production measurements at H1. This measurement complements the analyses of Jung [1] and Brinkmann [2, 3], who measured the production of $D^{*\pm}$ mesons in the virtuality regions $5 \text{ GeV}^2 < Q^2 < 100 \text{ GeV}^2$ and $100 \text{ GeV}^2 < Q^2 < 1000 \text{ GeV}^2$, respectively.

The phase space of this measurement is restricted to a photon virtuality range of $2 \text{ GeV}^2 < Q^2 < 5 \text{ GeV}^2$, an inelasticity range of $0.02 < y < 0.7$, a pseudo rapidity range of $-1.5 < \eta^{D^*} < 1.5$ and transverse momenta $p_t^{D^*}$ above 1.5 GeV. Single differential cross sections as functions of these four variables have been measured in these ranges, except for $d\sigma(e^\pm p \rightarrow e^\pm D^{*\pm} X)/dp_t^{D^*}$. In addition, double differential cross section $d\sigma^2/dQ^2 dy$ and $d\sigma^2/dp_t^{D^*} d\eta^{D^*}$ have been determined and compared to Monte Carlo predictions.

All cross sections have been compared to predictions from the Monte Carlo event generators RAPGAP and CASCADE. Both Monte Carlo predictions undershoot the data but describe the shapes of all distributions rather well.

Unintegrated gluon densities have been fitted to the measured single differential cross sections of $D^{*\pm}$ production with the *Monte Carlo method for PDF extraction*. This method uses Monte Carlo event generators to fit initial parton densities. It has been applied here to fit unintegrated gluon densities to $D^{*\pm}$ production cross sections for the first time.

Three different parametrizations have been used, all of which led to results which showed a good agreement to the measured data. The individual initial gluon distributions differ quite strongly, but the cross section prediction only slightly differ in

Summary and Conclusion

shape. This insignificance of the presented measurement to the initial gluon density parametrization stems from the restricted phase space of this measurement as well as from the large systematic uncertainties of the data.

This analysis has been the first determination of unintegrated gluon densities from charm production in electron-proton collisions. Further fits of unintegrated gluon densities to the whole $D^{*\pm}$ production phase space at H1 can enhance the sensitivity and lead to more restricted set of unintegrated gluon densities. The inclusion of more HERA data sets like the proton structure functions F_2 and $F_2^{c\bar{c}}$ can be used to further restrict the parameters of the unintegrated gluon densities.

A Cross Section Tables

Q^2 range [GeV ²]	$d\sigma(e^\pm p \rightarrow e^\pm D^{*\pm} X)/dQ^2$ [nb/GeV ²]	$\sigma_{stat.}$ [%]	$\sigma_{sys.}$ [%]	$\sigma_{tot.}$ [%]
2 - 3	0.829	± 5.3	± 16.2	± 17.1
3 - 4	0.603	± 5.1	± 10.7	± 11.9
4 - 5	0.448	± 4.7	± 16.0	± 16.7

Table A.1: Single differential cross section as a function of Q_e^2 with statistical ($\sigma_{stat.}$), systematic ($\sigma_{sys.}$) and total ($\sigma_{tot.}$) uncertainties.

y range	$d\sigma(e^\pm p \rightarrow e^\pm D^{*\pm} X)/dy$ [nb]	$\sigma_{stat.}$ [%]	$\sigma_{sys.}$ [%]	$\sigma_{tot.}$ [%]
0.02 - 0.05	3.93	± 12.7	+25.2 -18.4	+28.2 -22.4
0.05 - 0.12	5.58	± 5.0	± 9.3	± 10.5
0.12 - 0.22	4.31	± 4.4	± 8.4	± 9.5
0.22 - 0.35	2.73	± 6.1	± 11.2	± 12.7
0.35 - 0.5	1.27	± 7.2	+19.1 -18.1	+20.4 -19.5
0.5 - 0.7	0.86	± 13.2	+9.5 -10.8	+16.3 -17.1

Table A.2: Single differential cross section as a function of $y_{e\Sigma}$ with statistical ($\sigma_{stat.}$), systematic ($\sigma_{sys.}$) and total ($\sigma_{tot.}$) uncertainties.

$p_t^{D^*}$ range [GeV]	$d\sigma(e^\pm p \rightarrow e^\pm D^{*\pm} X)/dp_t^{D^*}$ [nb/GeV]	$\sigma_{stat.}$ [%]	$\sigma_{sys.}$ [%]	$\sigma_{tot.}$ [%]
1.5 - 2.0	1.312	± 9.6	± 7.9	± 12.5
2.0 - 2.5	0.839	± 5.8	± 7.8	± 9.7
2.5 - 3.0	0.580	± 6.2	± 8.0	± 10.1
3.0 - 3.5	0.354	± 6.2	± 8.3	± 10.4
3.5 - 4.5	0.199	± 5.0	± 8.4	± 9.8
4.5 - 6.0	0.062	± 6.4	$^{+9.2}_{-8.9}$	$^{+11.3}_{-11.0}$
6.0 - 10	0.011	± 9.2	± 9.5	± 13.3

Table A.3: *Single differential cross section as a function of $p_t^{D^*}$ with statistical ($\sigma_{stat.}$), systematic ($\sigma_{sys.}$) and total ($\sigma_{tot.}$) uncertainties.*

η^{D^*} range	$d\sigma(e^\pm p \rightarrow e^\pm D^{*\pm} X)/d\eta^{D^*}$ [nb]	$\sigma_{stat.}$ [%]	$\sigma_{sys.}$ [%]	$\sigma_{tot.}$ [%]
-1.5 - -0.9	0.499	± 6.0	± 9.3	± 11.1
-0.9 - -0.4	0.628	± 5.5	± 8.3	± 10.0
-0.4 - 0	0.664	± 6.4	± 7.8	± 10.0
0 - 0.4	0.634	± 6.9	± 7.9	± 10.5
0.4 - 0.9	0.656	± 6.7	± 8.4	± 10.7
0.9 - 1.5	0.629	± 10.1	± 10.8	± 14.8

Table A.4: *Single differential cross section as a function of η^{D^*} with statistical ($\sigma_{stat.}$), systematic ($\sigma_{sys.}$) and total ($\sigma_{tot.}$) uncertainties.*

Q^2 range [GeV ²]	y range	$d\sigma^2(e^\pm p \rightarrow e^\pm D^{*\pm} X)/dQ^2 dy$ [nb/GeV ²]	$\sigma_{stat.}$ [%]	$\sigma_{sys.}$ [%]	$\sigma_{tot.}$ [%]
2 - 3	0.02 - 0.09	1.861	± 10.3	± 18.1	± 20.8
	0.09 - 0.16	1.606	± 5.4	+9.1 -8.7	+10.6 -10.2
	0.16 - 0.32	1.359	± 7.6	+15.4 -15.1	+17.1 -16.8
	0.32 - 0.7	0.582	± 9.8	± 29.3	± 30.9
3 - 4	0.02 - 0.09	1.281	± 10.2	+11.6 -11.2	+15.4 -15.1
	0.09 - 0.16	1.739	± 7.4	± 7.8	± 10.8
	0.16 - 0.32	1.028	± 7.5	+9.5 -10.0	+12.1 -12.5
	0.32 - 0.7	0.480	± 16.1	+8.8 -10.8	+18.4 -19.4
4 - 5	0.02 - 0.09	1.291	± 8.5	+17.6 -13.5	+19.6 -15.9
	0.09 - 0.16	1.226	± 7.9	+8.6 -8.1	+11.6 -11.3
	0.16 - 0.32	0.792	± 8.0	+8.5 -7.8	+11.6 -11.2
	0.32 - 0.7	0.342	± 12.9	+8.9 -8.7	+15.7 -15.6

Table A.5: Double differential cross section as a function of Q_e^2 and $y_{e\Sigma}$ with statistical ($\sigma_{stat.}$), systematic ($\sigma_{sys.}$) and total ($\sigma_{tot.}$) uncertainties.

$p_t^{D^*}$ range [GeV]	η^{D^*} range	$d\sigma^2(e^\pm p \rightarrow e^\pm D^{*\pm} X)/dp_t^{D^*} d\eta^{D^*}$ [nb/GeV]	$\sigma_{stat.}$ [%]	$\sigma_{sys.}$ [%]	$\sigma_{tot.}$ [%]
1.5 - 2.5	-1.5 - -0.75	0.263	± 8.3	$^{+21.1}_{-18.1}$	$^{+22.7}_{-19.9}$
	-0.75 - 0	0.316	± 10.4	± 7.9	± 13.1
	0 - 0.75	0.334	± 9.3	$^{+8.7}_{-8.2}$	$^{+12.8}_{-12.4}$
	0.75 - 1.5	0.440	± 15.4	± 8.5	± 17.6
2.5 - 4.5	-1.5 - -0.75	0.160	± 6.8	± 9.8	± 11.9
	-0.75 - 0	0.262	± 5.2	± 7.9	± 9.4
	0 - 0.75	0.209	± 6.6	± 8.0	± 10.4
	0.75 - 1.5	0.222	± 10.2	$^{+8.7}_{-9.5}$	$^{+13.4}_{13.9}$
4.5 - 10	-1.5 - -0.75	0.027	± 12.2	$^{+14.8}_{-25.3}$	$^{+19.1}_{-28.1}$
	-0.75 - 0	0.050	± 8.9	$^{+11.4}_{-9.6}$	$^{+14.4}_{-13.0}$
	0 - 0.75	0.054	± 9.8	$^{+7.8}_{-7.9}$	$^{+12.5}_{-12.6}$
	0.75 - 1.5	0.042	± 13.8	$^{+11.9}_{-12.6}$	$^{+18.2}_{-18.7}$

Table A.6: Double differential cross section as a function of $p_t^{D^*}$ and η^{D^*} with statistical ($\sigma_{stat.}$), systematic ($\sigma_{sys.}$) and total ($\sigma_{tot.}$) uncertainties.

Bibliography

- [1] Andreas W. Jung. *Measurement of the $D^{*\pm}$ Meson Cross Section And Extraction Of The Charm Contribution, $F_2^c(x, Q^2)$, To The Proton Structure In Deep Inelastic Scattering With The H1 Detector At HERA*. PhD thesis, Ruprecht-Karls-Universität Heidelberg, <http://www-h1.desy.de/psfiles/theses/h1th-504.pdf>, January 2009.
- [2] M. Brinkmann. *Measurement of the $D^{*\pm}$ Meson Production Cross Section and $F_2^{c\bar{c}}$ at High Q^2 in ep Scattering at HERA*. PhD thesis, Hamburg, 2010.
- [3] F. D. Aaron et. al. (H1 Collaboration). *Measurement of the D^* Meson Production Cross Section and $F_2^{c\bar{c}}$, at High Q^2 , in ep Scattering at HERA*. *DESY 09-165*, 2009.
- [4] F. Halzen, A. D. Martin. *Quarks and Leptons*. John Wiley and Sons, 1984.
- [5] E. D. Bloom et. al. *High-Energy Inelastic ep Scattering at 6 degrees and 10 degrees*. *Phys. Rev. Lett.*, 23:930, 1969.
- [6] M. Breidenbach et al. *Observed Behavior of Highly Inelastic electron- Proton Scattering*. *Phys. Rev. Lett.*, 23:935–939, 1969.
- [7] P. Söding, I. Flegel. *Twenty-five years of gluons*. *CERN Courier*, 2004. <http://cerncourier.com/cws/article/cern/29201>.
- [8] C. Amser et. al. (Particle Data Group). 2009. <http://pdg.lbl.gov/2009/tables/rpp2009-sum-quarks.pdf>.
- [9] H. Jung. *k_t -factorization and CCFM: The solution for describing the hadronic final states - everywhere?* *Mod. Phys. Lett.*, 2004. arXiv:hep-ph/0311249.
- [10] S. Mrenna P. Skands T. Sjöstrand, L. Lönnblad. *PYTHIA 6.2 Physics and Manual*. <http://home.thep.lu.se/~torbjorn/pythia/pythia6206.pdf>.

Bibliography

- [11] H. Jung. The RAPGAP Monte Carlo for Deep Inelastic Scattering, Version 3.1. 2005. available at <http://www.desy.de/%7EJung/rapgap/rapgap31021.ps.gz>.
- [12] H. Jung. <http://projects.hepforge.org/cascade/>.
- [13] HZTOOL. <http://projects.hepforge.org/hztool/>.
- [14] I. Abt et. al. (H1 Collaboration). The H1-Detector at HERA. *Nucl. Instr. Meth.*, A(386):310–347 and 348–396, 1997. <http://www-h1.desy.de/h1/www/h1det/detpaper/contents.html>.
- [15] B. Andrieu et. al. (H1 Collaboration). Beam Tests and Calibration of the H1 Liquid Argon Calorimeter with Electrons. *Nucl. Instr. Meth.*, A(350):57–72, 1994.
- [16] R. D. Appuhn et. al. (H1 Collaboration). The H1 Lead/Scintillating-Fibre Calorimeter. *Nucl. Instr. Meth.*, A(386):397–408, 1997.
- [17] J. Ban et al. (H1 BEMC Group). The H1 Backward Calorimeter BEMC and its Inclusive Electron Trigger. *Nucl. Instr. Meth.*, A(372):399–414, 1996.
- [18] A. Aktas et. al. (H1 Collaboration). *arXiv: hep-ex/0703022*, 2007.
- [19] R. Brun et. al. Geant3 user’s guide. Cern-dd/ee-81-1, CERN, 1987.
- [20] S. Aid et al. (H1 Collaboration). *Z.Phys.C*, 72:593–605, 1996.
- [21] J. Breitweg et al. (ZEUS Collaboration). *Phys. Lett. B*, 407:402–418, 1997.
- [22] C. Adloff et al. (H1 Collaboration). *Nucl. Phys. B*, 545:21–44, 1999.
- [23] J. Breitweg. *Eur. Phys. J. C*, 12:35, 2000.
- [24] J. Breitweg et al. (ZEUS collaboration). *Eur. Phys. J.*, C12:35 ff., 2000.
- [25] C. Adloff et al. (H1 Collaboration). *Phys. Lett.*, B528:156 ff., 2002.
- [26] S. Chekanov et al. (ZEUS Collaboration). *Physical Review D*, 69:012004, 2004.
- [27] A. Baird et al. *IEEE Trans. Nucl. Sci.*, 48:1276–1285, 2001.
- [28] A. Aktas et. al. (H1 Collaboration). *arXiv: hep-ex/0701023*, 2006.
- [29] A. Aktas et. al. (H1 Collaboration). *arXiv: hep-ex/0608042*, 2006.

- [30] A. Aktas et. al. (H1 Collaboration). *arXiv: hep-ex/0503038*, 2005.
- [31] A. Aktas et. al. (H1 Collaboration). *arXiv: hep-ex/0502010*, 2005.
- [32] U. Bassler, G. Bernardi. On the Kinematic Reconstruction of Deep Inelastic Scattering at HERA: The Σ Method. *arXiv:hep-ex/9412004*, October 1994.
- [33] W. M Yao et. al. (Particle Data Group). Review of particle physics. *J. Phys.*, (G33), 2006.
- [34] J. E. Gaiser. *Charmonium Spectroscopy from Radiative Decays*. PhD thesis, Stanford University, 1982.
- [35] P. Granet et. al. *Nucl. Phys. B140*, page 389, 1978.
- [36] W. Verkerke, D. Kirkby. The RooFit Toolkit for Data Modeling. <http://roofit.sourceforge.net/>.
- [37] A. Bukin. Fitting function for asymmetric peaks. *arXiv:0711.4449*, 2007.
- [38] M. O. Boenig. *Messung des D^* -Meson-Produktionsquerschnitts in tiefinelastischer Streuung mit dem H1 Experiment*. PhD thesis, Universität Dortmund, 2007.
- [39] J. Collins, D. Soper, G. Sterman. Factorization of Hard Processes in QCD. *arXiv: hep-ph/0409319v1*, 2004.
- [40] C. F. von Weizsäcker. Radiation emitted in collisions of very fast electrons. *Z. Phys.*, 88:612–625, 1934.
- [41] E. J. Williams. Nature of the high-energy particles of penetrating radiation and status of ionization and radiation formulae. *Phys. Rev.*, 45:729–730, 1934.
- [42] M. Ciafaloni. *Nucl. Phys.*, B 296:49, 1988.
- [43] G. Marchesini S. Catani, F. Fiorani. *Phys. Lett.*, B 234:339, 1990.
- [44] G. Marchesini S. Catani, F. Fiorani. *Nucl. Phys.*, B 336:18, 1990.
- [45] G. Marchesini. *Nucl. Phys.*, B 445:49, 1995.
- [46] H. Jung. Un-integrated PDFs in CCFM. *arXiv:hep-ph/0411287v1*, 2004.

Bibliography

- [47] Gustafson G. Anderson, B. and B. Soderberg. Parton fragmentation and string dynamics. *Phys. Rep.*, 97:31–145, 1983.
- [48] G. Marchesini et. al. *Comp. Phys. Comm.*, 67:465, 1992.
- [49] G. Corcella et. al. *JHEP*, 0101, 2001.
- [50] PDF4MC. http://www.terascale.de/sites/site_terascale/content/e43/e46/e511/e1414/e1741/infoboxContent1744/pdf4mc.pdf.
- [51] R. Devenish, A. Cooper-Sarkar. *Deep Inelastic Scattering*. Oxford University Press, 2004.
- [52] CTEQ Collaboration. <http://www.phys.psu.edu/~cteq/>.
- [53] MSTW. <http://projects.hepforge.org/mstwpdf/>.
- [54] F. James. *MINUIT - Function Minimization and Error Analysis*.
- [55] A. Bacchetta et al. A method for tuning parameters of monte carlo generators and a its application to the determination of the unintegrated gluon density. *arXiv: hep-ph/4675v2*.

Acknowledgments – Danksagung

No thesis is ever written in isolation. Many people contributed to this work, some of them without realizing it. My humble supervisor Hannes, for example, would probably point out that I wrote it, not him. Nonetheless I owe him a lot for his understanding, his constant motivation and his nearly stubborn support until the very end.

Thanks also to Joachim Meyer, who brought me to Hamburg and whose criticism of my work greatly helped me improving it. To Andy and Klaus from the Dortmund office for all the tips and advice. To Karin and Katja, who now lead the H1 collaboration and once helped me to really understand the traps and pitfalls of D^* s. And to everyone in the H1 Collaboration I didn't mention!

Auch meinen neuen Kolleginnen und Kollegen Karen, Walter und Uta bin ich einigen Dank schuldig. Dass sie mir so den Rücken frei gehalten haben und es mir so einfach gemacht haben, meine neue Arbeit mit meiner alten ein ganzes Jahr lang zu verbinden, ist nicht selbstverständlich.

During my time as a PhD student I met a lot of weird personalities: a tall, red haired Spaniard, a black haired Swede, a Bulgarian from the 80s, a jewish Scotsman, a British Indian, a Slovakian libertarian, an American socialist, a Russian belly dancer, a physicist called Albert and many more. I will never forget the great times we had in Hamburg!

All meinen Freunden außerhalb des DESY – Nils, Marc, Renke, Christian, Armin und dene, die ich gerade vergesse – vielen Dank für Dschungelnächte, Zockarien und alles, was einem von der Arbeit ablenkt. Jetzt ist Zeit für Nebensächliches!

Großer Dank geht an meine Familie: meiner Mutter Inge, meinem verstorbenen Vater Fritz, meiner Schwester Sabine und meinem Neffen Timo.

Am allermeisten aber verdanke ich meiner zukünftigen Ehefrau Mara. Sie hat mich im schwierigsten Jahr erwischt, dem letzten, und hat die tiefsten Tiefen dieser Zeit mitgemacht. Es ist endlich an der Zeit, mit ihr in die höchsten Höhen aufzubrechen!

Acknowledgments – Danksagung

Erklärung

Hiermit versichere ich, die vorliegende Arbeit selbstständig und nur unter Verwendung der angegebenen Hilfsmittel angefertigt zu haben.

Hamburg, den 3.12.2010